Environmental Effects on the Mechanical Properties and Adhesion of Gecko Setae

Michael S. Prowse

A dissertation submitted in partial fulfillment
of the requirements for the degree of

Doctor of Philosophy

University of Washington

2012

Reading Committee:

Kellar Autumn

George Mayer

Brian Flinn

Program Authorized to Offer Degree: Materials Science and Engineering

ACKNOWLEDGEMENTS

This work was supported by NSF-IOS-0847953 (KA) and NSF-NBM-0900723 (KA). I like to acknowledge Kellar Autumn, Andrew Schnell, Kristen Crandell, Jon Puthoff, and Matt Wilkinson at Lewis and Clark College for his assistance in specimen collection, advice, and preparation. I also thank FEI Corp. for SEM imagining, Tobias Weidner and Joe Baio for NEXAFS data collection.

Dedication

The author wishes to express sincere appreciation to my understanding and patient wife Jin and to my young sons Benjamin and Nicolas, who arrived midway through this thesis work.

University of Washington

Abstract

Environmental Effects on the Mechanical Properties and Adhesion of Gecko Setae

Michael S. Prowse

Chair of the Supervisory Committee:
Professor Autumn Kellar
Materials Science and Engineering

Geckos have an amazing ability to climb walls and cling to inverted surfaces. While other terrestrial animals, such as tree frogs also process such abilities, geckos are unique given their reasonably large body mass. Geckos owe their remarkable adhesiveness to millions of dry setae on their toes, and the mechanism of adhesion in gecko setae has been the topic of scientific scrutiny for over two hundred years. Previously, it was demonstrated that van der Waals forces alone are sufficient for strong adhesion and friction in gecko setae. However, more recent studies have demonstrated that adhesion increases with relative humidity and proposed that surface hydration and capillary water bridge formation is important or even necessary.

In this study, we confirmed a considerable effect of humidity on gecko adhesion; but we reject the capillary adhesion premise. While the contact forces of isolated Tokay gecko setal arrays increased with humidity, the increase was similar on both hydrophobic and hydrophilic surfaces which are inconsistent with a capillary adhesion mechanism. Additionally, contact forces increased with humidity even at high shear rates, where capillary bridge formation is too slow to contribute to adhesion.

How can a humidity-related increase in adhesive and frictional force be explained? The effect of relative humidity on the mechanical properties of setal β-keratin has escaped consideration. We discovered that an increase in humidity softens the setae and increases viscoelastic damping, which increases adhesion. We measured the effect of RH on the tensile deformation properties, fracture, and dynamic mechanical response of an isolated Tokay gecko setae and strips of the smooth lamellar epidermal layer. The mechanical properties of gecko setae were affected strongly by RH. The changes in mechanical properties of setal keratin were consistent with previously reported increases in contact forces, supporting the hypothesis that an increase in RH softens setal keratin. Changes in setal materials properties, not capillary forces, fully explain humidity-enhanced adhesion, and van der Waals forces remain the only empirically supported mechanism of adhesion in geckos.

TABLE OF CONTENTS

LIST OF FIGURES

LIST OF TABLES

Tables Number Page

Chapter 1

1.1 Introduction

Many terrestrial organisms have the ability to adhere to vertical or even inverted surfaces from insects (ex. spiders, ladybugs, flies) [Federle 2002] to tree frogs and lizards (geckos, anoles, and skinks). The mechanisms of adhesion varies from fluid-based adhesives in tree frogs [Persson 2007, Federle 2006], insects [Federle 2002 and Dirks 2011], to dry adhesives that rely on van der Waals (vdW) force in some lizards [Autumn 2002a]. Of these many terrestrial species capable of locomotion on vertical or inverted surfaces, geckos have garnered a great deal of interest and are widely studied due their relativity high body mass, 200g or more for Tokay gecko (*Gekko gecko*) while exhibiting versatile and effective adhesion [Autumn 2006a, Autumn 2002b, Hiller 1975, Irschick 1996].

Geckos have an amazing ability to run up walls or across ceilings with ease due to their remarkable toes. Their toes are not sticky, unlike many traditional pressure sensitive adhesives (PSAs), such as scotch tape. Instead their toes are covered with a 'smart adhesive', one that is non-fouling [Hansen 2005], non-tacky, dry to the touch [Autumn 2006a], and easily detaches at a critical angle yet strongly adheres when pre-loaded [Autumn 2006b, Autumn 2000, Yamaguchi 2009]. Each toe bears a hierarchical structure made of a series of ridges composed of hair-like shafts (setae) which divide into hundreds of flat tips called spatula that make intimate contact with the adhered surface [Federle 2006, Autumn 2002b, Maderson 1964, Ruibal and Ernst 1965], that are composed of β-keratin [Alibardi 2003, Maderson 1964, Rizzo 2006, Alibardi 2011].

Naturally, there has been a number of research programs focused on achieving synthetic gecko-like adhesives (GSAs) [Autumn 2002b, Geim 2003, Lee 2009, Mahdavi 2008, Murphy 2007, Sitti and Fearing 2003, Campolo 2003, Liagti 2008] using a variety of methods from soft polymer based arrays [Geim 2003, Lee 2009, Mahdavi 2008, Murphy 2007, Sitti and Fearing 2003, Campolo 2003] to carbon nano-tubes [Liagti 2008]. Creating a synthetic GSA that successfully matches the function of the gecko setal array remains unattained.

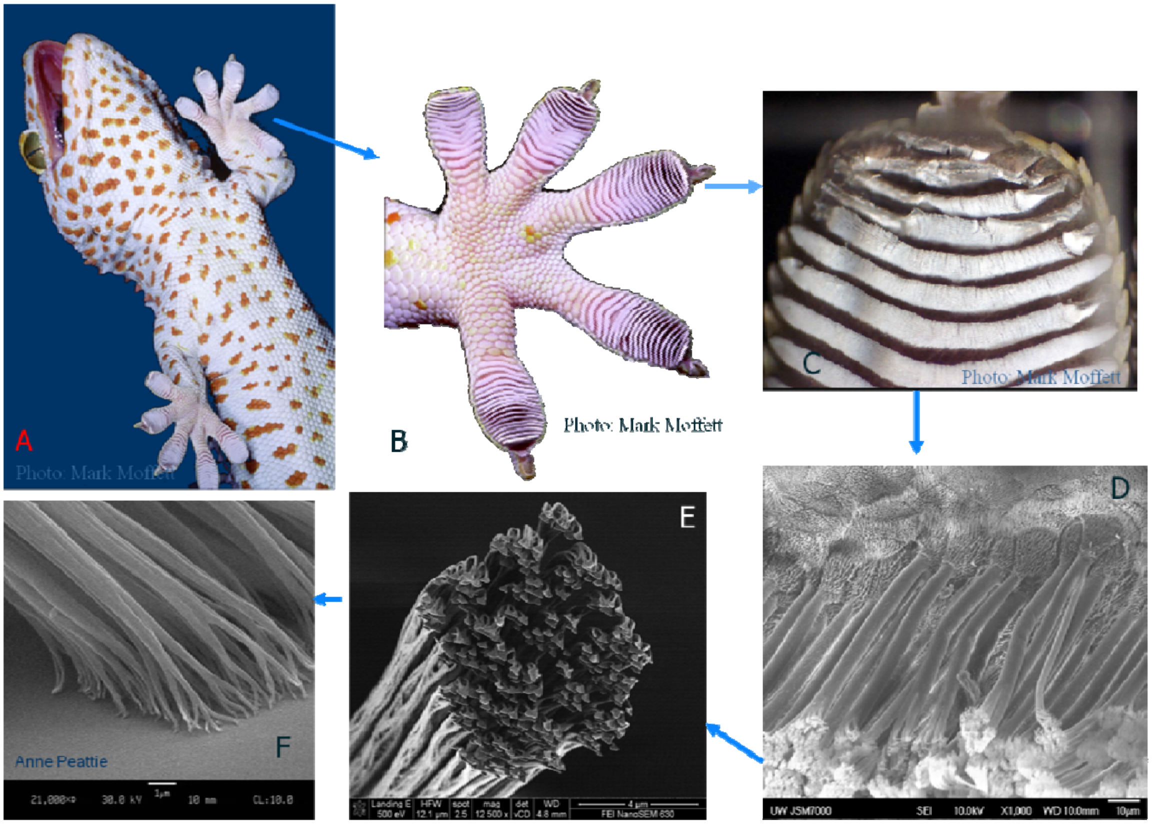

Figure 1.1 The Gecko setal hierarchy; A) Gekko gecko, B) foot and toe structure of the Gekko gecko, C) Optically magnified image of the toe ridges (setal arrays), D) Electro-micrograph of the microstructure shows individual shafts and the branching at the end. E) Electro-micrograph of an isolated seta. Each seta branch to form hundreds of flat tips called spatula. F) Electro-micrograph of an isolated seta adhered to a surface. (Images courtesy of M. Moffett, a, b, c; Prowse, d, e; and A. Peattie, f)

1.2 Gecko Adhesion

Since the times of ancient Greece [Aristotle, republished 1910] the climbing skills of geckos have intrigued. Scientific debate over how geckos adhere to surfaces has persisted for centuries. Unsupported mechanisms for gecko adhesion include suction, electrostatic attraction, micro-interlocking, and glue. Many of these theories have been abandoned and proven false over the decades with no conclusive theory proven [Autumn 2006a]. The aspect that geckos can climb on atomically flat surfaces [Autumn 2002a, Sitti and Fearing 2003] indicates that an appendage interlocking mechanism is not required for adhesion. Electrostatic attraction also appears unnecessary [Dellit 1934]. Another proposed adhesion mechanism is capillary bridges, first indicated by Thomson [Thomson 1871], who proposed absorbed atmospheric moisture at the contact region aided adhesion. The absorbed moisture will influence adhesion between bodies at high humidities [MacFarlane and Tabor 1950, Newton 1704] and at small length scales [Fisher and Israelachvilli 1981]. Provided that the surface energy of the water is lower than the surface energy of the solids i.e. the solid surfaces are hydrophilic, capillary bridges will contribute to adhesion mostly through the Laplace pressure. In the 1970's Hiller [Hiller 1975] suggested the properties of the substrate determined the adhesion, rather than surface texture or other mechanism, this was the first evidence supporting molecular adhesion. Another possibility for gecko adhesion is a mixture of van der Waals and capillary forces as suggested for adhesion in abalone [Lin et al. 2007].

Recently, [Autumn et al. 2002b] determined van der Waals force was sufficient for the Tokay gecko to adhere to surfaces. However, a capillary mechanism has persisted in the published literature as recently as 2005 and 2008 [Huber 2005, Sun 2005, Niewiarowski 2008]. All concluding capillary forces play a role in gecko adhesion and condensed moisture from the air was sufficient. While confirming that humidity has a significant impact on adhesion Huber et al, unlike Sun et al., rejected true capillary forces since a few monolayers of water present on the substrate was insufficient to form capillary bridges. Instead Huber postulated the presence of water could modify the contact geometry or affect Van der Waals forces by chemical changes on the surface of the setae.

While most previous explanations for gecko adhesion over the years have been disproved, among them electrostatic attraction, suction, and glue, there remain two leading explanations: Van der Waals force and capillary adhesion. Van der Waals force depends on the UV refractive index and the polarizibility (dielectric constant) of the surface and is not highly dependent on the polarity (hydrophilicity). Capillary adhesion depends on the polarity (hydrophilicity) of the surface, relative vapor pressure of water, and predicts less adhesion at both very low and very high humidities. To test whether capillary adhesion or van der Waals force is a sufficient mechanism of adhesion in geckos, Autumn et al. [Autumn 2002b] measured adhesion and friction on two polarizable semiconductor surfaces that varied greatly in hydrophobicity. For capillary adhesive forces to dominate, a lack of adhesion would be expected on strongly hydrophobic surfaces. In contrast, shear stress of live gecko toes on hydrophobic gallium arsenide (GaAs) surface was not significantly different from that on hydrophilic SiO_2 surface, and the adhesion force of a single Tokay gecko seta on the hydrophilic SiO_2 and hydrophobic Si MEMS (Micro-Electro-Mechanical system) cantilevers differed by only 2%.

Additionally, Autumn et al. [Autumn 2006c] found that gecko setae are strongly hydrophobic with a water droplet contact angle of 160.9°. Since, van der Waals force is the only mechanism that can cause two hydrophobic surfaces, (gecko seta on GaAs) to adhere in air, [Parsegian 2006, Israelachvili 1992], the semiconductor experiments provided direct evidence that van der Waals force is a sufficient mechanism of adhesion in gecko setae.

The discovery, that van der Waals force is sufficient for gecko adhesion does not preclude a contribution from water or capillary adhesion under some conditions. Sun et al. [Sun 2005] measured greater adhesion in gecko spatula at 70% RH than in dry N_2. However, the theory and methods of this study leave room for interpretations other than that favored by its authors. In a subsequent study using atomic force microscopy (AFM), Huber et al. [Huber 2005] confirmed that high humidity does result in an increase adhesion of gecko spatula. In contradiction to the title of his published article ("Evidence for capillarity contributions to gecko adhesion from single spatula nanomechanical measurements"), Huber rejects true capillary forces involving a water bridge since only a few monolayers of water were present at the spatula-substrate interface, even at high humidity. Instead, Huber concludes that surface hydration either modifies the contact geometry, increasing adhesion, and/or decreases the van der Waals' Hamaker's constant, reducing adhesion. These two effects counteract each other to yield an increase in adhesion of an isolated spatula from 7nN at low relative humidity to 12nN at high RH. The results support prior work Autumn et al. [Autumn 2002b] showing that geckos can adhere solely by van der Waals forces, and suggest that van der Waals adhesion is the primary mechanism of adhesion in geckos [Pesika 2009]. Another recent study by Niewiarowski et al. [Niewiarowski 2008] showed increasing adhesion with humidity at low temperatures and decreasing adhesion at high temperatures with increasing RH. This is further evidence that humidity affects attachment forces in geckos, but the interaction between temperature and humidity is difficult to explain in terms of van der Waals or capillary theory.

1.3 Keratin consideration

Sun et al. [Sun 2005], Huber et al. [Huber 2005], and Niewiarowski et al. [Niewiarowski 2008], suggested that surface hydration (capillary forces or van der Waals enhancement) is important or even necessary for gecko adhesion, considerations of mechanical properties changes has not garnered attention.

The mechanical properties of α-keratin (alpha helix ternary structure), the form found in mammals have been studied to a much greater extent than β-keratin (pleated sheet ternary structure), the form commonly found in birds and lizards. *See figure* 1.2. This is due to the economical importance of α-keratin. There are multi-billion dollar industries based on α-keratin due to wool production. Beta-keratin has little economic benefits other than specialty items ex. snake skins or feathers.

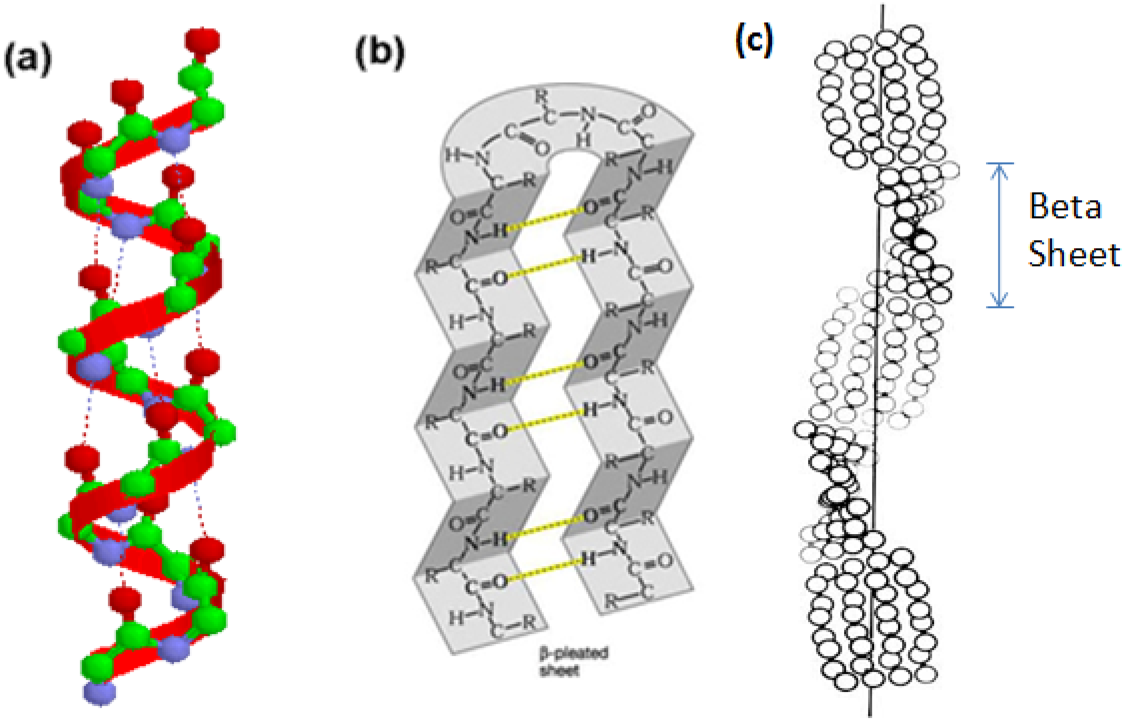

Figure 1.2, Keratin structures, a) Mammalian form, alpha helix structure of α-keratin, b) generic pleated beta sheet c) Reptilian and avian form of keratin, a twisted beta sheet structure of β-keratin with ~95Å helix.

Both α-keratin and β-keratin share very similar composite-like structures and are chemically similar [Fraser 1972, Wainwright 1976, Alexander 1950, Gillispie 1968, Lindley 1974, Eckhart 2008]. It is well known that the mechanical properties of structural proteins such as keratins are strongly affected by humidity. The mechanical properties of both α and β keratin have been shown to be highly affected by water content [Fraser 1972, Speakerman 1929, Kitchener 1987, Danilatos 1981, West 1961, Feughelman 1997, Bonser 1995, Bonser 2002, Taylor 2004]. The elastic modulus of avian β-keratin (which is closely related to gecko β -keratin [Alibardi 2003] for example, the elastic modulus decreases from 3.66 GPa to 1.47 GPa as humidity increases from 0 to 100% for feather rachis [Bonser 1995]. Therefore, we must consider the effect RH have on the mechanical properties of keratin. To date there has been no attempt to study the mechanical properties of β-keratin and the potential effects on adhesion.

1.4 Previous studies of gecko adhesion

As noted in section 1.2, there have been several recent studies of gecko adhesion with several differing claims. Huber [Huber 2005], Niewiaroski [Niewiaroski 2008], Pesika [Pesika 2009], and Sun [Sun 2005] have all noted a correlation between humidity and gecko adhesion with differing explanations. None has been truly satisfactory. Despite the well documented effects of hydration on mechanical properties of biological proteins, no author has noted the potential for mechanical properties to alter adhesion and friction of geckos. This in spite of the fact that both adhesion and friction are greatly influenced by the mechanical properties of the materials involved [Kendall 2001].

Table 1.1 Recent Gecko adhesion publications and claims.

Study	Effect of RH	Claim
Autumn et al. 2002b	**Ambient conditions - %RH not measured**	**van der Waals force is sufficient to explain gecko adhesion**
Huber, et al. 2005	**~2x increase in pull off force with an increase in humidity**	**Capillary forces enhance adhesion but no true capillary bridges**
Niewiarowski et al. 2008	**Nearly 2x increase in 'clinging' force from 25%RH to 80%RH**	**Surface hydration enhances adhesion**
Pesika et al. 2009	**Hydrophobicity decrease with water exposure** **Adhesion and friction increase with humidity** **Adhesion while immersed in water decrease (decrease van der Waals force)**	**Surface chemistry changes with humidity**
Sun et al. 2005	**2.6x increase in adhesion at 70%RH compared to 'dry N_2' environment**	**Capillary forces dominate**

Since van der Waals forces are strong between polarizable surfaces and only weakly dependant on water contact angle (hydrophobicity/hydrophilicity), Autumn et al. [Autumn 2006c] conducted a simple experiment to determine if vdW force was sufficient for gecko adhesion. Gecko adhesion was measured on three surfaces: gallium arsenide; a highly hydrophobic (water contact $\theta = 110°$) and highly polarizable ($\varepsilon = 10.88$) surface, silicon dioxide; a highly hydrophilic ($\theta = 0°$) and polarizable ($\varepsilon > 4.3$) surface, as well as bare silicon with water contact angle of $\theta = 81.9°$ and highly polarizable ($\varepsilon = 11\text{-}12$). A MEMS cantilever was used to measure the forces on Si and SiO_2, while 4 inch single crystal wafers were used for GaAs and SiO_2 measurements. It is expected that capillary adhesion will result in high adhesion on the hydrophilic SiO_2 and low adhesion on GaAs and Si, while vdW force will result in high adhesion on all surfaces. High adhesion was observed on all surfaces in support of vdW model of adhesion. In fact, the disparity between the hydrophilic and hydrophobic surfaces was ~2%. Autumn conducted the experiments under ambient conditions and did not measure relative humidity (RH).

Huber et al. [Huber 2005] measured pull off force of a single spatula in an AFM after adhering the spatula under shear load. Using a variety of hydrophilic and hydrophobic substrates Huber showed ~2x greater adhesion on hydrophilic substrates with 10° water contact angle compared with hydrophobic substrates with 110° water contact angle. In addition to using hydrophilic and hydrophobic substrates Huber demonstrated ~2x increase in adhesion from near 0%RH to ~70%RH. Interestingly, adhesion increased with increasing humidity for both hydrophilic and hydrophobic substrates, although for the hydrophobic substrate the adhesion force was slightly lower. The results and conclusion raise several questions. Why does adhesion increase with RH on a hydrophobic substrate when the Laplace pressure is expected to be repulsive between two hydrophobic surfaces [Isrealachvilli 1992]? Also, why does Huber show a continuous, roughly linear increase in adhesion with RH instead of a step function as predicted by Sun et al [Sun 2005] or MacFarlane and Tabor [MacFarlane 1950] for capillary adhesion?

Ellipsometry data confirmed only an absorbed monolayer of water was present at 88%RH on the surface of a highly hydrophilic substrate (10° water contact angle). A single monolayer of water cannot support capillary adhesion, i.e. no meniscus formation and therefore no Laplace pressure [Nosonvsky 2011]. Water does tends to condense at contact points and therefore a monolayer on a bare surface may not exclude greater amounts of water at the spatula/surface interface; however the distance between the spatula and the surface tends to exclude the possibility of a water meniscus being present. Huber does not present any other ellipsometry data on any substrates other than for the most hydrophilic. Additionally, it is expected that only RH above 90% will there be sufficient water condensation for capillaries to form [MacFarlane and Tabor 1950]. Huber ultimately rejects true capillary due to the lack of water coverage for capillary formation and the hydrophobic nature of the spatula. However in his thesis [Huber 2006], Huber does present a capillary micro-bridging hypothesis suggesting water condenses on local hydrophilic regions of the macroscopic hydrophobic setal surface. This small amount of condensed water is speculated to be sufficient to create micro-capillary bridges and enhance adhesion. Although, there is some evidence from the *Salvinia molesta* floating plant that indicates local hydrophilic regions in an otherwise hydrophobic surface [Barthlott 2010]. It is highly unlikely that a hydrophobic seta on a hydrophobic substrate will have corresponding local hydrophilic regions to initiate micro-capillary bridges. Thusly, this theory does not adequately explain the adhesion data observed on the hydrophobic surfaces.

Using an AFM with hydrophilic (water contact $\theta = 30^\circ$) and hydrophobic (water contact $\theta = 110^\circ$) cantilevers Sun et al. [Sun 2005] showed at 70%RH there was a ~2.4x greater adhesion with the hydrophilic cantilever as opposed to the hydrophobic cantilever. Also noted was an increase in adhesion with the hydrophilic cantilever from 30%RH to 80%RH by a factor of 2.6. There was no data presented for the hydrophobic cantilever at any RH other than 70%RH. Sun also speculates that since it is known that adhesion between silicon nitride AFM tips and mica is capillary and is proportional to relative humidity

[Thundat 1993] that "we can assume that the nature of forces in both systems is the same." Unlike the hydrophobic setae, both silicon nitride (θ = 40°) [Mittal 2009] and mica (θ = 15°) [Licari and Swanson 2005] are hydrophilic. Two hydrophilic surfaces are a requirement for capillary formation. Hydrophobic surfaces do not wet and thus cannot form capillary bridges. Sun offers an additional antidote to further support for the capillary hypothesis by noting zoologists often spray water on surfaces to release geckos without potentially harming the animal. Claiming this action also suggests the absence of capillary adhesion reduces gecko adhesion. Water in quantities greater than that required for capillary formation, greatly reduces adhesion. This is true whether the original adhesion was capillary or molecular.

Niewiarowski et al. [Niewiarowski 2008] performed adhesion experiments with variable temperature and relative humidity on glass substrates using whole animals as opposed to the method of using individual setae or setal arrays. This adds complication to the data as live animals add variability. Niewiarowski notes the humidity dependence of adhesion, approximately 2x increase in adhesion from 25%RH to 80%RH and suggests a hydrophilic setae despite evidence to the contrary and suggests capillary forces play an important role in gecko adhesion, but only provides a net conclusion that neither van der Waals nor capillary interactions adequately explains whole animal adhesion data.

Pesika et al. [Pesika 2009] notes changes in the wetting behavior of setal arrays after prolonged exposure to water. Initially the setal array as described by Autumn and Hansen [Autumn 2006b] is highly hydrophobic at θ = 160°, (note that for β-keratin of the gecko spectacle is θ = 93°, suggesting a surface geometry influence on water contact angle.) After exposure to de-ionized (DI) water for 20 minutes, a water droplet was pushed into the setal array surface; there is visible necking and a thin film of water remaining on the array upon retraction of the water droplet. This is a stark contrast to initially dry arrays, where the contact of the water droplet remains hydrophobic with no visible necking upon retraction of the water droplet or wicking into the array. Pesika hypothesizes the cause of the observed effect is due to surface changes of the β-keratin. Keratin hydration results in more hydrophilic proteins to be exposed on the free surface and, thus, an observed increased in adhesion and hydrophilic behavior. This is consistent with Huber et al. [Huber 2005], as he alluded to surface changes as a possible explanation of his data. However it does not provide an explanation for the increase of adhesion on hydrophobic surfaces. Pesika solves van der Waals adhesion to support the experimental results

$$F_{vdw} = \frac{A_{123}R}{6D^2} \qquad \text{Eqn. 1}$$

Where,

$$A_{123} = \underbrace{\frac{3}{2}kT\left(\frac{\varepsilon_1-\varepsilon_3}{\varepsilon_1+\varepsilon_3}\right)\left(\frac{\varepsilon_2-\varepsilon_3}{\varepsilon_2+\varepsilon_3}\right)}_{\text{Thermal energy}} + \underbrace{\frac{3hv_e}{8\sqrt{2}}x\frac{\left(n_1^2-n_3^2\right)\left(n_2^2-n_3^2\right)}{\left(n_1^2+n_3^2\right)^{1/2}\left(n_2^2+n_3^2\right)^{1/2}\left[\left(n_1^2+n_3^2\right)^{1/2}+\left(n_2^2+n_3^2\right)^{1/2}\right]}}_{\text{Photon energy}}$$

Eqn. 2

Where n_i and ε_i are dielectric constants and reflective indices of the media, *h* is Plank's constant and v_e is the absorption frequency in UV (~$3\text{x}10^{-15}$ s^{-1}). A_{123} is the Hamaker constant. The Hamaker constant for the setal array interacting with silica surface in water is $A_{123,\text{ water}} = 9.64\text{x}10^{-21}$ J and in vacuum is $A_{123,\text{ vacuum}} = 7.08\text{x}10^{-20}$ J, a difference of a factor of 7.34. Theoretical decrease in adhesion in water is in good agreement with the experimental results obtained with the setal array interacting with a silica surface in water and vacuum, lending confirmation to the van der Waals adhesion hypothesis.

Kim and Bhushan, using a multi-scale model, calculated the magnitude of capillary forces for contact between elements with varying degree of hydrophillicity/hydrophobicity [Kim and Bhushan 2008]. The model is in fair agreement with adhesion data from Huber [Huber 2005] for a hydrophilic substrate with a general increase in adhesion up to near 90%RH. However, the model disagrees with Huber's data on hydrophobic substrate, the model showing a decrease in adhesive force up to ~80%RH with an increase of adhesion thereafter. But there is no net increase of adhesion from 0% to 100%RH on the hydrophobic interfaces.

More recently, Chen et al. [Chen 2010] based on his previous works and prior adhesion research from others offers an alternative to the capillary model of adhesion and suggests material properties changes are responsible for the apparent increase in gecko adhesion with increasing humidity. Using commercially available FEA (Finite Element Analysis) software package Abaqus® to perform numerical simulations on vertical peeling of the spatula. Chen demonstrated apparent adhesion energy of an interface involving a thin pad depends strongly on the stiffness of the material. A 25-80% increase in peel-off force with 4x reduction in elastic modulii was noted depending on geometry. Chen published his work well after the commencement of this thesis work and submission/review of papers in Journal of Experimental Biology [Puthoff et al 2010] and Acta Biomaterialia [Prowse 2011], papers detailed in this thesis. Chen's work does however provide support for this study's findings and ultimate conclusions.

1.5 Adhesion Theory

Adhesion occurs on the molecular level. Such forces are very short range. Atmospheric contaminates such as water, volatile organics, and oxygen are known to reduce adhesion by orders of magnitude [Baley1967, Johnson et al 1971, Kendall 2001, Obreimoff 1930]. Thus molecular adhesion works best under high vacuum conditions. Most people attempt to apply macroscopic views to adhesion which are false. One assumes that mechanical fasteners such as mortise and tenon joints or even such fasteners as nails are the root to adhesion. That is, interlocking mechanical connection as observed with the unaided eye, scales down to the microscopic level - it does not. As Isaac Newton observed, the smoother he polished the surface of glass marbles the stronger their adhesion [Newton 1704, pg 397].

Johnson, Kendall and Roberts (JKR) [Johnson et al 1971] performed an experiment using two elastic rubber balls showed unequivocally that molecules jump into contact when separation is minimal (sub-micron scale). After the surfaces make contact the contact spot expands as the balls deform under the force of the molecular adhesion. The deformation stops once the elastic resistance of the rubber equilibrates with the adhesive force. The material properties have a substantial affect on this deformation process and the observed macroscopic adhesion.

Per Kendall [Kendall 2001], adhesion follows 3 basic laws. Adhesion force between atoms and molecules is considerable, that is when two bodies approach each other at the nanometer scale, the adhesion force is great enough that the surfaces will jump into contact. Wetting molecules or other contaminates reduce molecular adhesion or even make bodies repel one another. Finally, molecular adhesion is of such short range, many mechanisms can have a large influence even though molecular adhesion remains unchanged. These influential mechanisms are surface roughness, elastic deformation, viscous deformation, etc. The last two items are of particular interest for gecko adhesion, yet has not received much attention.

Surface contamination can greatly alter the adhesion between two surfaces. We are all familiar with the effects of water on adhesion. We use water as a cleaning agent as the water helps 'release' dirt from surfaces, we add water to clay to make it more malleable, paper falls apart when wet, etc. Early experiments in adhesion also noted the effects of contamination on adhesion. Isaac Newton noted two glass lenses would adhere less strongly once water was introduced [Newton 1704]. However, many of us also know empirically that water seems to act as an adhesive too. Any child building a sand castle can attest, only moistened sand stays together.

In a classic experiment, Obreimoff [Obreimoff 1930] cleaved mica under vacuum and repeated the experiment in air. The energy required to cleave a mica sheet in air dropped by a factor of 13. Bailey et al. [Bailey 1967] conducted a simple experiment using a transparent rubber ball and measuring the contact surface which is proportional to the work of adhesion. In dry conditions the work of adhesion was determined to be 71mJm^{-2}, but when the surfaces were immersed in water the work of adhesion dropped by a factor of 10 to 6.8mJm^{-2}. Clearly demonstrating contamination of the adhering surface with water diminished adhesion. It should be noted that the water contact angle for the rubber used by Bailey was 66 degrees (hydrophilic).

Condensing water in thin films has two effects. For wetting liquids in a narrow gap, capillary attraction resulting from the surface tension (γ) of the liquid and the curvature of the meniscus caused the Laplace pressure drop inside the capillary bridge (stretched water) can have substantial adhesion [Yang 2008]. The energy required to break capillary bridge is approximate to the energy of forming two new water surfaces (proportional to the foundation area of the meniscus). The second effect of thin film water in surface gaps is viscous resistance. Liquids tend to resist rapid separation, the more rapid the separation rate from a static state, greater the viscous resistance. McFarlane and Tabor [1950] determined the capillary adhesion F_{cap} (dynes) of a bead on a flat plane to be

$$F_{cap} = 4\pi R\gamma\cos\alpha \qquad \text{Eqn. 3}$$

Where R = radius of the bead, γ = surface tension of the liquid (water = 0.072N/m) and α = angle of contact between the liquid and solid.

From McFarlane and Tabor [1950] the contribution of humidity induced capillary adhesion, increased rapidly above 80%RH to be the dominating adhesion approaching 100%RH. For smaller geometries than those considered by McFarlane and Tabor [1950], capillary adhesion has been shown to peak at lower RH values [Asay 2010, Xu 1998]. Condensation of capillaries is also a time dependant phenomena, according to Szoszkiewicz [Szoszkiewicz 2005], nanoscale capillary formation requires ~4.2ms. Consequently, a sufficiently high shear rate will prevent capillary formation.

When the partial pressure of water in air, P_v, is less than the saturation partial pressure P_{sat}, condensation dominates over evaporation. Conversely, when $P_v > P_{sat}$, evaporation prevails over condensation. The ratio of P_v/P_{sat} is referred to as relative humidity. For a convex surface the equilibrium occurs when $P_v > P_{sat}$, i.e. over-saturated condition. This is not true for a concave interface where the equilibrium occurs $P_v < P_{sat}$, this is expressed by the Kelvin equation.

$$\gamma_{LV}\left(\frac{1}{R_x}+\frac{1}{R_y}\right) = \rho RTIn\frac{P_V}{P_{sat}} \qquad \text{Eqn. 4}$$

Where γ is the surface energy; R_x and R_y are radii of curvature in the x and y axis, respectively, R is the gas constant, T is temperature in Kelvin and density ρ. The Kelvin radius $R_k = (1/R_x + 1/R_y)^{-1}$. A concave meniscus may form at any humidity in accordance with the Kelvin equation. For low humidity the pressure difference inside and outside the capillary bridge is large, but the bridge size is small and may be of insufficient size to generate capillary force. Once the particles get too wet, nearing 100%RH, the meniscus becomes large; the radii of curvature become large, reducing the Laplace pressure to zero with the capillary contribution to adhesion dropping to approximately nil. The Laplace pressure is given by

$$\Delta P = \gamma(\frac{1}{R_x}+\frac{1}{R_y}) \qquad \text{Eqn. 5}$$

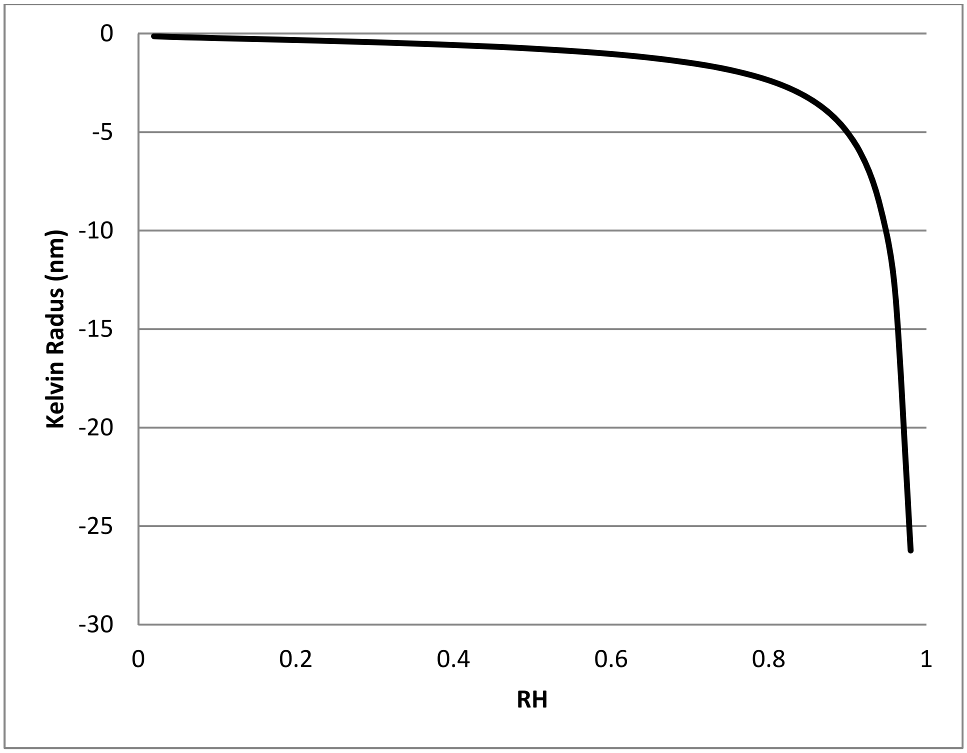

Figure 1.3. Kelvin radius (R_k) for water at T = 300K. Derived from equation 4, $R_k = 0.53/\ln(P_v/P_{sat})$ nm.

Van der Waals attraction is a relatively weak intermolecular force that arises from dipole interactions. There are two prominent interaction forces that are under the vdW umbrella. The Keesom/Debye forces, or 'zero-frequency' electrostatic interactions, act between dipolar-nondipolar and rotating dipolar interactions arising from thermal fluctuation in electric fields of neighboring molecules. The second vdW force is the London dispersion force, nondipolar-nondipolor interactions arising from resonant fluctuations in the electric fields of neighboring molecules.

Van der Waals attraction is very short range with $1/(x-d)^2$ dependence where, x is the separation distance between two spheres and d is the sphere diameter. This is a much more rapid decrease in attraction than Coulomb attraction which has an $1/r^2$ dependence, where r is the radius from the charged body. In the case of gecko adhesion the primary concern is London force and surface polarization. Moreover, Keeson/Debye and London dispersive energies cannot exceed 1/2kT, (where k is Boltzmann constant). For a very detailed explanation of vdW see reference [Parsegian 2006].

As pertaining to gecko adhesion, London dispersive forces dominate because the interaction takes place in air where dispersion is largely unretarded and screening by intervening solvent ions cannot take place.

1.7 Problem statement

Most traditional non-biological adhesives are either soft polymers with high visco-elastic loss (e.g. scotch tape) or substances that chemically react irreversibly to bond two surfaces (e.g. epoxy). While adhesives such as scotch tape can be removed from a surface, reuse is limited to no more than a couple of uses and often a single use as debris collects on the adhesive surface [Hansen 2005], often with residue remaining on the surface. Likewise thermo-set adhesives such as epoxy are single use. Mimicking gecko adhesives which are non-fouling and seem to offer unlimited reuse at least for the time frame of the molting cycle could offer advantages over traditional adhesives. Understanding the materials aspect of gecko adhesion is critical importance in making synthetic analogs.

In the capillary model of adhesion, it is expected to have little effect below ~80-90%RH, where there is a strong increase in adhesion as the capillary bridges begin to form [MacFarlane 1950]. Accordingly, the capillary model poorly explains the adhesion data of Huber et al [2005], Sun et al [2005], and Niewiarowski [2008]. In the case of Huber, the observed adhesion was approximately linear with %RH. Sun and Niewiarowski observed increased adhesion below the threshold where sufficient water condensation is present for capillary formation. Another issue with the capillary model is the observed increase in adhesion of the hydrophobic setae on hydrophobic surfaces. The poor explanation of the capillary model to adequately explain the humidity effect on gecko adhesion provides the impetus for this thesis. An unconsidered possible explanation to the observed changes in gecko setal adhesion is the changes in mechanical properties of the setae.

As a biological protein the β-keratin in the setae is susceptible to moisture, altering the mechanical response to strain. I will present data to support the hypothesis, that changes in mechanical properties with respect to humidity satisfactorily explain the observed increase in adhesion at high humidity. Mechanical response of a single seta and the smooth epidermal tissue (lamella) will be measured in tension to failure and under dynamic loading. Setal arrays will be measured in normal and shear force with varying humidities on hydrophobic gallium arsenide (GaAs), and hydrophilic glass (SiO_2) glass to determine adhesive forces relative to ambient humidity. SEM studies of fracture surfaces of the setae will be presented depicting the internal structure of the setae.

Additionally, initial surface chemical analysis of Tokay gecko tissue; setae, lamella (epidermal tissue underlying the setae) eye spectacle and scale, were measured using x-ray photoelectron spectroscopy (XPS) and near edge x-ray atomic fine structure (NEXAFS). I will present the initial data of the surface chemistry.

References

Aristotle Historia Animalium, Book IX. Oxford, UK: The Clarendon Press. Available online at http://classics.mit.edu/Aristotle/history_anim.mb.txt. (1910) *part 9*.

Alexander, P., Earland, **C.,** Structure of wool fibres, Nature, 166 (1950) 396-97.

Alibardi, L., Ultrastructural autoradiographic and immunocytochemical analysis of setae formation and keratinization in the digital pads of the gecko *Hemidactylus turcicus* (Gekkonidae, Reptilia). Tissue & Cell. 35 (2003) 288-296.

Alibardi, L., Edward, D.P., Patil, L., Bouhenni, R., Dhinojwala, A., and Niewiarwski, P.H., Histochemical and ultrastructural analysis of adhesive setae of lizards indicate that they contain lipids in addition to keratins. J. of Morph. 272 (2011) 758-768

Asay, D.B., de Boer, M.P., Kim, S.H., Equilibrium vapor adsorption and capillary force: exact -Young equation solution and circular approximation approaches. J. Adhesion Sci Technol. 24, (2010) 2363–2382

Autumn, K. and Peattie, A., Mechanisms of adhesion in geckos. Int. Comp. Bio. 42 (2002a) 1081–1090.

Autumn, K., Liang, Y.A., Hsieh, S.T., Zesch, W., Chan, W.P., Kenny, W.T., Fearing, R., Full, R.J., Adhesive force of a single gecko foot-hair, Nature. 405 (2000) 681-685.

Autumn, K., How Gecko Toes Stick, Amer. Sci. 94 (2006a) 124-132.

Autumn, K. , Sitti, M., Peattie, A., Hansen, W., Sponberg, S., Liang, Y.A., Kenny, T., Fearing, R., Israelachvili, J., Full, R.J., Evidence for van der Waals adhesion in gecko setae, Proc. Natl. Acad. Sci. 99 (2002b) 12252-12256.

Autumn, K., Dittmore, A., Santos, D., Spenko, M., and Cutkosky, M., Frictional adhesion: a new angle on gecko attachment. J. Exp. Biol (2006b) 209, 3569-3579

Autumn, K., Hansen, W., Ultrahydrophobicity indicates a non-adhesive default state in gecko setae. J. Comp. Physiol A. 192 (2006c) 1205-1212

Autumn, K., Majidi, C., Groff, R.E., Dittmore, A., and Fearing, R., Effective elastic modulus of isolated gecko setal arrays. J. Exp. Biol. 209 (2006d) 3558-3568

Bailey, A.I., kay, S. M., A Direct Measurement of the Influence of Vapour, of Liquid and of Orientated Monolayers on the Interfacial Energy of Mica, Proc. R. Soc. Lond. A, 301 (1967) 47-56

Barthlott, W., Schimmel, T., Wiersch, S., Kock, K., Brede, M., Barczewski, M., Walheim, S., Weis, A., Kaltenmaier, A., Leder, A., and Bohn, H.F., The Salvinia Paradox: Superhydrophibic Surfaces with Hydrophilic Pins for Air Retention Under Water, Adv. Mater. 22 (2010) 2325-2328

Bonser, R.H.C., Purslow, **P.P.,** The Young's Modulus of Feather Keratin, J. Exp. Biol., 198 (1995) 1029-1033.

Bonser, R.H.C., Hydration sensitivity of ostrich claw keratin, J. Mater. Sci. Lett. 21 (2002) 1563-1564.

Campolo, D., Jones, S.D. and Fearing, R.S., Fabrication of gecko foot-hair nano structures and adhesion to random rough surfaces, IEEE nano 2003

Chen, B., and H. Gao, An Alternative Explanation Of The Effect Of Humidity In Gecko Adhesion: Stiffness Reduction Enhances Adhesion On A Rough Surface International Journal of Applied Mechanics Vol. 2, No. 1 (2010) 1–9, Imperial

College Press.

Danilatos, G.D., Postle, R., Dynamic Mechanical Properties of Keratin Fibers During Water Adsorption and Desorption. J. of Appl. Poly. Sci. 26 (1981) 193-200

Dellit, W.-D. Zur anatomie und physiologie der Geckozehe. Jena Z. Nature. 68 (1934) 613-656.

Dirks, J.H. and Federle, W., Mechanisms of fluid production in smooth adhesive pads of insects. J.R. Soc. Interface, 8 (2011) 952-960

Eckhart, L., et al. Identification of reptilian genes encoding hair keratin-like proteins suggests a new scenario for the evolutionary origin of hair. Proc. Natl Acad.Sci. USA. 105 (2008) 18 419–18 423.

Federle, W., M. Riehle, A.S.G. Curtis and R.J. Full, An Integrative Study of Insect Adhesion: Mechanics and Wet Adhesion of Pretarsal Pads in Ants. Integr. Comp. Biol., 2002. 42 (6): pg. 1100.

Federle, W., W.J.P. Barnes, W. Baumgartner, P. Drechsler and J.M. Smith, Wet but not slippery: Boundary friction in tree frog adhesive toe pads. J. R. Soc. Interface, 2006. 3(10): pg. 689.

Feughelman, M. Mechanical Properties and Structure of Alpha-Keratin and Related Fibres; Wool, Human Hair and related Fibres, UNSW Press, USA, 1997.

Fisher, L. R. and Israelachvili, J. N. (1981). Direct measurement of the effect of meniscus forces on adhesion: a study of the applicability of macroscopic thermodynamics to microscopic liquid interfaces. Colloids Surf. 3, 303-319.

Fraser, R.D.B., and Macrae, T.P., Molecular and mechanical structure of keratins, Symp. Soc. Exp. Biol. 34 (1980) 211-246

Fraser, R.D.B., Parry, D.A.D., The Molecular Structure of Reptilian Keratin. International J. of Bio. Macromolecules. 19 (1996) 207-211

Geim, A. K., Dubonos, S. V., Grigorieva, I. V., Novoselov, K. S., Zhukov, A. A. and Shapoval, S. Y. Microfabricated adhesive mimicking gecko foot-hair. Nat. Mater. 2 (2003) 461-463.

Gillispie, J.M., Haylett, T., Lindley, **H.,** Evidence of homology in high-sulphur protein fraction (SCMK-B2) of wool and hair α-keratin, Biochem J. 110 (1968) 193-200

Hansen, W.R., and Autumn, K., Evidence for self-cleaning in gecko setae. Proc. Natl. Acad. Sci. (2005) 102, 385-389

Hiller, U., Comparative studies on the functional morphology of two gekkonid lizards, J. of the Bombay Natural History Soc. 73 (1975) 278-282

Huber, G., Mantz, H., Spolenak, R., Mecke, K., Jacobs, K., Gorb, S., Arzt, E., Evidence for capillarity contributions to gecko adhesion from single spatula nanomechanical measurements. Proc. Nat. Acad. Sci. 102 (2005) 16293-16296.

Huber, G., Orso, S., Spolenak, R., Wegst, U.G.K., Enders, S., Gorb, S., Arzt, E., *Mechanical Properties of a Single Gecko Seta*. Int. J. Mat. Res. 99 (2008) 1113-1118

Huber, G., 2006. Nanoscale adhesion of individual gecko spatulae explored by atomic force microscopy. Ph.D. Thesis

Irschick, D., Austin, A., Petren, K. Fisher, R.N., Losos, J.B. Ellers, O., A compariative analysis of clinging ability among pad-bearing lizards. Bio. J. of the Linnean Soc. 59 (1996) 21-35

Israelachvili, J., Intermolecular and Surface Forces, Academic Press, New York, 1992.

Johnson, K.L., Kendall, K., Roberts, A.D., Surface Energy and the Contact of Elastic Solids. Proc. R. Soc. Lond. A, 324**,** 1558 (1971) 301-313.

Kendall, K., The Connection Between Fracture Energy and the Inelastic Behavior. Acta Metall. 27 (1979) 1065-1073

Kendall, K., Molecular Adhesion and Its Applications. Khuwer Academic Publishers, New York, 2001

Kim, T. W. and Bhushan, B. The adhesion model considering capillarity for gecko attachment system. J. R. Soc. Interface 5, (2008) 319-327.

Kitchener, A., Vincent, J.F.V., Composite theory and the effect of water on the stiffness of horn keratin, J. of Mat. Sci. 22 (1987) 1385-1389

Lacari, J., Swanson, D.W., Adhesion Technology for Electronic Applications, Materails, Proecesses, Reliability. William Andrew Inc., (2005) pg. 206

Lee, J., Bush, B., Maboudian, R. and Fearing, R. S. Gecko-Inspired combinedlamellar and nanofibrillar array for adhesion on nonplanar surface. Langmuir, 25 (2009) 12449-12453.

Liangti, Q., Liming, D., and Stone, M., Carbon nanotube arrays with strong shear binding-on and easy normal lifting-off, Science 322 (2008) 238-242

Lin, A.Y.M., Brunner, R., Chen, P.Y., Talke, F.E., Meyers, M.A., Underwater adhesion of abalone: The role of van der Waals and capillary forces, Acta Mater. 57 (2007) 4178-4185

Lindley, H., Cranston, **R.W.,** The reactivity of the disulphide bonds of wool, Biochem J. 139 (1974) 515-523

Maderson, P.F.A., Keratinized epidermal derivatives as an aid to climbing in gekkoid lizards. Nature 203 (1964) 780-781

Mahdavi, A., Ferreira, L., Sundback, C., Nichol, J. W., Chan, E. P., Carter, D. J. D.,Bettinger, C. J., Patanavanich, S., Chignozha, L., Ben-Joseph, E. et al. A biodegradable and biocompatible gecko-inspired tissue adhesive. Proc. Natl. Acad. Sci. USA 105, (2008) 2307-2312.

McFarlane, J.S., Tabor, D., Adhesion of solids and the effect of surface films,Proc. R. Soc. Lond. A, 202 (1950) 224-243.

Mittel, K.L., Contact Angle, Weetability and Adhesion. Koninklijke Brill NV, The Netherlands, (2009) pg. 292

Newton, **I.,** Opticks, Smith and Walford, London 1704 (reprinted Dover, New York, 1952)

Niewiarowski, P. H., Lopez, S., Ge, L., Hagan, E., Dhinojwala, A., Sticky Gecko Feet: The Role of Temperature and Humidity. PLoS ONE 3 (2008) e2192.

Nosonovsky,M., and B. Bhushan,B., Capillay Adhesion and Nanoscale Properties of Water; Scanning Probe Microscopy in Nanoscience and Nanotechnology 2. Springer 2011 B Bhushan ed.

Obreimoff, **J.W.,** The Splitting Strength of Mica, Proc. R. Soc. Lond. A. 127 (1930) 290-297

Parsegian, V. van der Waals forces, a handbook for biologists, chemists, engineers, and physicists, Cambridge University Press, New York, 2006.

Pauling, L., Corey, R.B., Compound Helical Configurations of Polypeptide Chains: Structure of Proteins of the α-Keratin Type. Nature no. 4341, 1953

Peattie, A.M., Majidi, C., Corder, A., Fuller, R.J., Ancestrally High Elastic Modulud of Gecko Setal β-Keratin. J.R. Soc. Interface. 4 (2007) 1071-1076

Persson, B.N.J., Wet adhesion with application to tree frog adhesive toe pads and tires. J. Phys.-Condens. Mat., 2007. 19 (37): pg. 376110.

Pesika, N.S., Zeng, H., Kristiansen, K., Zhao, B., Tian, Y., Autumn, K.. Isrealachvili, J., Gecko adhesion pad: a smart surface? J. Phys.-Condens. Mat., 2009. 21 (46) 2009 464132.

Peters, L., Woods, **H.J.,** Protein fibres, In The Mechanical Properties of Textile Fibres, R. Meredith, ed. North Holland Publishing Company, Amsterdam, 1955. pg. 151-244

Prowse, M.S., Puthoff, J.B., Wilkinson, M., Autumn, K., Effects of Humidity on the Mechanical Properties of Gecko Setae. Acta Biomaterialia. 7 (2011) 733-738

Puthoff, J.B., Prowse, M.S., Wilkinson, M., Autumn, K., Changes in Materials Properties Explain the Effects of Humidity on Gecko Adhesion, J. Exp. Biol. 213 (2010) 3699-3704

Rizzo, N.W., Garner, K.H., Walls, D.J., Keiper-Hrynko, N.M., Ganzke, T.S., Hallahan, D.L., Characterization of the Structure and Composition of Gecko Adhesive Setae. J.R. Soc. Interface 3 (2005) 441-451

Ruibal, R. and Ernst, V., The structure of the digital setae lizards. J. Morphol. 117 (1965) 271-293

Setti, M., Fearing, R.S., Synthetic gecko foot-hair mirco/nano-structure as dry adhesives. J. Adhes. Sci. Technol. 17 (2003) 1055-1073.

Speakerman, J.B., The rigidity of wool and its change with adsorption of water vapour**,** Trans Faraday Soc. 25 (1929) 92.

Sun, W., Neuzil, P., Kustandi, T. S., Oh, S. and Samper, V. D. (2005). The nature Of the gecko lizard adhesive force. Biophys. J. 89, L14-L17.

Szoszkiewicz, R., Riedo, **E.,** Nucleation Time of Nanoscale Water Bridges. Phys. Rev. Lett. **95** (13) 2005 135502.

Taylor, A.M., Bonser, R.H.C., Farrent, **J.W.,** The influence of hydration on the tensile and compressive properties of avian keratinous tissue. J. Mater. Sci. 39 (2004) 939-942.

Thomson, W. On the equilibrium of a vapour at a curved surface of liquid. Phil.Mag. 42 (1871) 448-452.

Thundat T., Zheng, X.Y., Chen, G.Y., Warmack, R.J., Role of relative humidity in atomic force microscopy imaging, Surf. Sci. Lett. 294 (1993) L939-L943

Vincent, J.F.V., Structural Biomaterials. Princton University Press, New Jersey, 1990

Vincent, J.F.V., Biomechaincs: Materails: A Practical Approach. Oxford University Press, New York, 1992

Wainwright, S.A., Biggs, W.D., Currey, J.D., Gosline, J.M., Mechanical design in organisms, Edward Arnold, London, 1976. pg. 187-191

West, G.W., Haley, A.R., Feughelman, M., Physical Properties of Wool Fibers at Various Regains, Tex. Res. J. (1961) 899-904

Xu, L., Lio, A., Hu, J., Ogletree, D.F., Salmeron, **M.,** Wetting and capillary phenomena of water on mica. J. Phys. Chem. B 102 (1998) 540–548

Yamaguchi, T., Gravish, N., Autumn, K., and Creton, C., Microscopic modeling of the dynamics of frictional adhesives in the gecko attachment. J. Phys. Chem. B, 113 (2009) 3622-3628

Yang, S.-H., Nosonovsky, M.,Zhang, H.,Chung, K.-H., Negative pressure in water Capillary bridges at nanocontacts. Chem. Phys. Lett. 451 (2008) 88–92

Chapter 2

Methods and materials

2.1 RoboToe

Traditional mechanical properties testing methods, Instron or atomic force microscopy (AFM) do not offer the either the force range required for testing setae or setal arrays or correct geometries needed. Therefore, using a specially designed apparatus at Lewis and Clark College, gecko setae and setal arrays can be mechanically tested under a variety of environmental conditions with various loads and geometries [Gravish 2010]. The mechanical testing apparatus is securely mounted in an environmental chamber (Electro-Tech system inc. model 5503-00) capabilities of the chamber are limited by the 2-axis stage motors to humidities from 0%RH to 80% RH and temperature range from 0°C to 55°C. The environmental chamber can be both manually and remotely controlled using RT3 software. The apparatus is located inside a class 1000 clean room located on the ground floor of the Lewis and Clark BoDine building.

For individual setae measurements, a single axis quartz piezo-load cell is mounted opposing a 2-axis stage is better than 10nm resolution (Aerotech model ANT-50L). The quartz peizo-load cell, Kistler type 9207 and analog to digital amplifier is capable of 0.084mN resolution. For setal array and lamellae measurement, a Kistler 3-axis piezo load cell was utilized with resolution of 2.67mN in normal force, 1.3mN in shear [Gravish 2010]. *See figure* 2.1.

All hardware components are connected to a PC running RoboToe (RT3), a software application specially written with LabView (National Scientific). RT3 controls the movement of the 2-axis stage and data acquisition for the load cell, camera, and the environmental chamber controlling both temperature and humidity. The data output for the RT3 is written for IGOR, a technical graphing and data analysis software.

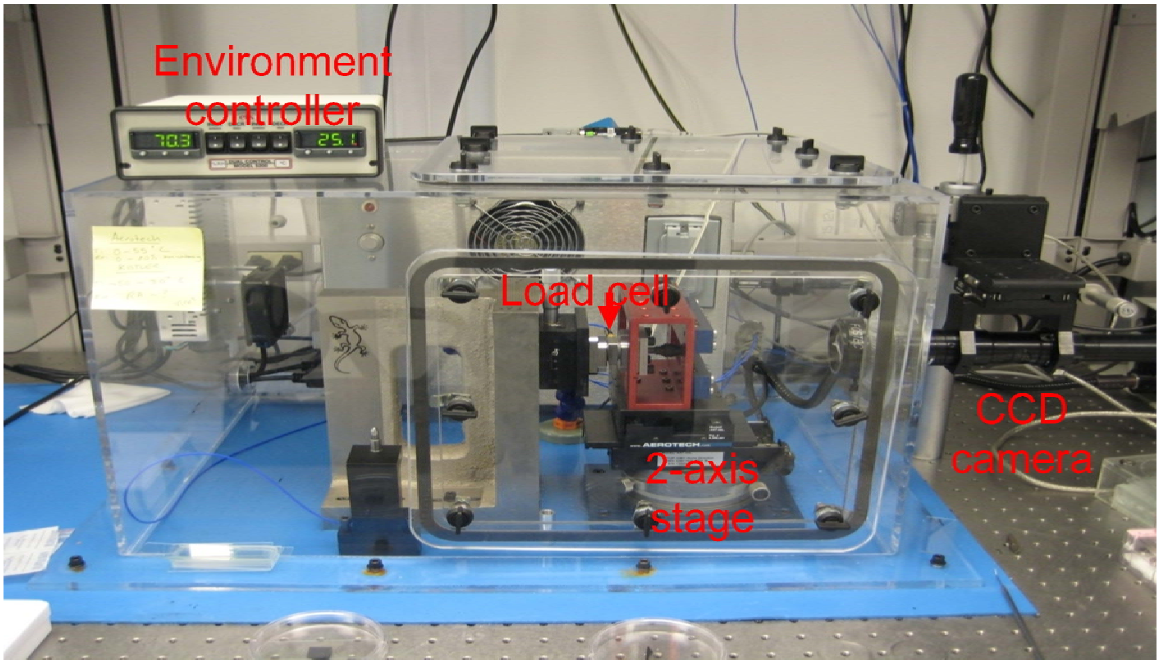

Figure 2.1. RoboToe apparatus in Autumn lab at Lewis and Clark College. A tombstone with rigidly mounted piezoelectric force sensor mounted opposite an Aerotech x-y motorized stage, in a clear poly enclosure with temperature and humidity controls.

2.2 Tensile testing

Both the single and 3-axis piezo load cells were calibrated using a precision 1g weight. An additional test case using American Fine Wire alloy AW8 (99.99% Au) bonding wire with a diameter .001" (25.8um) was tested to verify accuracy of the single axis system. Published specifications [americanfinewire.com], for the bonding wire, elongation of 4-7% at a minimum tensile load of 7.5g with typical failure load of 10g. Elongation at fail was experimental determined to be 3.5% at a load of 9g. The variation to the published values was attributed to the slight amount of handling damage but remained in expected value range.

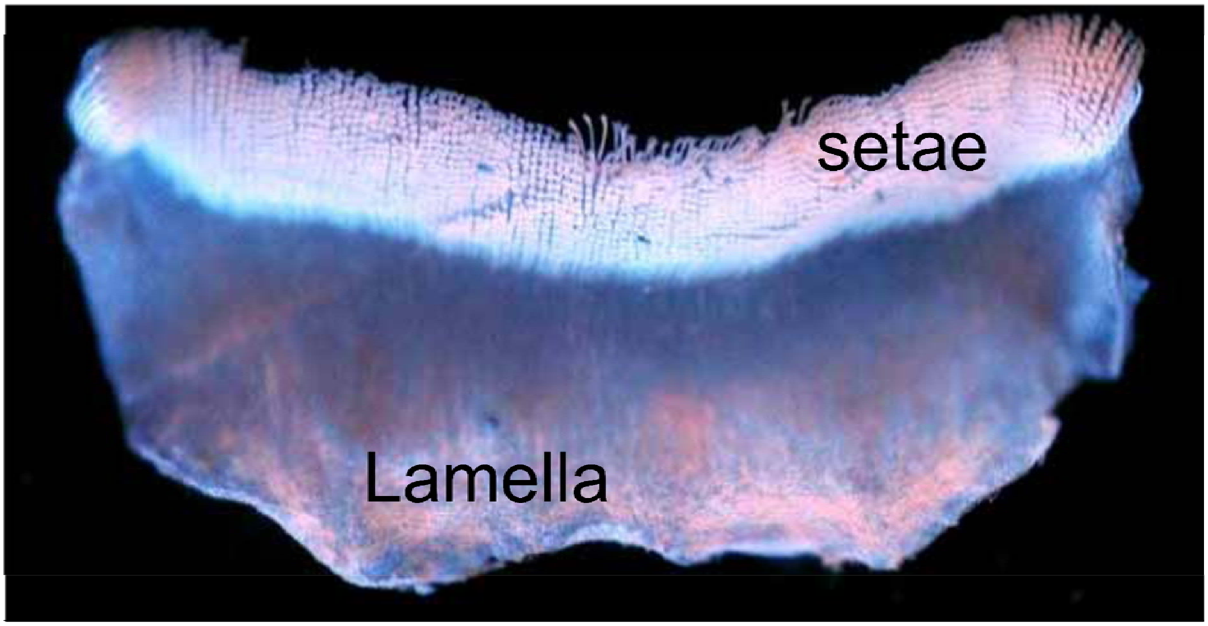

Figure 2.2, An isolated setal array as separated from a Tokay gecko. The epidermal layer (lamella) can be separated from the setae using a razor blade. Arrays measure ~1x1.5mm.

After separating setae from the backing tissue (*see figure* 2.2), an individual gecko seta is glued to the end of a fine stainless steel minutien pin (F.S.T. 0.1mm x 10mm) with Loctite® 4210 (cyanoacrylate). *See figure* 2.3. Loctite 4210 is used due to the black coloration makes it more visible under low and high magnification. The pin is then glued to a glass microscope slide, rigidly mounted on the 2-axis motorized stage. Using high magnification CCD camera the stage is moved to the load cell where a small amount of Loctite is used to secure the free end of the seta to the load cell. The glue was allowed to partially dry before contacting the seta to prevent wicking. The glue is then allowed to cure for 6-24 hours before the loading experiment proceeds.

An image is saved once the final setup is complete and dimension determined using RT3 calibrated CCD camera. The minutien pin also provides an in-situ redundant dimension calibration. Statistical SEM measurements were used for the setae diameter as the optical measurements were not precise enough to measure the diameter of the seta. The setal diameter was determined to be 3.3μm ± 0.3μm; length dimension was approximately 110μm to 125μm. Total length of the seta once secured to RT3 was 65μm to 80μm.

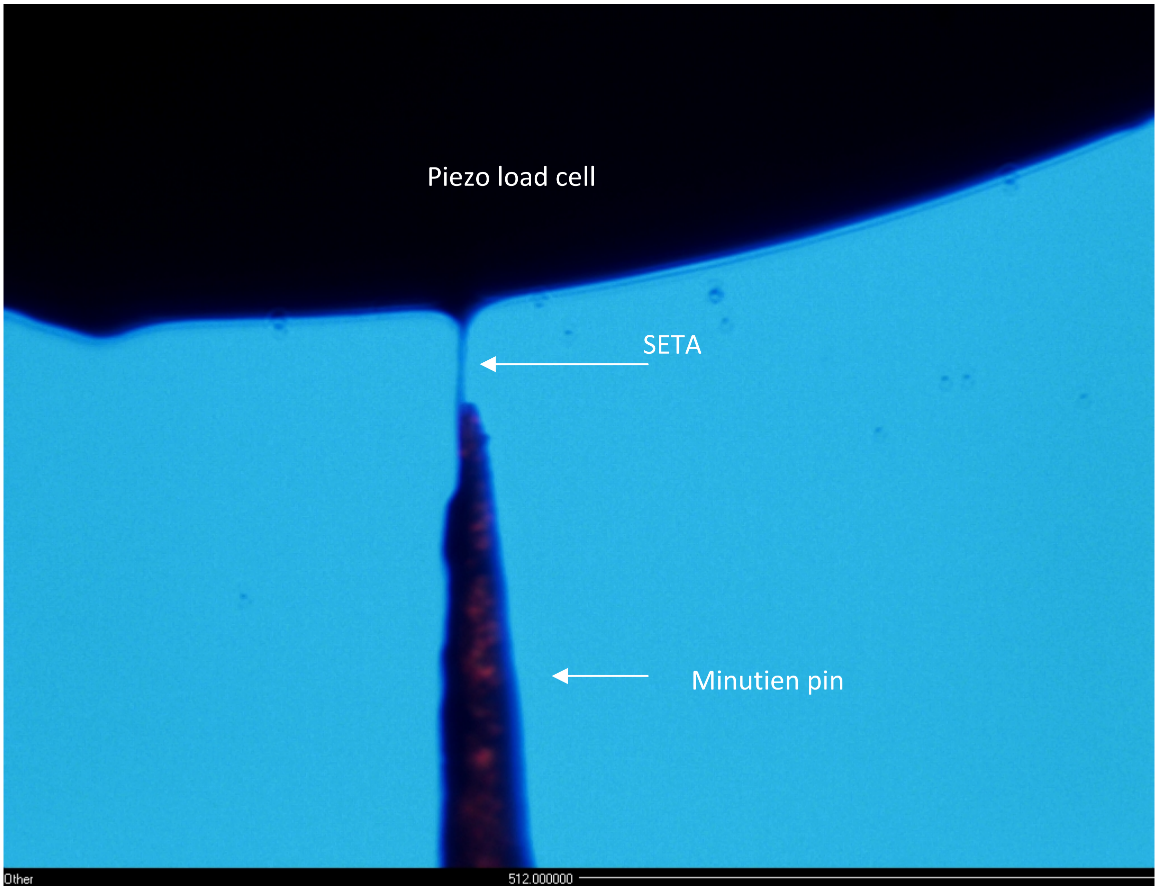

Figure 2.3 A single gecko seta mounted for tensile/DMA testing. The seta is mounted to the tip of a fine minutien pin secured opposing the piezo load cell. Scale bar 512 μm.

Pull rates were kept ≤ 5μm/sec which correlates to a maximum strain rates of ~7% per second for individual seta tests. The high strain rates were needed to ensure minimal drifting of the piezo cell so that it did not contribute to the data for the time of the experiment. Drift correction was not used for setae testing.

Slippage of the seta out of the cured glue was a recurring issue, particularly at higher humidities. Typically the spatula end of setae stayed embedded in the glue during loading; however the root end tended to come unattached from the glue particularly at high humidity. Using setae with the root greatly improved the pull out issue as the roughness of the root increase adhesion with the glue. Determination of 'pull-out' was straight forward from analyzing the data and post test images of the setae.

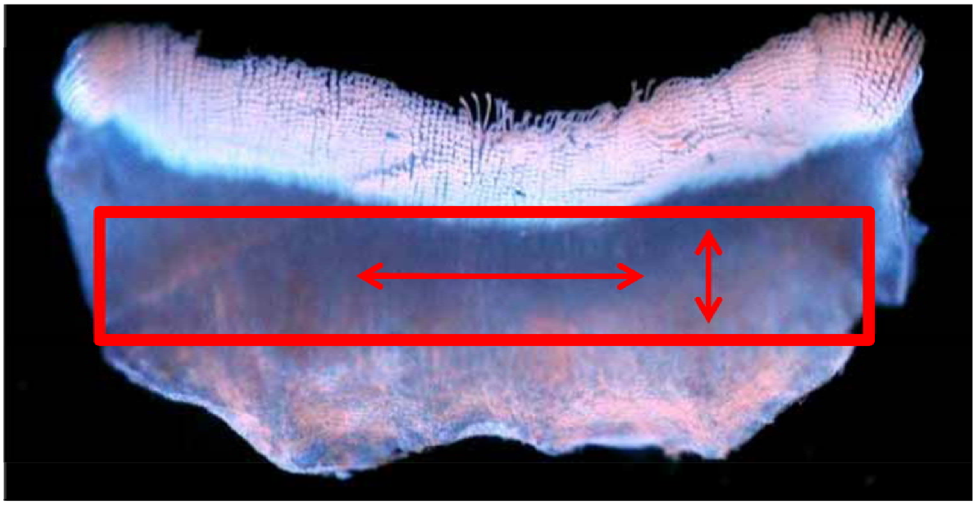

Figure 2.4. Schematic of a lamella sectioned (red box) for testing with directions of applied loads during DMA and tensile testing

The lamellae were cut from the setal arrays (*see figure* 2.4) into rectangular sections approximately 0.75 x 1.1mm and glued using Loctite 4210 to the edge of a glass microscope slide. S*ee figure* 2.5. The slide was then rigidly mounted on the 2-axis motorized stage. Using high magnification CCD camera the stage is moved to the load cell where a small amount of Loctite is used to secure the free end of the lamella to the load cell. Lamella thickness was measured optically using a Nikon stereo microscope model SMZ 1500.

Once the lamella was secured, an automated routine in RT3 properly aligned the sample. The routine would slowly tense the lamella and measure the forces in the y direction (tensile) and the x (perpendicular plane), then make any stage position corrections to ensure there are no out of plain forces. The lamella was allowed to acclimatize for a minimum of 2hrs prior to the testing. The strain rate for tensile testing was 2%/sec (~0.02 mm/sec).

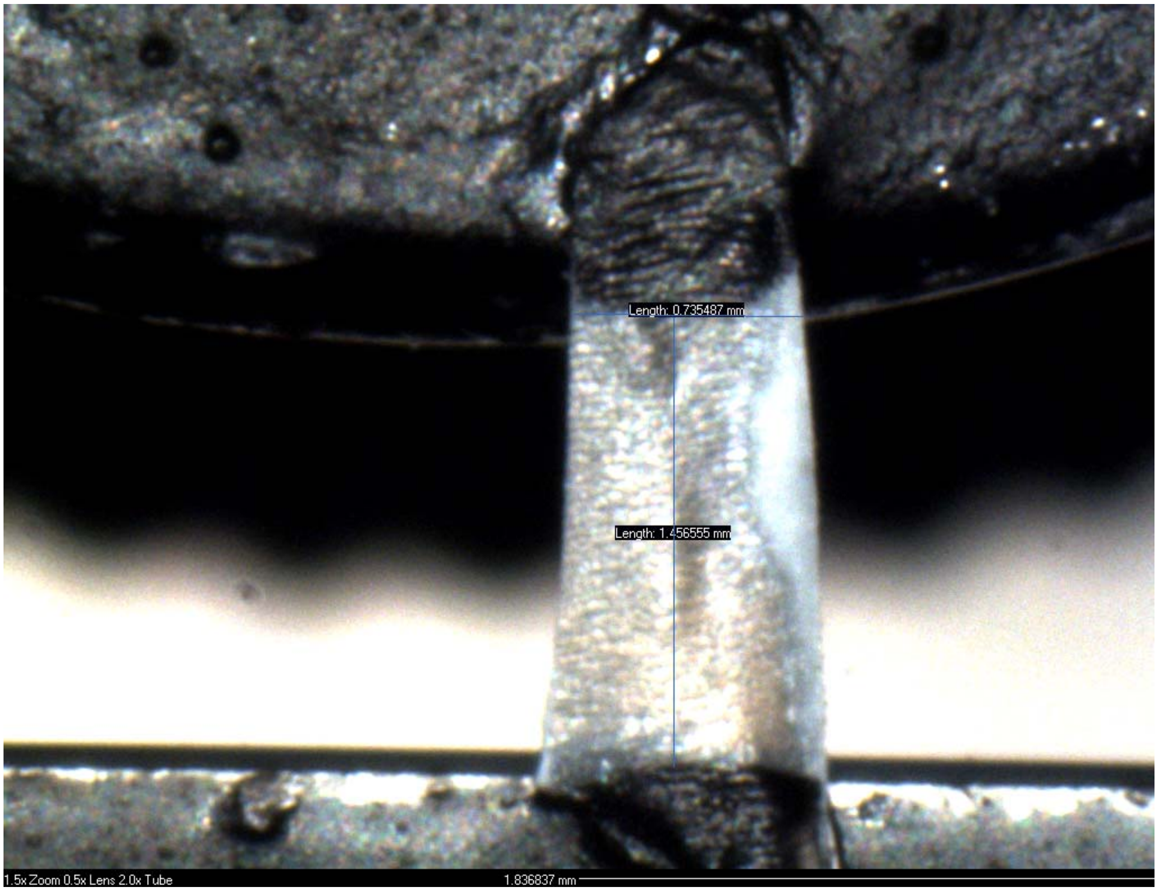

Figure 2.5. A single lamella mounted for tensile/DMA testing loaded perpendicular to the setae growth. The lamella is mounted on a glass microscope slide (bottom) and secured to a peizo load cell (top). Optical measurements of dimensions are displayed, 0.74x1.45mm. Tensile and DMA measurements were made on the lamellae in orientations perpendicular and parallel to the setae growth.

2.3 Dynamic Mechanical Analysis

In dynamic mechanical analysis (DMA), an applied force (stress) corresponds to strain (deformation) of the specimen. *See figure* 2.6

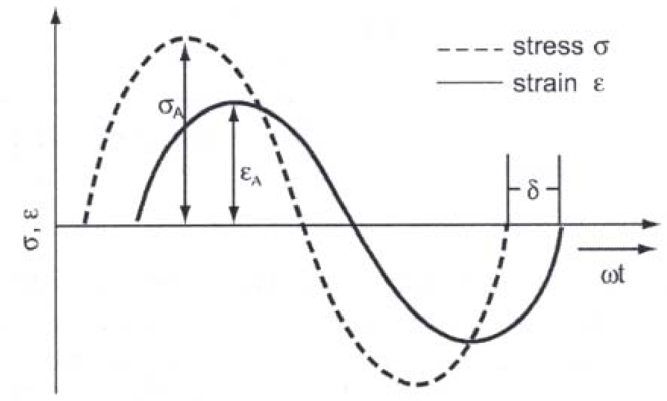

Figure 2.6 Schematic representation of the stress-strain behavior under sinusoidal loading.

Where,

$\varepsilon = \varepsilon_o \sin(\omega t)$ Strain (1)

$\sigma = \sigma_o \sin(\omega t + \delta)$ Stress (2)

The complex or dynamic modulus E* is the ratio of stress/strain and represents the stiffness of the material. The magnitude is:

$|E^*| = \sigma_A/\varepsilon_A = \sqrt{(E')^2 + (E'')^2}$ Dynamic/complex modulus (3)

E' and E" are related by a dimensionless loss tangent

$\tan\delta = E''/E'$ (6)

The complex modulus is composed of the storage modulus, E' and the loss modulus E". E' is the real part whereas E" is the imaginary part, the magnitudes of which depend on the material, measuring frequency and the environmental/specimen conditions. The stress response has the same frequency and the input excitation in the linear visco-elastic range. The analytical parameters are the amplitude of the stress, deformation and the time displacement (δ/ω) between deformation and stress.

The loss modulus, E", is proportional to the energy dissipated during the loading cycle and is the energy that is unrecoverable. The storage modulus, E', represents the visco-elastic stiffness and is proportional to the energy stored during the loading cycle. The storage modulus is roughly approximate to the elastic modulus under a single rapid stress at low strain and is the reversible deformation.

Physically the loss tangent is a measure of the energy loss during deformation expressed in terms of recoverable energy. It is dimensionless and represents mechanical damping in the system. A large loss tangent indicates a material has a large non-elastic strain component. A low tangent loss indicates a material that has small non-elastic strain component and thusly more elastic. At higher frequencies the loss tangent decreases as time dependant portion of the viscoelasticity decreases, although polymers never become purely elastic even at high oscillation frequencies.

In a purely elastic material, the stress and deformation (strain) are in phase ($\delta=0$). Therefore the complex modulus is equivalent to the storage modulus, $E^* \approx E'$. Steels are an example of nearly pure elastic materials. In purely viscous materials the phase angle is 90 degrees. Thusly, the complex modulus is equal to the loss modulus, $E^* = E''$.

2.3.1 DMA Testing

Dynamic measurements were carried out using the same experimental setup as the tensile testing except with cyclic loading for the setae and lamella, respectively. The testing apparatus was not capable of sinusoidal cyclic frequencies of greater than 20Hz. Consequently, all data was collected well below 20Hz, typically at 0.5Hz to 10Hz. Strain was nominally 2-4% as the apparatus incapable of sinusoidal movements of $\leq$ 2% strain for the setae. This nominal strain was also used for the lamellae testing for consistency.

RT3 was programmed to compensate for the swelling of the lamella during the humidity DMA measurements to ensure proper tension at higher humidities. After acclimatizing for 2hrs, an automated routine tensed the sample to 0.02N for lamella to adjust the starting position. For the setae samples the tensing was done manually.

2.4 Adhesion and friction testing

RT3 was used for the setal array measurement of adhesion and friction. Setal arrays were cut from lamella and glued with Loctite® 4210 (cyanoacrylate) on a SEM stub. The stub is securely mounted in a chuck on the 3-axis piezo load cell in RT3. Either GaAs wafer or soda-lime glass microscope slide is mounted on the motorized stage. The previously unused glass slide and GaAs wafers were cleaned with ethanol, acetone, and DI water to remove any surface contamination. There is no stable native oxide on GaAs so there was no need for any oxide removal step.

An automated routine in RT3 determined the contact position of the array to the substrate prior to testing. The arrays were brought into contact with the substrate and dragged in a movement mimicking a gecko footfall. Typical drag durations were 2-4 seconds at rate of 5-100μm/sec, before the array is moved away from the substrate.

2.5 Data Analysis

Data analysis on the dynamic testing was performed using a LabView macro specifically written to analyze the stress/strain wave forms. The macro used sine wave best fit technique and calculated the frequency (redundant check), stress/strain amplitude, and frequency delta. The macro also corrected for piezo sensor drift and incorporated a smoothing function to reduce noise in the wave analysis.

Tensile data analysis was straightforward using Microsoft Excel and SigmaPlot. Excel was also used for the statistical calculation for tensile and DMA results. Adhesion/friction data was analyzed using IGOR and Mathcad.

References

Gravish, N., Wilkinson, M., Autumn, K., Frictional and Elastic energy in Gecko Adhesive Detachment. J.R. Soc. Interface, 5 (2008) 339-348.

www.americanfinewire.com, Nov. 2008

Chapter 3

Effects of Humidity on the Mechanical Properties of Gecko Setal Beta-Keratin

Beta-keratin is a fairly low molecular weight (10-20kDa) biological polymer that forms a discontinuous fiber composite [Rizzo 2005, Lingham-Soliar 2009, Toni 2007]. Intermolecular bonding is primarily hydrogen bonding with small degree of disulfide bridges between cystine peptides. The matrix is highly susceptible to moisture due to a combination of high degree of hydrogen bonding, amorphous structure, and lower density.

3.1 Keratin Structure

Keratins are a class of proteins that are highly durable, pliable, chemically ill-defined, and un-reactive in natural environments. Keratin forms many appendages such as feathers, scales, hair, nails, and claws. They are most often found in higher vertebrates; reptiles, birds, and mammals [Fraser 1971, Fraser and Macrae 1980 etc].

There are three main forms of keratin: α, β, and amorphous. Although there is a distinction between amorphous keratin and other forms, the crystallinity found in both α- and β-keratins is on the order of 20-35% [Fraser 1972]. Alpha-keratin is helical in structure and is commonly found in mammals. Beta-keratin is found in birds and reptiles where the structure is a twisted β-sheet [Fraser 1972, Fraser 1996], and is readily differentiated from α-keratin structure by x-ray diffraction. In the twisted beta sheet model, keratin molecules are arranged anti-parallel, and form an inter-chain hydrogen-bonding network between the N-H groups (amide hydrogen) in one backbone and C=O groups (carboxyl oxygen) in the adjacent strand. Inter-molecular forces stabilize inter-sheet interactions. The strands exhibit a right-hand twist with a pitch of ~95 Å [Fraser 1996]. See figure 3.1.

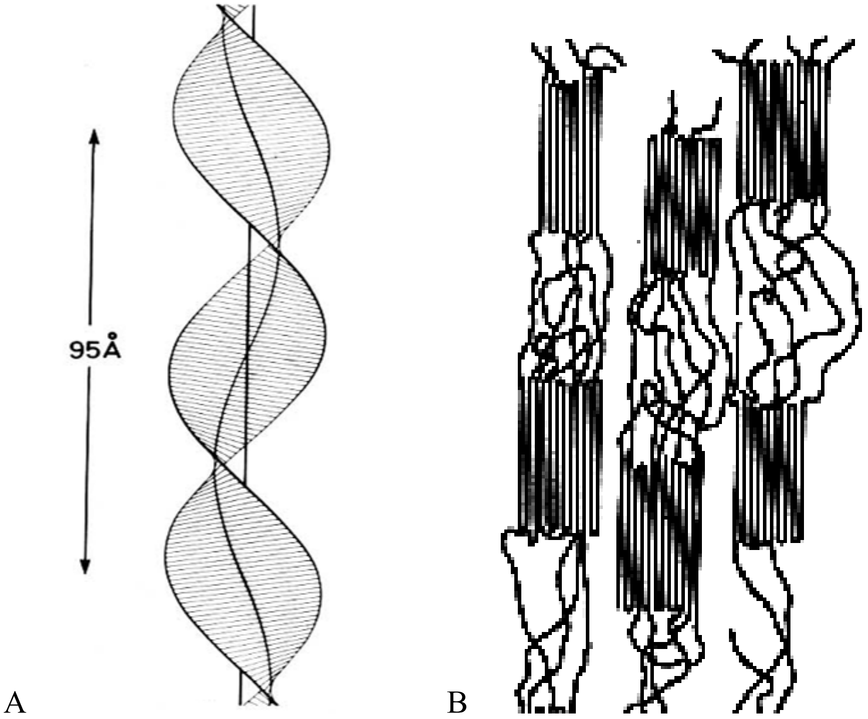

Figure 3.1,A) Helical structure with ~95 Å pitch. B). Schematic representation of the crystalline and amorphous regions, crystalline regions represent only 20-35% for β-keratin, the remaining volume is amorphous. The keratin strands form larger fibril bundles, in setae the bundles are ~200nm in diameter.

In both α-keratin and β-keratin microfibrils, there are two distinct mechanical phases, with microfibrils in a non-fibrous matrix. The matrix appears to have no secondary structure consisting of globular and amorphous polypeptides [Fraser 2008]. In feather rachis the β-keratin contributes to both the matrix and microfibrils [Fraser 2008]. The microfibrils are bundled into larger filaments up to 6μm in diameter that are embedded in an additional matrix material [Lingham-Soliar 2009] in feather rachis. For gecko setae, the larger fibril bundles are embedded in a lipid based matrix [Alibardi 2011]. Disulfide bridges are stronger (60 kcal/mol verses hydrogen bonds at 8-40KJ/mol) but far less numerous than the hydrogen bonds in keratin and are most in the keratin matrix [Fraser 1972].

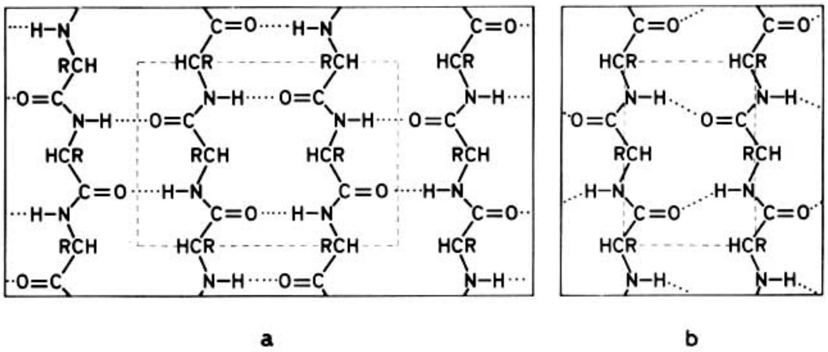

Figure 3.2 Hydrogen bonding in β-keratin a) anti-parallel chain and b) parallel chain. The repeating unit is enclosed in the dashed line. Configuration 'a' is more stable and is the configuration seen in β-keratin, typified in reptiles and birds.

Beta-keratin helical structure was first described by Pauling and Corey in 1953 [Pauling 1953]. In β-keratin the molecular chains are nearly fully extended, the strands are arranged in an anti-parallel manner. *See figure* 3.2. This arrangement is more stable than a parallel arrangement since the hydrogen bond length is shorter. The β-sheet conformation is maintained by the hydrogen bonding between the carboxyl and amide groups on the adjacent polypeptides. Successive side chains of each strand extend in opposite directions and therefore interact with the environment, neighboring strands, or matrix.

3.1.1 Alpha-keratin to β-keratin transformation

As hard mammalian α-keratins are stretched, the characteristic x-ray α-pattern decreases and is replaced by the β-pattern [Ashbury 1931 and 1933, Bendit 1957 and 1960]. Typically, the strongest β-patterns are obtained when the fibers are stretched in steam under constant load with extension of 90% to 100%. The transition involved stretching of the molecules and the β-form to consist of near fully extended polypeptide molecules aggregated into sheets stabilized by intermolecular hydrogen bonds. X-ray diffraction studies of the α→β transition also show that the crystallites grow more rapidly parallel to the plane of the sheets. The transition is important as it provides a link between the two forms of keratin.

3.2 Effects of Moisture on keratin

Being a biological polymer with extensive hydrogen bonding keratin is susceptible to moisture effects. Hydrogen bonds at 8-40KJ/mol are far weaker than covalent bonding, C-C (347KJ/mol) or C-N (291 KJ/mol), but the large number of such bonds in biological proteins results in a substantial contribution. Moisture can have a profound effect on keratin reducing the elastic modulus by approximately 3-fold at 100% humidity compared to dry. The effect has been observed for both α- and β-keratin and are well documented [Fraser 1972, Fraser 1996, Fraser 1980, Speakerman 1929, Kitchener 1987, Danilatos 1981, West 1961, Feughelman 1997, Bonser 1995, Bonser 2002, Taylor 2004, Maeda 1989, Leeder 1965 Mukherjee 2000, Peters and Woods 1955, Druhala 1974, Seki 2005].

Surrounding the bundles of polypeptide chains forming fibrils is the matrix. The matrix is mostly composed of amorphous and globular keratin proteins. In keratins, the amorphous matrix is rich in sulfur containing cystine.

Water absorbs into keratin in 2 phases according to King et al. [King 1945]. The first phase roughly follows Fick's law of diffusion. This initial phase is followed by a much slower phase of water absorption. The second phase is characterized by structural readjustment due to the absorption of water in the first phase. Maximum weight of absorbed water at saturation was 32% in keratin. King also confirms there are no capillary contributions to water absorption.

With water absorption, it is noted that the shear modulus is more affected than the elastic modulus. The elastic modulus is reduced by a factor of 3 with a change from dry to wet while the shear modulus in reduced by a factor of 15 [Fraser 1972, Fraser 1980, Feughelman 1997, Mitchell 1960, Bendit 1968]. The large differential between shear and elastic modulus lead to a conclusion that the matrix absorbs water and becomes less stiff while the fibrils are either not affected or only absorb a very small amount of water.

Fraser et al. [Fraser 1971] studing x-ray diffraction patterns of mammalian keratin determined volume swelling due to water absorption was largely confined to the matrix. He estimated volume swelling due to water adsorption of the matrix is 53% and swelling of the fibrils was 11%. The large degree of swelling within the matrix indicates the water must primarily be outside of the matrix protein as the matrix proteins have a high degree of cross-linking due to cystine. Additionally, more than half the protein in the fibrils do not interact with water, as Fraser et al. confirmed that the amide N-H groups do not convert to $N\text{-}^2H$ when saturated with heavy water (^2H_2O) [Fraser 1958]. It is reasonable to conclude with the available data that water forms a hydrogen bonded network within and interacting with the matrix proteins of the keratin.

Water is able to infiltrate into the keratin matrix, displacing the inter-polypeptide hydrogen bonds with peptide side group-water hydrogen bond. Water absorption initiates at the polar amino, carboxyl, and hydroxyl groups [Maeda 1989]. Leeder et al. [Leeder 1965] confirmed polar amino groups' absorption is dominant, reaching nearly the theoretical 3 water molecules per amino group at 80%RH. Above 80%RH, there is structural swelling. The result is a weakening of the inter-molecular bonding strength and formation of a water network in the keratin matrix, mostly surrounding the globular proteins [Feughelman 1997]. The weakened inter-molecular bonding allows the keratin molecules to slide pass each other at a lower threshold stress.

Rhinoceros horn is made of an interwoven network of fibers [Fraser 1972] which increase the strength and toughen the horn in multiple axes. This is an example of form following function as the rhinoceros horn is loaded in multiple directions during use. Other biological applications of keratin have different arrangements of the fibrils adapted to the application. For example, in hair and feather rachis, the filaments are arranged parallel to the direction of growth, increasing axial strength, while in fingernails the filaments are normal to the surface, enhancing wear-tolerance. Clearly the structure of keratin has adapted to the environment and use of the animal.

Ostrich keratin has been demonstrated to be influenced by moisture content, in both compression and tension, the modulus decreases with the increase of moisture. This was true for both feather rachis and claw keratin. The results were quite substantial; a reduction in elastic modulus from 3.66GPa at 0%RH to 1.47GPa at 100%RH was observed [Bonser 2002]. A large decrease in the tensile stress at failure was also observed, with a decrease from 221MPa to 106MPa at 0%RH and 100%RH, respectively. Along with the reduction in ultimate tensile strength and elastic modulus with increasing moisture there was an increase in the strain at failure of approximately 3-fold, from 5.71% to 20.51%.

Table 3.1 Mechanical Properties of keratin (various authors)

Material	Modulus	Strain at failure	Stress at failure	Structure
Austrian copperhead (scale) [Fraser 1980] Laysan albatross	Tensile 3.5GPa (65%RH) 0.86GPa (100%RH) Tensile 5.2GPa (65%RH) 3.4GPa (100%RH)	n/a	n/a	α
Goose feather rachis [Cameron 2003] Swan feather rachis Ostrich feather rachis	Tensile 3.2±0.1GPa(0%RH) 4.2±0.3GPa(50%RH) 4.9±0.4GPa(75%RH) 2.7±0.3GPa(0%RH) 3.7±0.2GPa(50%RH) 4.1±0.4GPa(75%RH) 1.7±0.1GPa(0%RH) 1.4±0.1GPa(50%RH) 1.4±0.1GPa(75%RH)	n/a	n/a	α
Oryx horn [Kitchener 1987]	6.1GPa (0% regain*) 4.3 GPa (20% regain) 1.8 GPa (40% regain) Shear	n/a	n/a	α
Ostrich feather rachis 0%RH [Bonser 1995 Taylor 2004]	3.66 GPa Tensile (0%RH) 1.47 GPa Tensile(100%RH)	5.71% (0%RH) 20.51% (100%RH)	221 MPa (0%RH) 106 MPa (100%RH)	β
Ostrich claw [Bonser 2002]	1.6 GPa 'dry' 0.18 GPa 'wet' tensile	n/a	n/a	β
Toco toucan (micro-hardness) [Seki 2005]	1.4 GPa (tensile) 6.1 GPa (Indentation)	N/A	50 MPa	β
Tokay Gecko Seta [Peattie 2007]	1.4-1.6 GPa bending	n/a	n/a	α
Tokay gecko seta [Huber 2008]	1.2 GPa Micro-indention 7.3±1.0 GPa Tensile** 1.7 ±0.6GPa 3pt-bend	2.5%±1.3% Range 1.5% to 4.7% Tensile	149±107 MPa Range 76-336MPa	β
Wool [Maeda 1989, Whitely 1977, Peters and Woods 1955]	1.4 to 5 GPa tensile	20% - 45%	40 MPa - 280 MPa	α
Wool in liquid N_2 [Feughelman 1967]	9.7 GPa Tensile	n/a	n/a	α

*regain - water absorption by weight, **measured in high vacuum due to sample preparation method

Literature values of elastic modulus for keratins range from 0.18GPa to 7.3GPa. However, many mechanical property values were not accompanied by the temperature and humidity in which the material was measured, making direct comparisons uncertain. Without these values there should be skepticism of the data presented for elastic modulus and other mechanical property data, as keratin is greatly affected by both temperature and humidity. Strain rate is another important parameter that can greatly affect the modulus and elongation at failure. However, this parameter is also often neglected in the literature [Feughelman 1997].

The elastic modulus of wool in liquid N_2 (-196°C) at 9.7 GPa is the expected value for hydrogen bonds. The elastic modulus of solid water for reference is 9.6 GPa [Fletcher 1970, Feughelman 1997 page 9]. This demonstrates the critical nature of hydrogen bonding and the influence that water plays in the mechanical properties of keratin.

Kitchener et al. [Kitchener 1987] determined the elastic modulus for both the matrix and fibrils of Oryx horn (α-keratin). The elastic modulus of the fibers stayed constant at 6.1GPa over the range of moisture content measured, dry to wet. In contrast the matrix showed a 6.7-fold decrease in elastic modulus from 6.1 GPa dry to 0.9 GPa wet. This combined to an overall elastic modulus decrease of the Oryx horn from 6.1 GPa dry to 1.8 GPa wet. It is also noted by Kitchener that dry horn is notch sensitive while wet Oryx horn is not notch sensitive. The notch sensitivity in the elastic modulus measurements indicates at low moisture content the matrix is able to fracture and transfer the propagating crack tip the fibrils. At high moisture content the matrix is unable to transfer the propagating crack tip energy to the fibrils most likely due to the low shear modulus of the hydrated matrix and/or weak matrix bonding to the fibrils.

Peattie et al. measured the elastic modulus of gecko setae of between 1.4 GPa and 1.6 GPa depending on the species evaluated [Peattie 2007]. Species dependence of E observed by Peattie is interesting and may indicate adaptation to particular environments. Peattie utilized an Euler-Bernoulli beam vibration model to determine the elastic modulus. Testing was performed by gluing one end of the seta to a secured surface while the free end was glued to a 40μm glass bead. By initiating oscillation of the bead the elastic modus can be determined through mathematical means. However, once plastic deformation occurs the stress-strain relationship is no longer linear and other dampening effects become active. Just the static load of the glass bead represents a strain of nearly 1%, and any additional perturbation of the system would exceed linear stress-strain region. This could explain the lower value of elastic modulus of the seta compared to other measurements for β-keratin by other authors and this study.

Huber et al. observed similar elastic modulus results in bending and nano-indentation as Peattie. Elastic modulus was 1.2GPa for nano-indentation and 1.7 ± 0.6GPa in 3-pt. bending, although avian β-keratin has larger values [Bonser 1995, Bonser 2002, Taylor 2004]. The tensile values for elastic modulus obtained by Huber are higher than other published results for keratins. It is curious there were no changes in elastic modulus relative to humidity for a range of 10-60% RH, as measured by 3pt bending. However, sample preparation was performed under high-vacuum, perhaps explaining the lack of humidity effects [Vincent 1992]. Huber also observed fracture surfaces consistent with brittle fracture, a further implication that the setae were dehydrated.

The dynamic mechanical properties of α-keratin have been investigated in the form of human stratum corneum [Mukherjee 2000], horse hair [Druhala 1974], and wool [Danilatos

1981]. All determined there is a strong correlation between the humidity/water content and the viscoelastic properties. As water is absorbed into the keratin matrix the viscoelastic damping increases, while the complex modulus decrease.

3.3 Setal Structure

The setae are specialized appendages emerging from the epidermal layer of the scales that cover the body [Ruibal and Ernst 1965, Maderson 1964 and 1998, Alibardi 2007 and 2011, Peterson 1983]. The epidermal layer is responsible for resistance to water loss [Lillywhite 2006] and mechanical abrasion [Chuong 2002]. Impermeability of water is largely due to extracellular lipids within the epidermal stratified layers [Landmann 1981 and 1988]. The lipids are arranged as 'mortar' in a brick (corneocytes cells) and mortar structure [Landmann 1981 and 1988]. The setae emerging from this layer has an intact plasma membrane up to the point that the individual keratin bundles separate approximately 10-15μm from the termination point with lipid content filling the space between the keratin bundles [Alibardi 2011].

Adhesive setae in lizards have been investigated [Stork 1983, Ruibal and Ernst 1965, Rizzo 2005, Maderson 1964, Autumn 2002, Alibardi 2011]. Each setae of the Tokay is composed of numerous elements of approximately 180 nm to 280 nm in diameter in a columnar arrangement as can be seen in figures 3.3 and 3.4. The elements extend from the base setae, branch into smaller fiber bundles until individual fibrils are isolated and terminate at the spatula. The elements are bundled in the seta that is approximately 3.5-4.5μm in diameter and lengths up to 120 μm for Tokay gecko. The uniaxial fibrils in the seta should greatly increase the longitudinal strength and the transverse strength of the material is greatly inferior. This likely has no adverse affects on the gecko as the loading on the seta for locomotion is mostly along the long axis of the seta. The axial arraignments of the fibers are possibly even advantageous for adhesion.

Scanning electron microscope (SEM) images were collected at the University of Washington (UW) Department of Materials Science and Engineering Electron Microscopy Center using a JSM 7000. Additional high magnification SEM data collection was performed at FEI NanoCenter (FEI NOVA NanoSEM 630) in Hillsboro, Oregon and cross-sectional images were obtained using a focused ion beam (FIB) model V600 at FEI. The NanoSEM 630 is capable of mTorr operation and electron landing energies in the sub kV ranges, allowing better surface characterization and imaging of biological specimens. The FIB was used to cross-section preparation and imaging. Finally, lower magnification images were obtained using a FEI Phenom desktop SEM at Lewis and Clark College.

The specimens imaged at the UW were broken under tensile loading at room temperature and humidity approximately 21°C and 30% RH. Due to limitations of the SEM and charging at high resolution images were not obtained. However, high resolution images were obtained at FEI on specimens. All SEM samples were mounted using conductive carbon tape, samples imaged at the University of Washington and Lewis and Clark College were coated with Au/Pd, and samples imaged at FEI were coated with Ir. Iridium coating allows for better detail and higher resolution than Au/Pd coating. There was no fixation or stain used; all setae were imaged as collected from the animal.

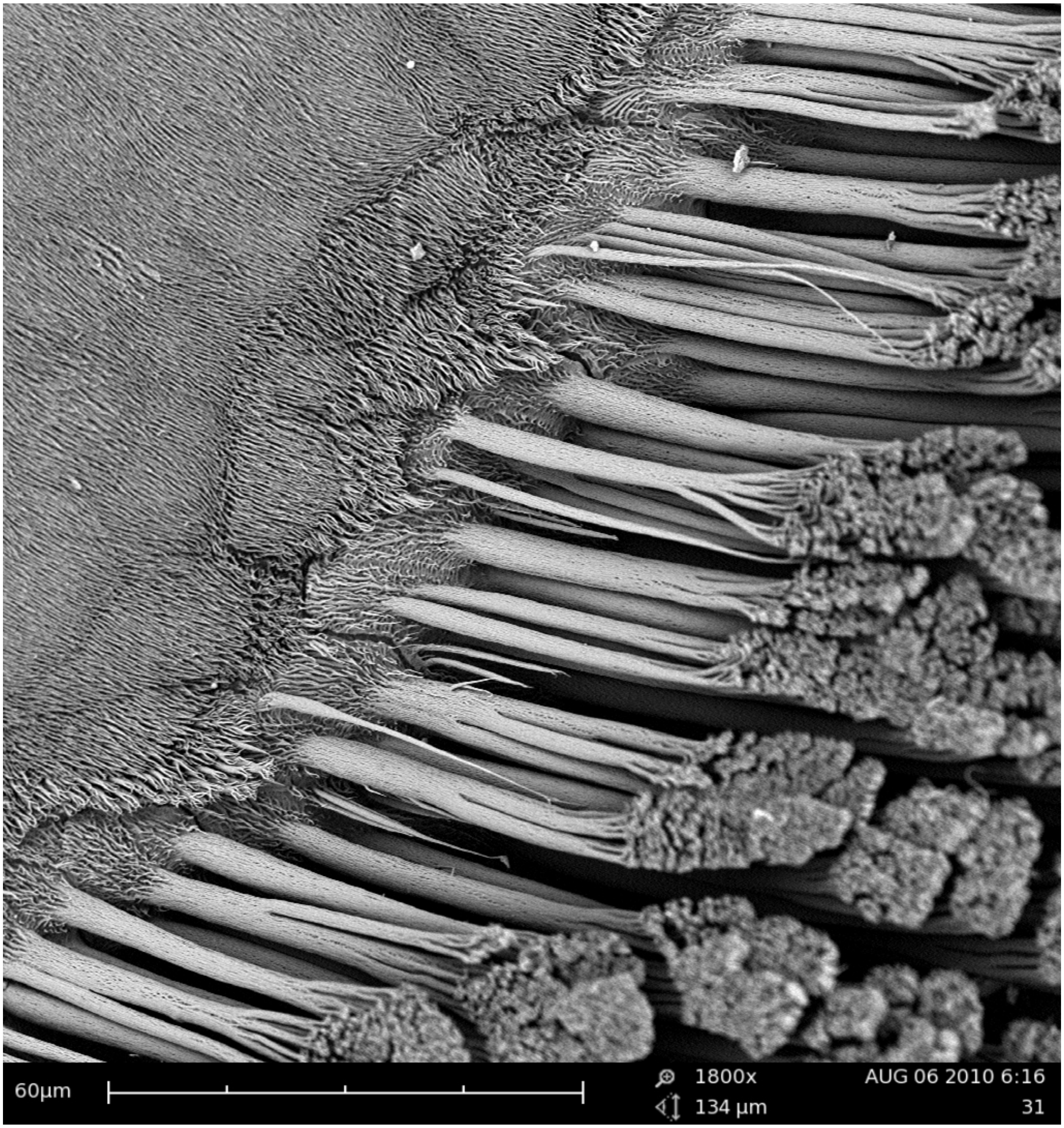

Figure 3.3. Setal forest rising from the smooth lamellar epidermal layer. Setae are densely packed, numbering ~14 400 setae per mm^2. FEI Phenom SEM, at Lewis and Clark College.

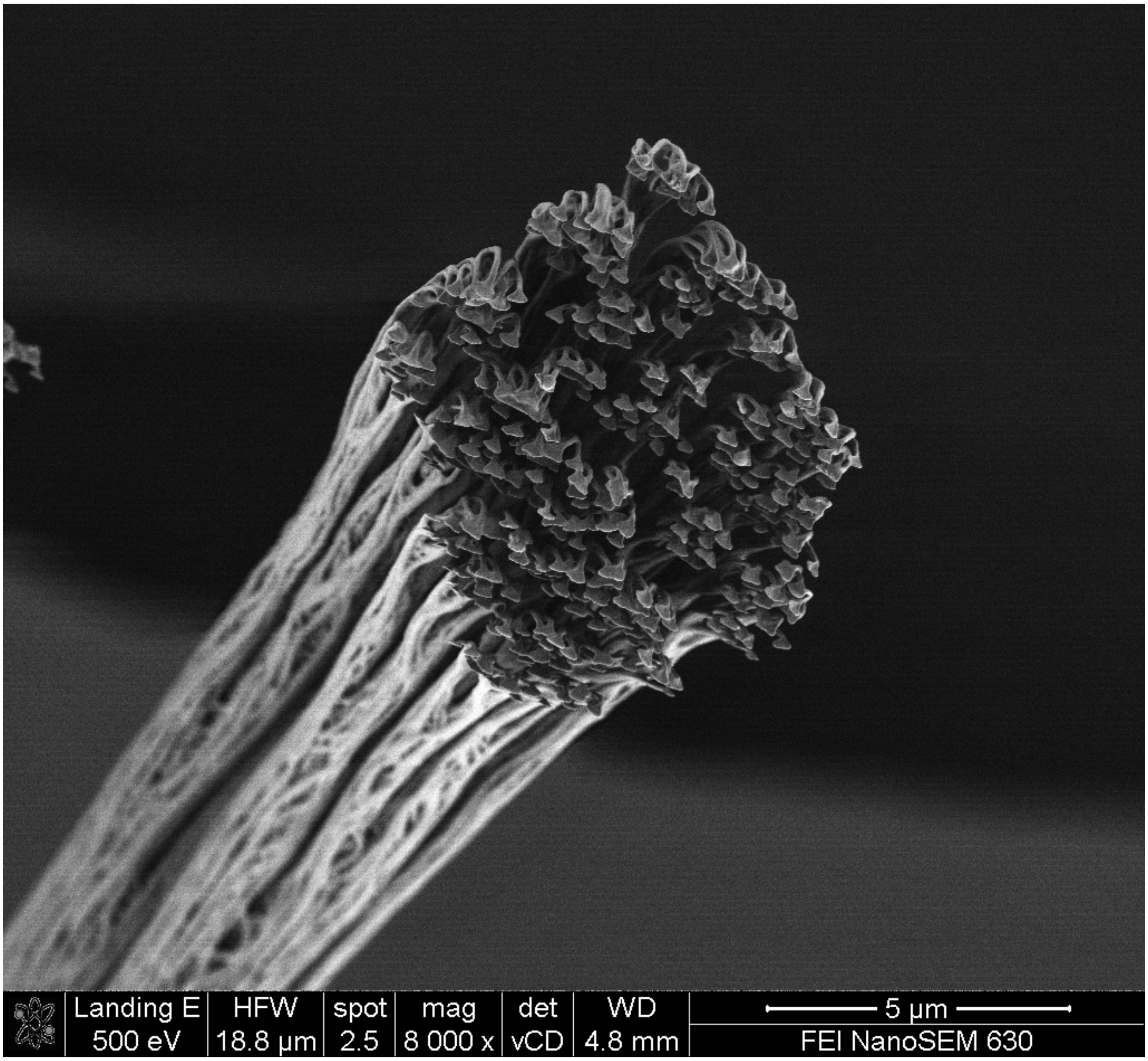

Figure 3.4. Spatula termination of an isolated seta. The spatula number between 300 and 350, consistent with an average fibril size of ~200nm. FEI NOVA NanoSEM 630.

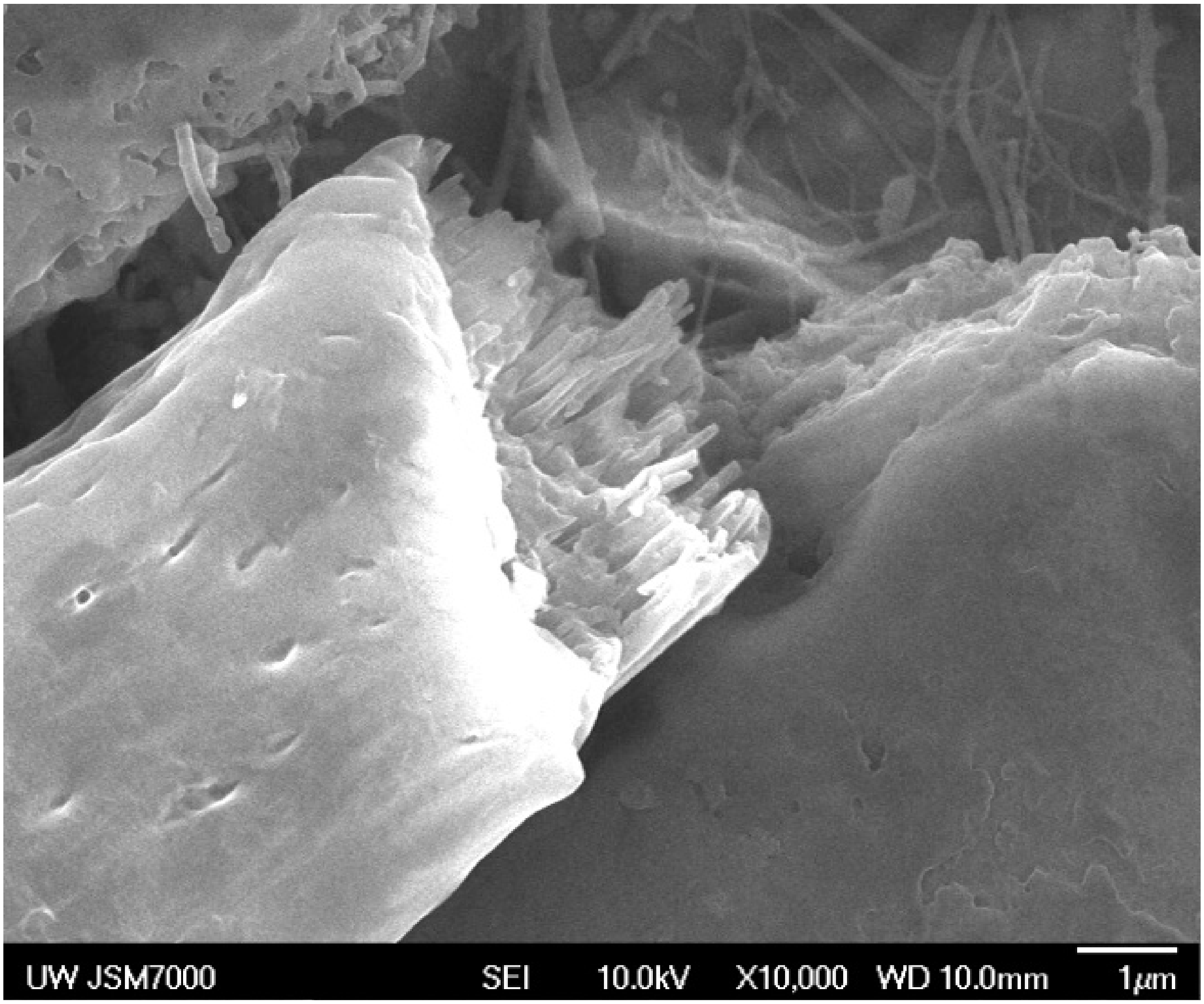

Figure 3.5 Electro-micrograph of a fractured seta at 30RH% and RT under tensile load. Individual filaments in the seta a visible with differing fracture points and fiber 'pull-out'. A sheath is also present in the image. University of Washington department of Materials Science and Engineering electron microscope center. JEOL 7000 SEM, 10kV.

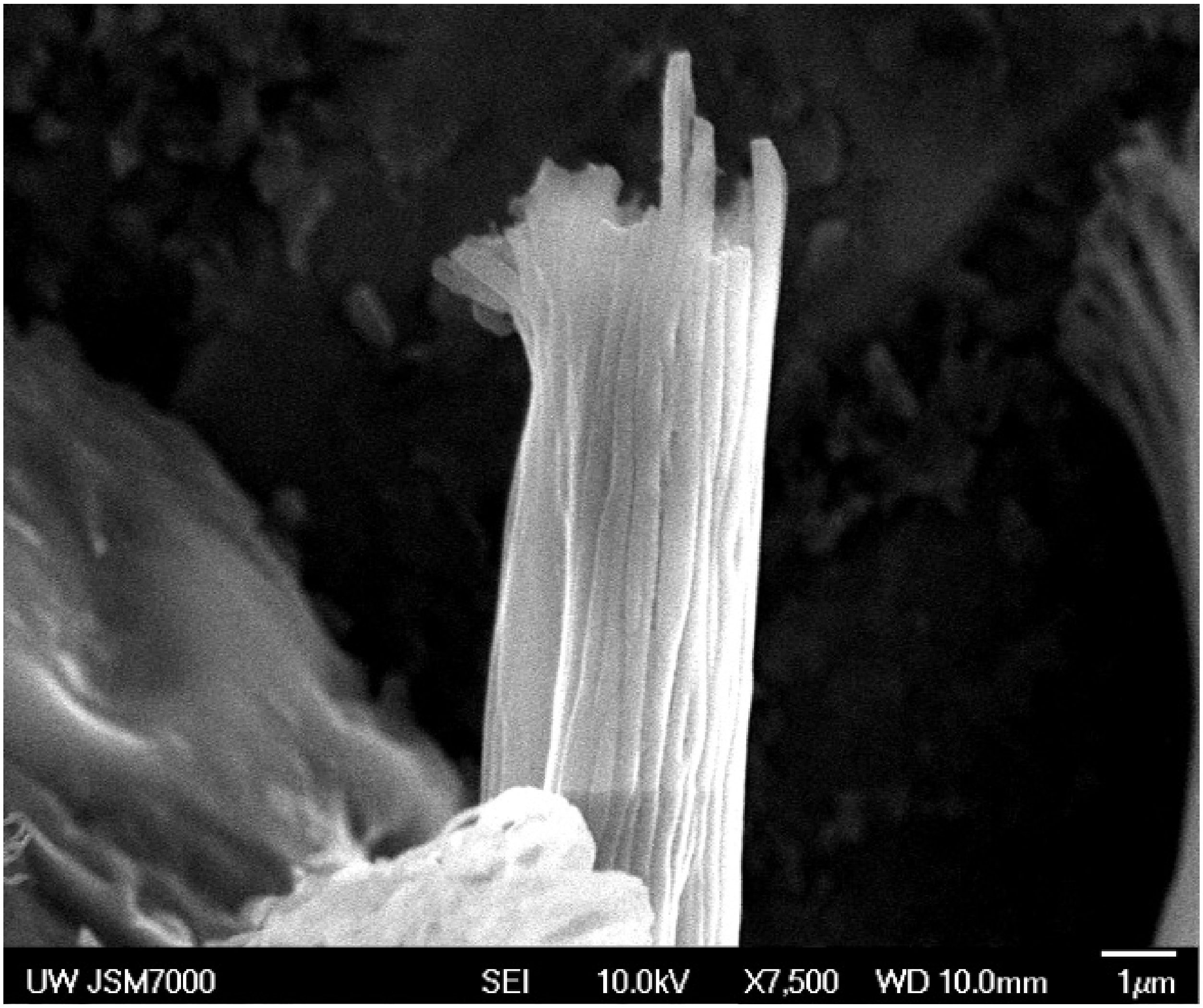

Figure 3.6 Electro-micrograph of a fractured seta at 30RH% and RT under tensile load. Individual filaments in the seta a visible with differing fracture points. University of Washington department of Materials Science and Engineering electron microscope center. JEOL 7000 SEM, 10kV.

Rupture under tensile loading shows the nature of the setae to be composed of keratin bundles. *See figures* 3.5 and 3.6. The fracture surface lends credence to the presence of extended aligned elements in the setae running axially with weaker interfacial adherence between the elements. Failure first occurs along the interfaces between the fibril elements and the matrix, as the matrix is too weak to transfer the propagating crack tip to the fibrils, followed by the failure of the elements under the applied stress. This results in fiber pull out and is typical of weak matrix/strong fiber composites [Hull 1996 pg 145].

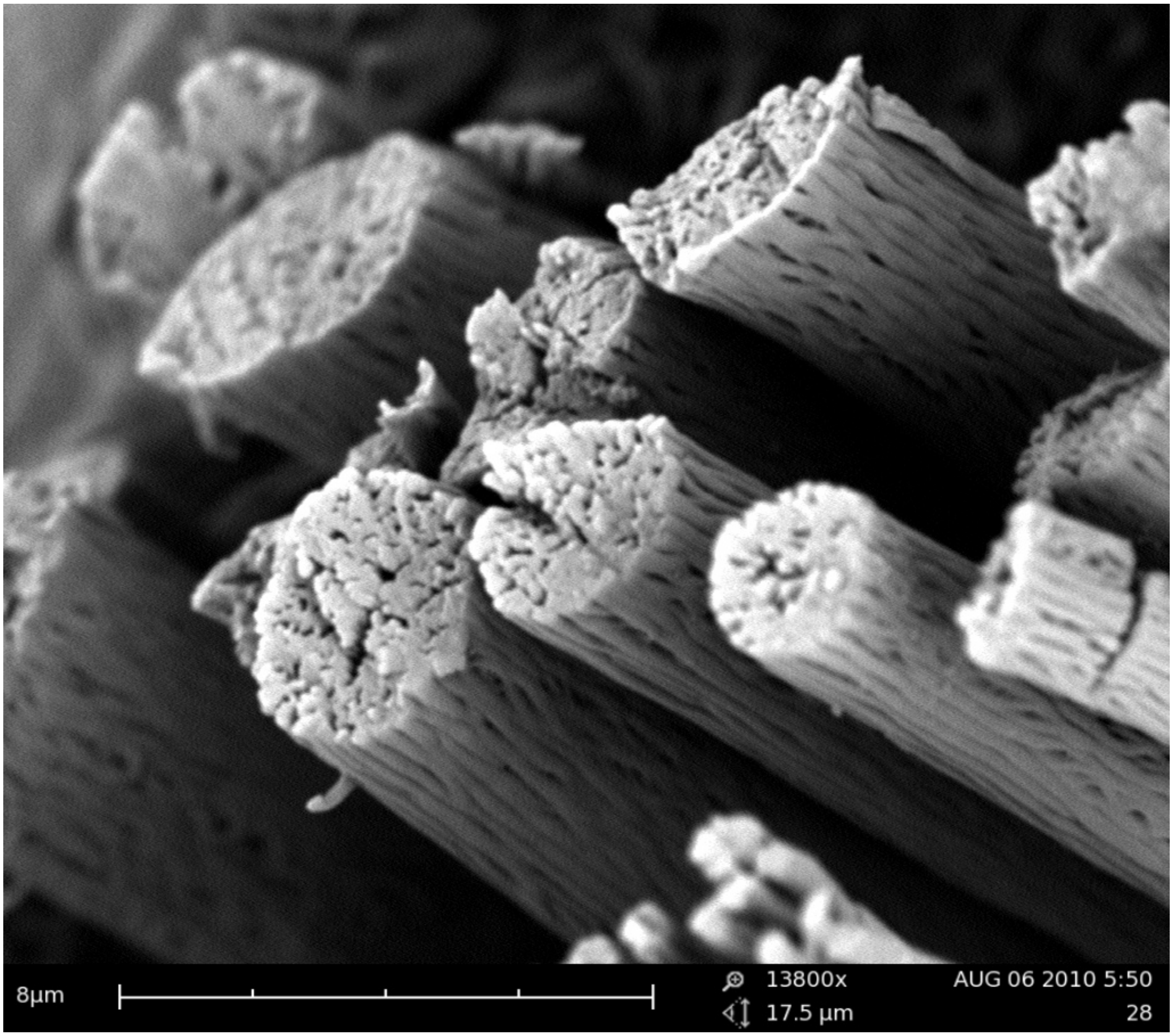

Figure 3.7. Razor blade cut setae. Individual fibrils are visible on the cut surface of the setae with delamination between the fibrils indicating weak bonding among the fibrils in the setae. Lewis and Clark College, FEI Phenom SEM.

Severed surfaces, *figure* 3.7, show the internal structure of the setae resembles that of the surface, uniaxially aligned fibrils. Voiding between the fibrils indicates weak inter-fibril bonding manifested by the shearing action of the cutting process.

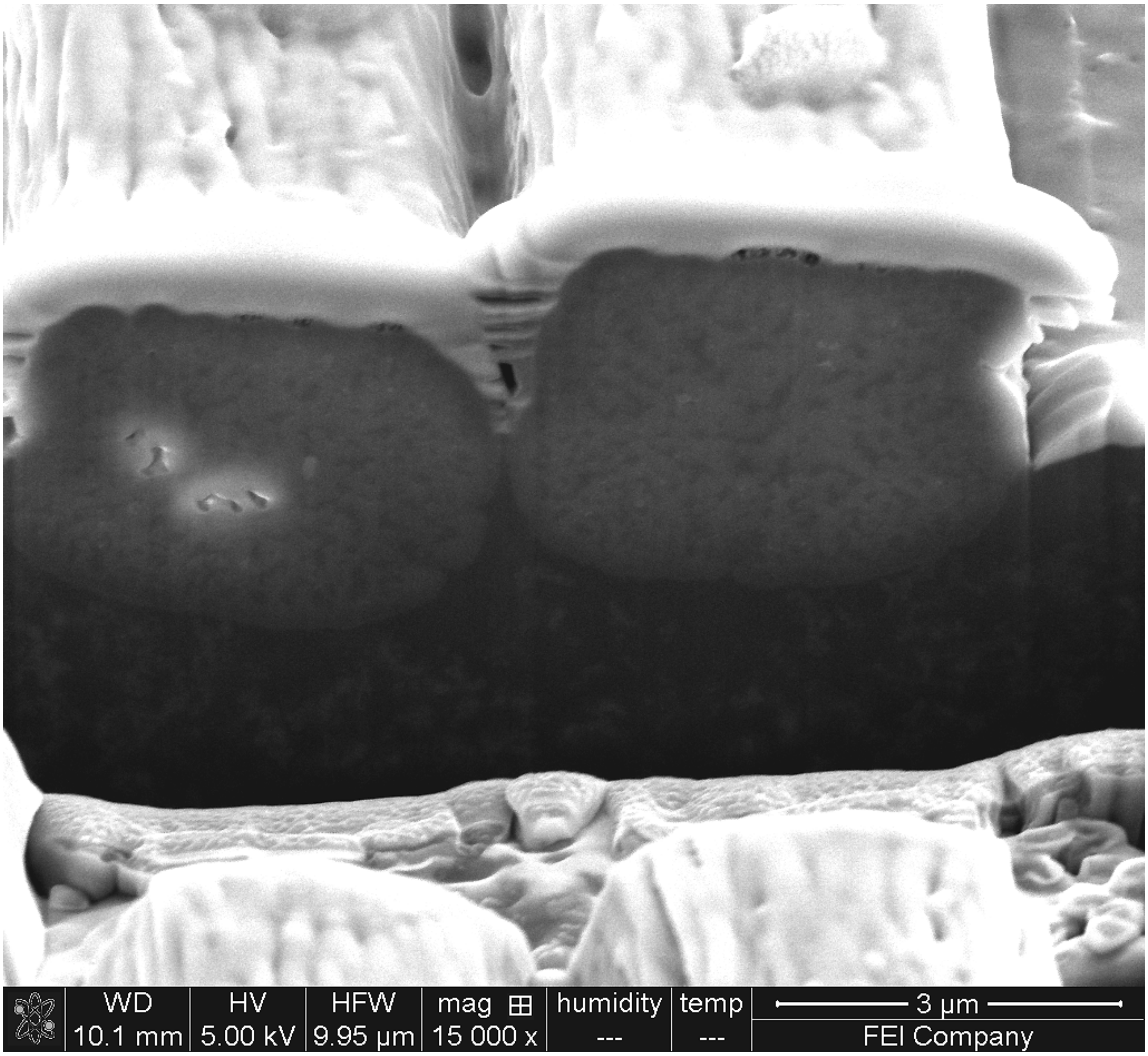

Figure 3.8. Ion milled cross section. Several voids are present near the center of the seta on the left hand side of the image. The voids extended for several micros. FEI FIB

Several voids can be seen on the left-hand seta in figure 3.8. The voids extended for several microns along the axis of the seta as viewed during ion-milling. Although the milled length (~10µm) and number of setae were limit to two, voiding does not appear to be prevalent in the interior of the setae. The interior of the seta is similar as that observed by Rizzo [Rizzo 2005] and Alibardi [Alibardi 2011] with non-symmetric light and dark regions.

The lower volume fraction material composes approximately 22% of the total setal volume as determine by cross-sectional area and Rizzo implies this light region 'electron poor' is matrix. A more detailed study [Alibardi 2011] determined the light regions are keratin bundles surrounded by area with lipid content and a thin plasma membrane on the outer surface of the setae. From figure 3.7, the inter-fibril regions are weakly bonded with individual fibrils separating when sheared. The lipid matrix will be quite weak compared to the fibrils, lipid have elastic storage modulus of ~20kPa and shear modulus of 12 to 30 KPa [Marangoni 2000].

The smooth lamellar epidermal layer, *figure* 3.9, 3.10 and 3.11, fractured under ambient conditions (approximately 20°C and 30%RH or 50%RH) show a very different structure compared to the setae. There are no signs of fibril bundles as in the setae and no fiber pull out. The structure is layered with separation occurring between the layers during rupture, typical of epidermal tissue [Landmann 1988, Lillywhite 1988]. The more ambiguous structure of the lamella, suggests a less optimized strength for uniaxial loads and more isotropic mechanical behavior.

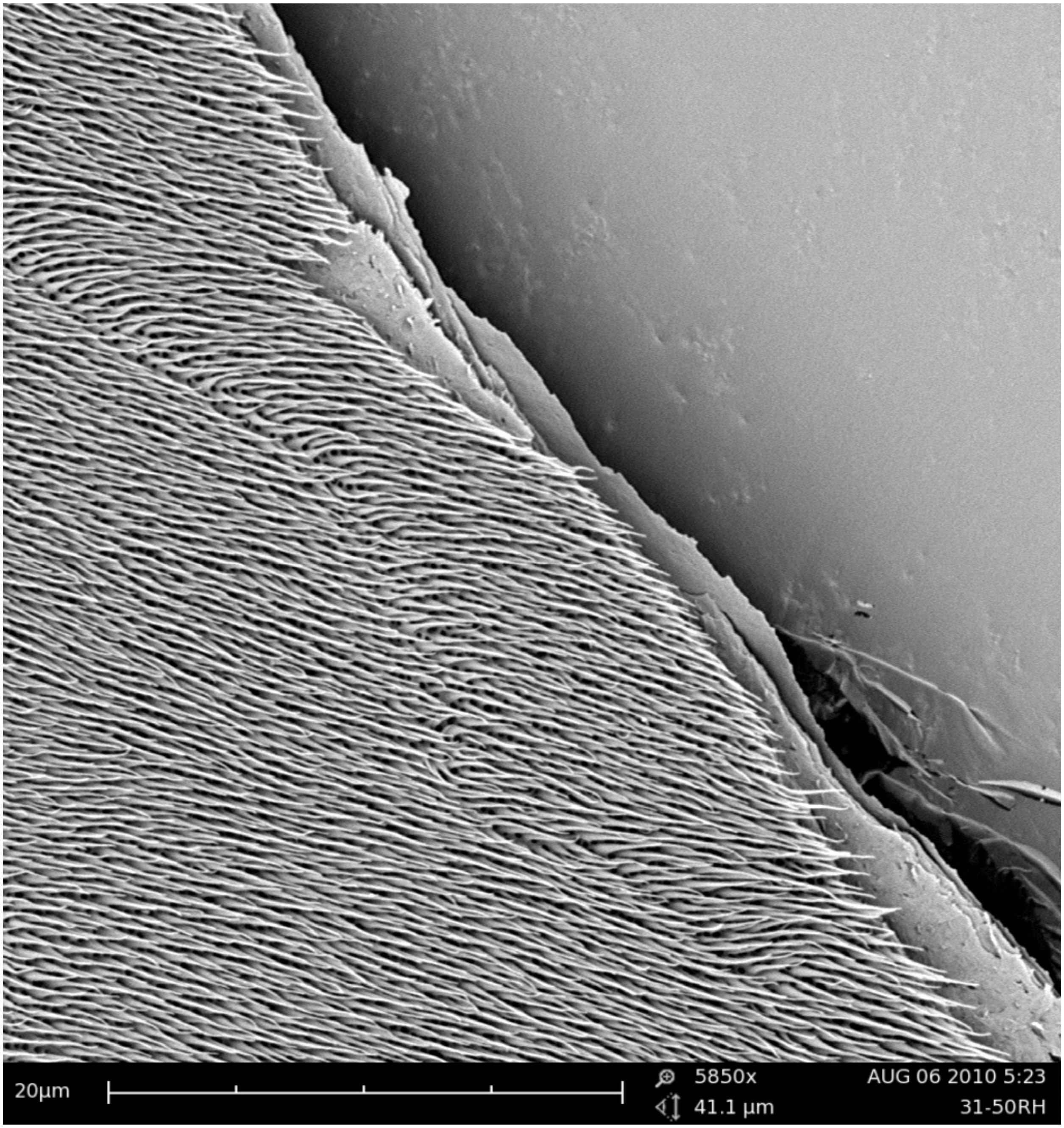

Figure 3.9 Electro-micrograph of the smooth epidermal layer (lamella) shows the structure is not ordered into fibril bundles but is a layered structure. Surface fractured a RT and 50% RH under tensile load. Lewis and Clark College, FEI Phenom SEM.

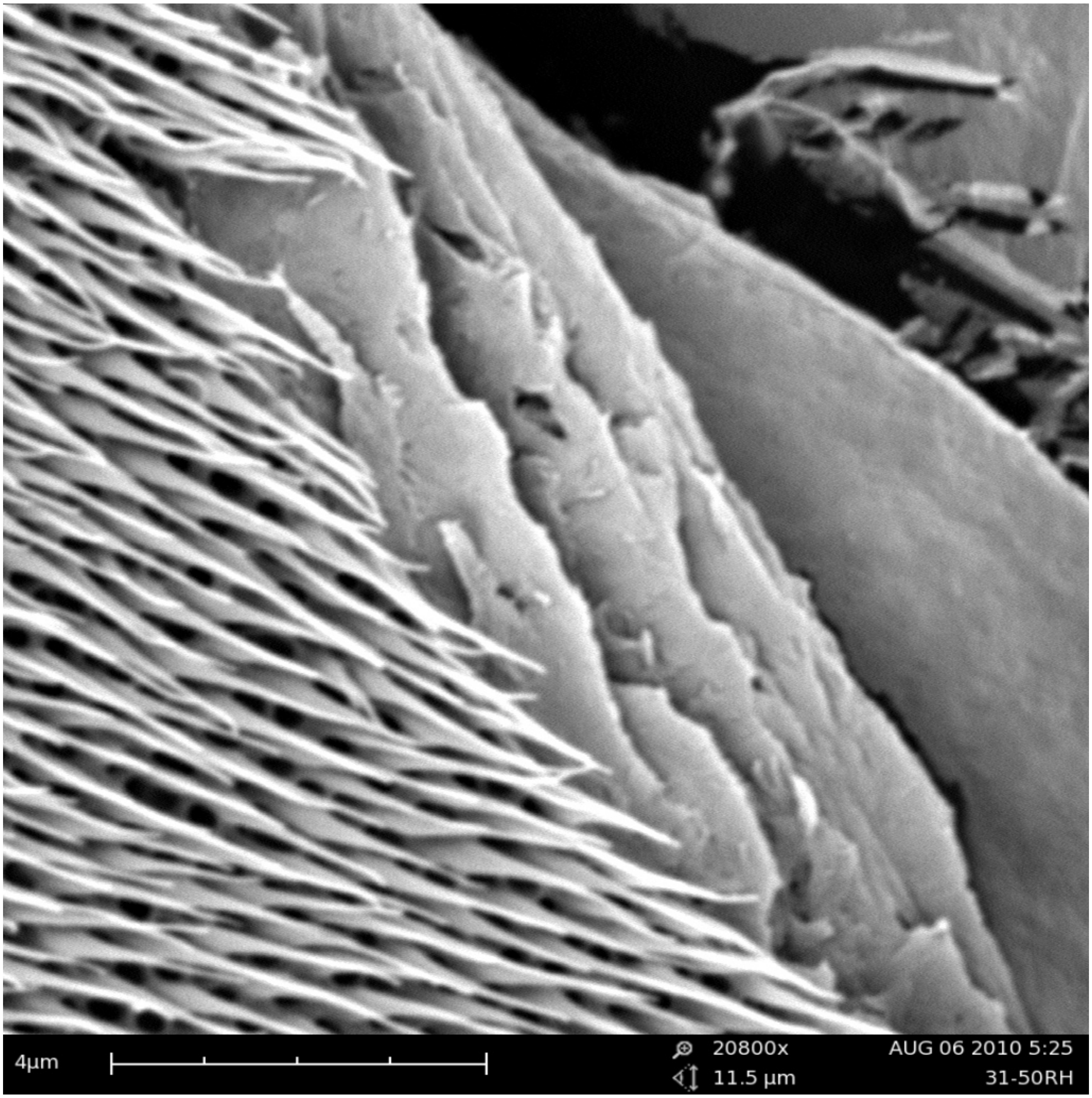

Figure 3.10. High magnification electro-micrograph of the smooth epidermal layer (lamella) shows the structure is composed of stratified layers. Surface fractured a RT and 50% RH under tensile load. Lewis and Clark College, FEI Phenom SEM.

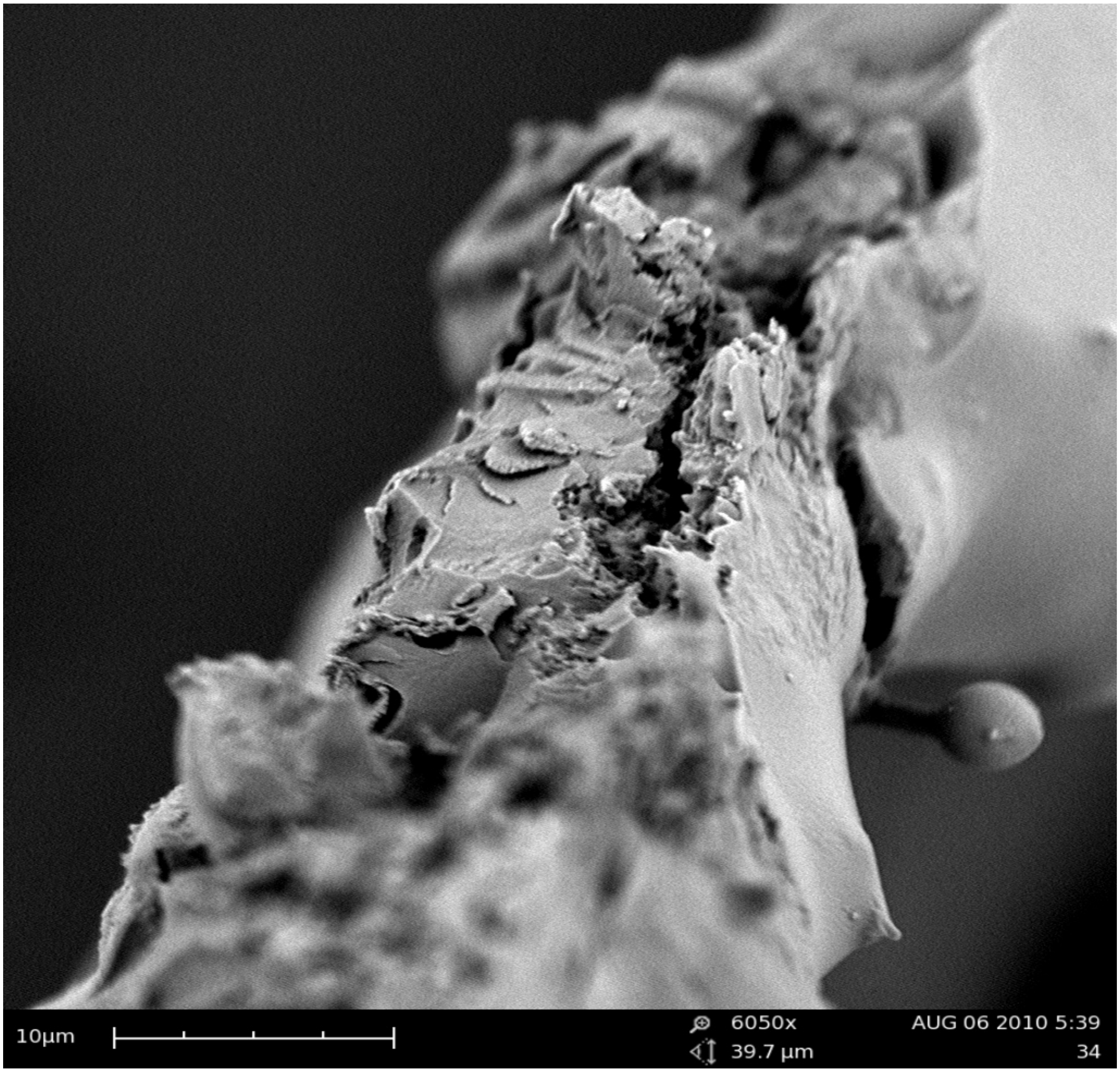

Figure 3.11. Electro-micrograph of the fractured edge of the smooth epidermal layer (lamella). Surface fractured at RT and 50% RH under tensile load. Lewis and Clark College, FEI Phenom SEM.

3.4 Setal Tensile Measurements

Tensile results have been obtained for single setae using RT3 as described in chapter 2. Due to the small force values the raw data has a fair amount of noise. A smoothed curve is overlaid to visually clarify the data.

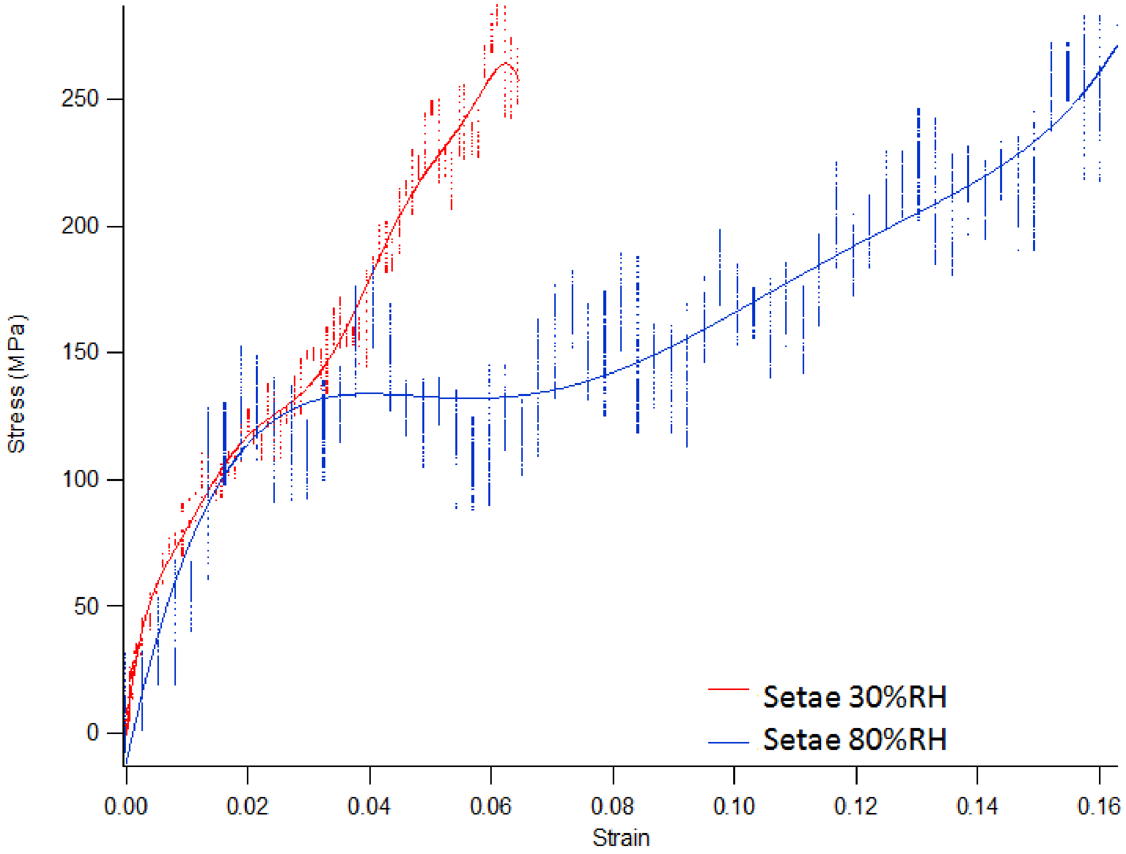

Figure 3.12. Typical tensile Stress-Strain curves for individual setae at 30%RH (red) and 80%RH (blue) with polynomial spline curve added for clarity. There is a modest decrease in the elastic modulus and a significant increase in the strain at failure for the setae measured at 80%RH

At lower humidity levels there are distinct sections of the stress-strain curve. The initial near linear section is followed by a decrease in the slope, then an increase in slope prior to rupture. Setal stalks under tensile loading follow fairly typical behavior for aligned fiber composite materials with 3 distinct slopes on the stress-strain curve prior to complete failure [Hull 1996 pg 145]. That is, there were 3 distinct phases in the stress-strain curve, initial phase where both the matrix and fibers are resisting the applied strain, followed by matrix failure, and the final phase where the fibrils are resisting the applied strain with no matrix contribution.

Table 3.2 Tensile data for individual Seta

Parameter	**Sample %RH**	**N**	**Parameter Value ±std error**
Elastic modulus	30	16	3719.7 ± 202.4 MPa
Elastic modulus	80	3	2138.6 ± 456.5 MPa
strain % at failure	30	16	6.8 % ± 0.59%
strain % at failure	80	3	16.7% ± 2.1%
Stress at failure	30	16	262.5 ± 14 MPa
Stress at failure	80	4	237.2 ± 44.1 MPa

There was a 43% reduction in the measured elastic modulus at 80%RH compared to 30%RH and there is a 2.45 fold increase the elongation at failure at 80%RH. However, the stress at failure does not change proportionally with the increased test humidity. There was an observed reduction of only 10% in stress at failure for the 80%RH samples. It should be noted that the calculation for cross sectional area was not adjusted at higher humidities as the only accurate method for measuring the diameter of the setae was under high vacuum in a SEM, i.e. a dehydrated state.

The initial linear region of the stress-strain curve is Region I; Hookean region. This state continues to ~ 0.5% strain. After the initial linear region the modulus of the S-S curve is greatly diminished and is distinctly non-linear, this is Region II; yield region. For the 80%RH samples, there is gradual decrease in slope from 1% to ~2.5% strain before more rapid slope decrease. The gradual slope roll off for the 30%RH specimen is much shorter ~1% to 1.5% strain, and region II starts at 1.5% strain for the 30%RH specimens versus 2.5% strain the 80%RH specimen group. Region III or post yield region is the area of slope increase following region II. Rupture marks the end of region III.

The stress-strain curves for the setae are similar to those obtained by Peters and Woods [Peters and Woods 1955] for wool, but the setae are much less extendable. Wool is known to have keratin filaments aligned parallel to the axis of the fiber [Fraser 1971, Feughleman 1997, Whitely 1977, Caldwell 2005].

3.4.1 Stress-Strain Model

Feughelman [Feughelman 1997, page 125] presented a two phase model to explain the mechanical behavior of wool, even though wool under goes α to β transition during extension; it remains useful basis to explain setal mechanics.

Region I is characterized by both the matrix and fibrils under strain contributing the stiffness.

Transition region I to region II: the linear stress-strain relation disappears indicating the matrix is beginning to fail and more strain is transferred to the fibrils.

Region II is characterized by the complete failure of the matrix to transfer strain to the fibrils.

Transition region II to region III: The fibrils begin to extend, the fibril matrix begins to fail transferring the strain to the keratin microfibers.

Region III: the microfibers internal to the fibril bundles extension of the helical regions becomes impeded by steric interaction, the matrix proteins are unfold as a result of longitudinal stress and jamming between the microfibrils. Water molecules continue to facilitate the breaking and reforming of bonds. The microfibers begin to the fail near the end of region III leading to complete rupture

In region II and III the effects of water reduces the S-S slope appreciably and extends the transitional periods.

Table 3.3 Regional slopes of individual setae under tensile strain at 30% and 80%RH.

	Seta	
Region I	**Modulus ± std error**	**% Strain of onset ± std error**
30%	3719.7 ± 202.4 MPa	N/A
80%	2138.6 ± 456.5 MPa	N/A
Region II		
30%	2101.2 ± 115.5MPa	1.0% ± 0.2%
80%	367.2 ± 128.4 MPa	3.2% ± 0.4%
Region III		
30%	3407.6 ± 209.1Mpa	2.4% ± 0.3%
80%	1130 ± 192.9MPa	7.5% ± 1.2%

3.5 Lamellae Tensile Measurements

The forces observed during tensile testing of the lamella were much larger than the setae and resulted in far less sensor noise. The stress-strain curves were initially near linear before a decrease in the slope before rupture. The point of the slope change was much lower for the 80%RH sample and the duration of the reduced S-S slope was considerably longer. See figure 3.13. Typical tensile Stress-Strain curves for lamellae at 30%RH and 80%RH. There is a modest decrease in the elastic modulus and a significant increase in the strain at failure for the setae measured at 80%RH.

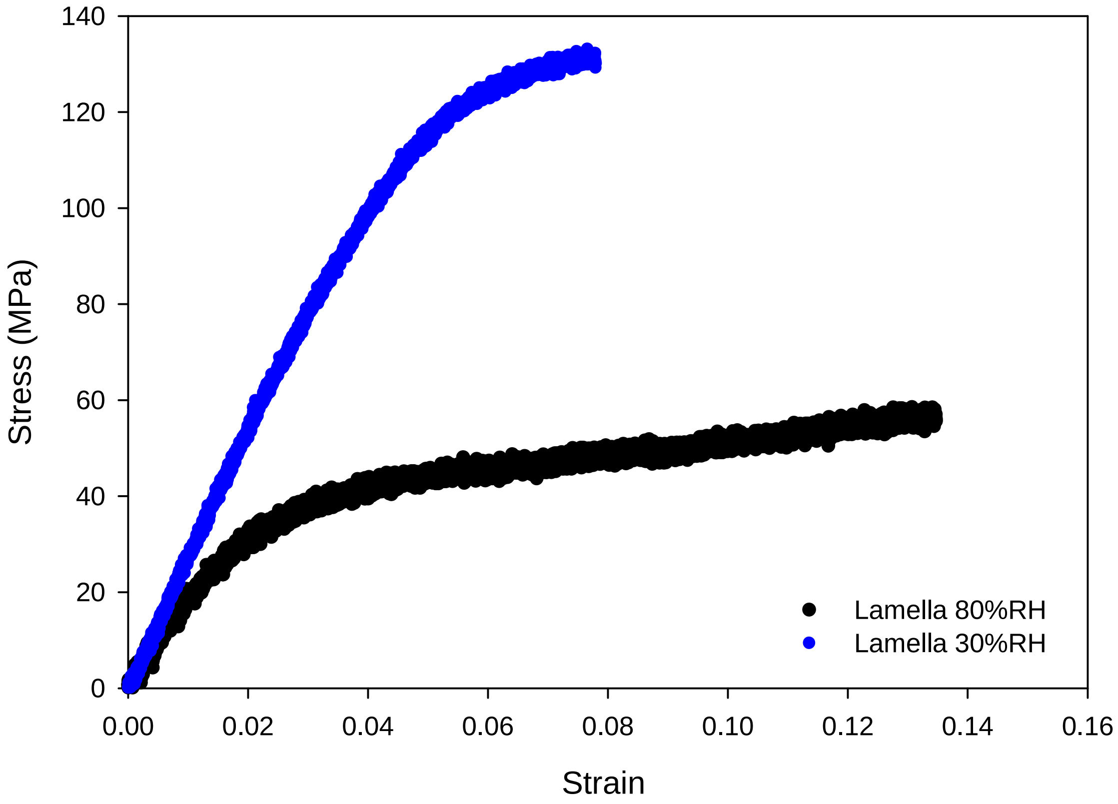

Figure 3.13 Typical tensile Stress-Strain curves for lamella at 30%RH and 80%RH. There is a modest decrease in the elastic modulus and a significant increase in the strain at failure for the setae measured at 80%RH.

Lamella showed similar tensile results as the setae with a strong dependence on humidity. There was a 2x increase of the strain and stress at failure from 30%RH to 80%RH. And the elastic modulus decreased from 3220 MPa to 2270 MPa, a reduction of 29.5%.

Table 3.4 Lamellae - Measured tensile data

Parameter	**Sample %RH**	**N**	**Parameter Value ± std error**
Elastic modulus	30	6	3220 ± 216 MPa
Elastic modulus	80	6	2270 ± 255 MPa
strain % at failure	30	6	6.8 ± 0.15%
strain % at failure	80	6	12.28 ± 4.6%
Stress at failure	30	6	131.15 ± 14.4 MPa
Stress at failure	80	6	59.19 ± 4.64 MPa

Extension of the lamella under tensile loading results in stress-strain curves with fewer features than for the setae. The S-S curves have two main features an initial linear region followed by a yield region of decreased slope prior to rupture. A transition region of gradual decreasing slope between the two regions is present and is similar to that observed for the setae. The onset of region II occurs just under 2% strain at 80%RH and ~5% strain at 30%RH. The stress-strain curve for the lamella displays a 'J' shape that is common among biological materials [Fung 1993] including epidermal tissue [Lanir 1974].

While the elastic modulus and strain at failure are comparable for both the lamella and setae, stress at failure for the lamella is significantly reduced compared to the setae. The lamellian S-S curves with a single yield point do indicate a different structure than the setae.

The likely explanation for the lamella S-S curve is random orientation of the microfibrils, as there was no statistical difference of the elastic modulus due to orientation of the lamella. Likely the lamellae are composed of numerous orientations, and a multi-cellular structure.

3.6 DMA Testing and Data

In dynamic mechanical analysis (DMA), a specimen is subjected to sinusoidal strain with amplitude $\square_0$ and frequency □: $\square(t) = \square_0 \sin(\square t)$. The resulting dynamic stress, $\square(t) = \square_0 \sin(\square t + \square)$ will be phase shifted with respect to the strain by the loss angle □. The dynamic material behavior can be described by the magnitude of the complex modulus E*

$$|E^*| = \sqrt{(E')^2 + (E'')^2} = \frac{\sigma_o}{\epsilon_o} \qquad \text{Eqn. 1}$$

Where E' and E" is the elastic and inelastic part, respectively, and are related by the dimensionless loss tangent.

$$\tan\delta = \frac{E''}{E'} \qquad \text{Eqn. 2}$$

We conducted our tests at three frequencies (□ = 0.5, 5, and 10 Hz), over a range of humidity (RH = 10, 20, 30, 40, 50, 60, 70, and 80%), and due to limitation of the Aerotech stage for sinusoidal movement of 10Hz at amplitudes of < 1.5nm (strain ~2%) required for setae testing, a nominal $\square_0$ = 2% was applied to both the setae and lamella for all DMA testing. While experimental cyclic loading was consistent with foot fall rate of the gecko, there could be higher frequency loading present on the seta and spatula during locomotion of the animal.

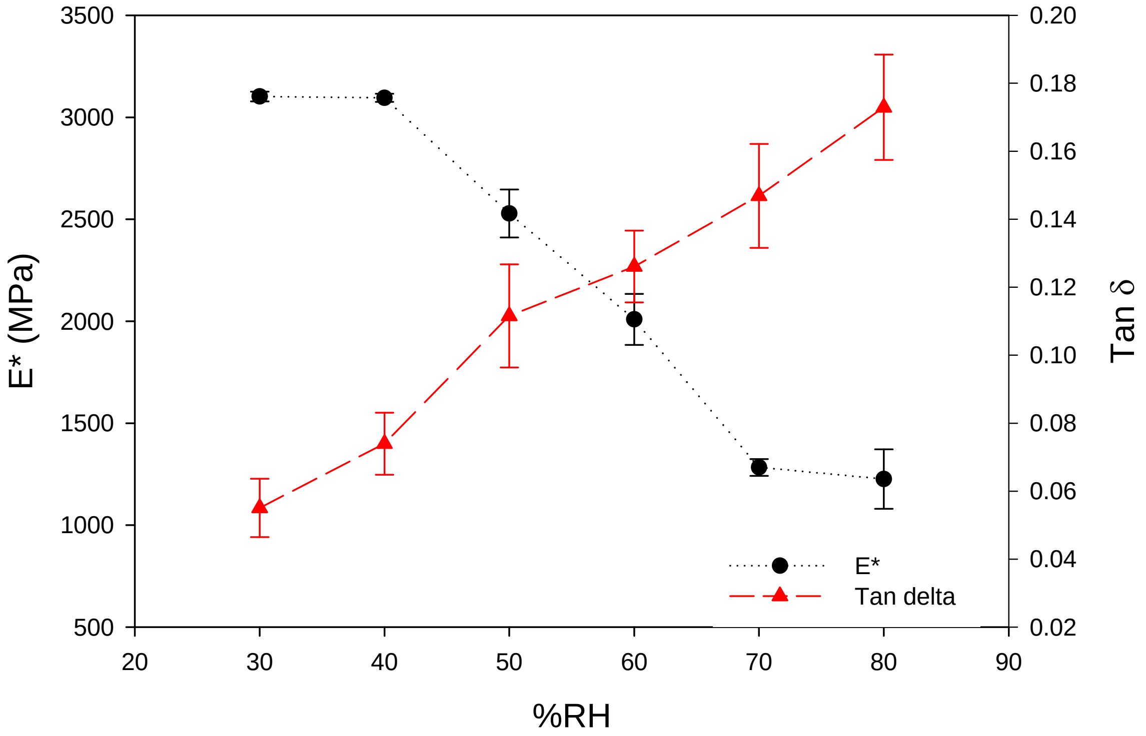

Figure 3.14. Complex modulus and loss tangent of individual seta verses %RH, measured at 5Hz, N=9. Error bars in standard error of mean. The complex modulus E* decreases with RH whilst the loss tangent increases.

Dynamic mechanical measurements of an isolated Tokay seta as revealed in figure 3.14 shows a 3x increase in the loss tangent and a decrease of 1/3 in the dynamic modulus with an increase in humidity. As water is absorbed into the matrix of the seta the water forms an interpenetrating network of hydrogen bonds with the matrix proteins and the amorphous region of the fibril proteins. The water network reduces the energy needed for the proteins to move under an applied stress. This in turn is seen macroscopically as unrecoverable plastic deformation in the dynamic measurements.

While the dynamic modulus for an individual seta at 30%RH was roughly 3 GPa this is lower than that measured under tensile testing, E = 3.2GPa. At 80%RH the disparity is larger, E* = 1.25 GPa compared to tensile of 2.1 GPa. The elastic modulus obtained from tensile testing was less than 1% strain; dynamic measurements were performed using strain of 2% in addition to the different methodology of the two testing procedures. The trends obtained by the two methods both show the decrease in strength with an increase in relative humidity.

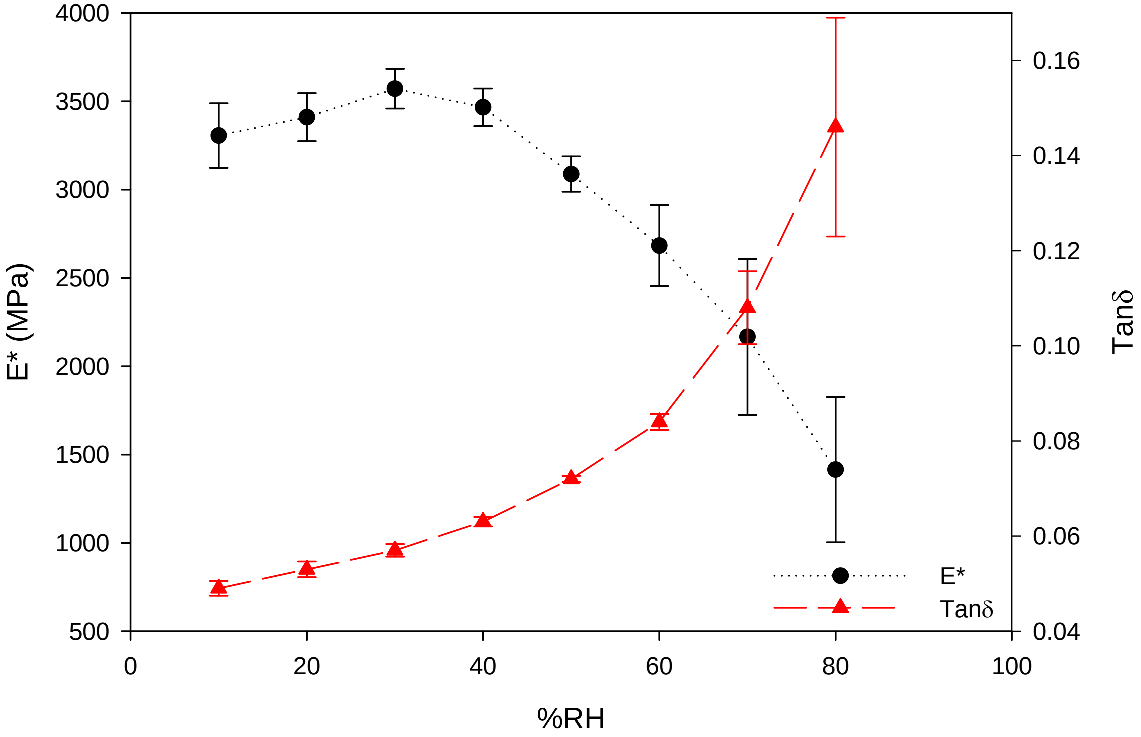

Figure 3.15. Complex modulus and loss tangent of lamella verses %RH, measured at 10Hz, N = 6. Error bars in standard error of measurement. The complex modulus E* decrease with RH whilst the loss tangent increases in good agreement with the setae data.

In addition, DMA was performed on the lamellae of the Tokay gecko. The dynamic modulus and loss tangent for the lamellae is in good agreement with that of the seta. The mechanical response of the lamella was similar to the setae in dynamic loading, E* at 80%RH was ~1/3 the value at dry conditions, a decrease from 3306MPa to 1415MPa and an increase in the loss tangent from 0.049 at 30%RH to 0.146 at 80%RH.

Table 3.5. Dynamic mechanical data for setae and lamella. (std error)

Dynamic Mechanical Property	**Keratin Source**	**30%RH**	**80%RH**
Complex Modulus (GPa)	Seta	3.09(0.024)	1.23(0.145)
	lamella	3.3(0.183)	1.42(0.411)
Loss Tangent	Seta	0.055(8e-3)	0.173(0.0155)
	lamella	0.049(0.0015)	0.146(0.023)

The dynamic mechanical properties of α-keratin have been investigated in the form of human stratum corneum [Mukherjee 2000], horse hair [Druhala 1974], and wool [Danilatos 1981]. All determined there is a strong correlation between the humidity/water content and the viscoelastic properties. In general keratin is becoming more compliant and more lossy with increasing %RH.

3.7 Effective Modulus

The work of adhesion is approximately 50mJm^{-1} for van der Waals interactions [Israelachivili 1992], but as a result of viscoelastic energy loss the work of detachment of pressure sensitive adhesives can be orders of magnitude greater [Creton 1996, Kinloch 1987]. The elastic modulus of the material greatly affects adhesion as the upper limit of Dahlquist's criterion for tacky materials is 100KPa [Dahlquist 1969] at 60 Hz. Autumn et al. [Autumn 2006b] measured the effective modulus of setal arrays to be 80-100KPa. *See figure 3.16.* A reduction in RH causes an increase in elastic modulus of the bulk setal keratin and should have a detrimental effect on adhesion while a smaller elastic modulus will increase adhesion.

While a low E is beneficial for adhesion, too low a modulus may promote matting of the setae [Setti 2003], which reduces adhesion. Expanding on this work, suggests an increase in elastic modulus of the bulk setal keratin will have a deteriorating effect on adhesion while a smaller elastic modulus will increase adhesion.

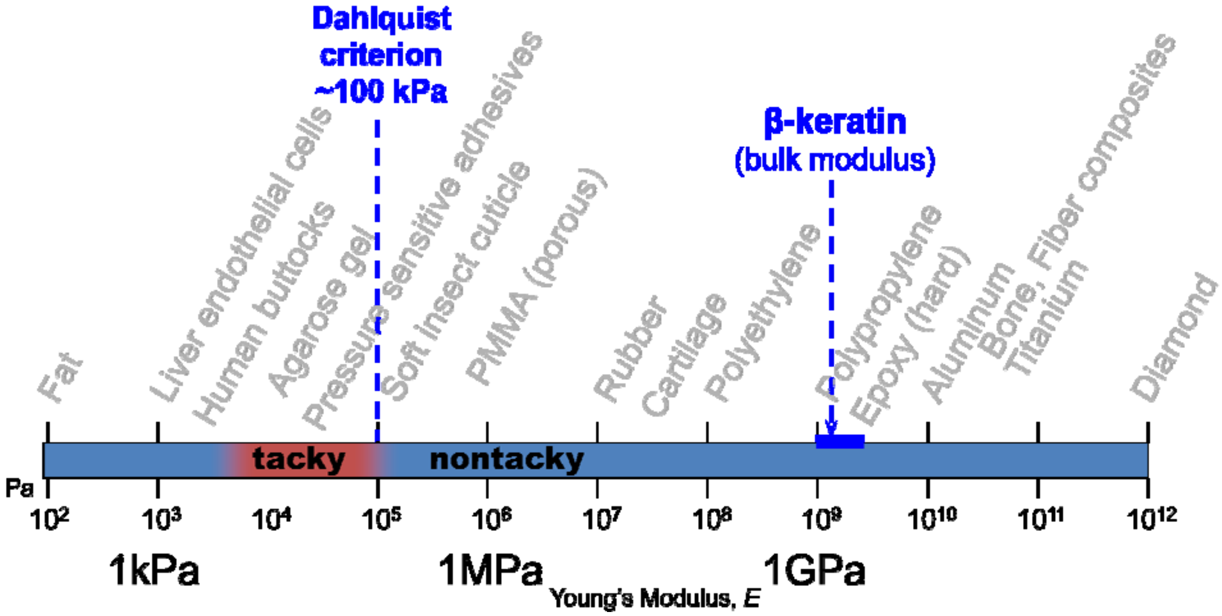

Figure 3.16, Dahlquist criterion as plotted with elastic moduli of assorted materials. For pressure sensitive adhesives, the material needs to be able to conform to the surface while rigid enough to maintain structural integrity. (Figure courtesy of K. Autumn [Autumn 2006])

Changes in elastic modulus of the bulk setal keratin will correlate to changes in the effective modulus and the Dahlquist criteria. Although E for bulk keratin is 4-5 orders of magnitude greater than the upper limit of Dahlquist criteria for tacky materials, one would not expect keratin to act as a pressure sensitive adhesive by deforming easily to molecular contact with a surface of varying profiles. However, since the microstructure of the gecko adhesive is millions of high aspect ratio cantilevers, the effective modulus (E_{eff}) is lower than bulk keratin. One can calculate E_{eff} using Autumn et al. [Autumn 2006b].

The calculations for effective modulus were determined from the following equations.

Area moment of inertia for a cantilever

$$I = \pi \frac{R^4}{4} \qquad \text{Eq. 3}$$

Effective modulus

$$E_{eff} = \frac{3EIDsin\phi}{L^2 cos^2\phi(1 \pm \mu tan\phi)} \qquad \text{Eq. 4}$$

Where: R = setae radius; L = length of setae; E = bulk complex modulus; D = setal density (14 400mm^{-2}); φ = load angle; and μ = coefficient of friction [Autumn 2006b].

The bulk complex modulus of both the lamella and setae are calculated for E_{eff} and plotted in figure 3.17. At 30%RH, E_{eff} is near the upper limit of Dahlquist criteria, while at high RH, E_{eff} decreases to well inside Dahlquist criteria for tacky materials. Figure 3.17 also stipulates geckos have less adhesion at low RH.

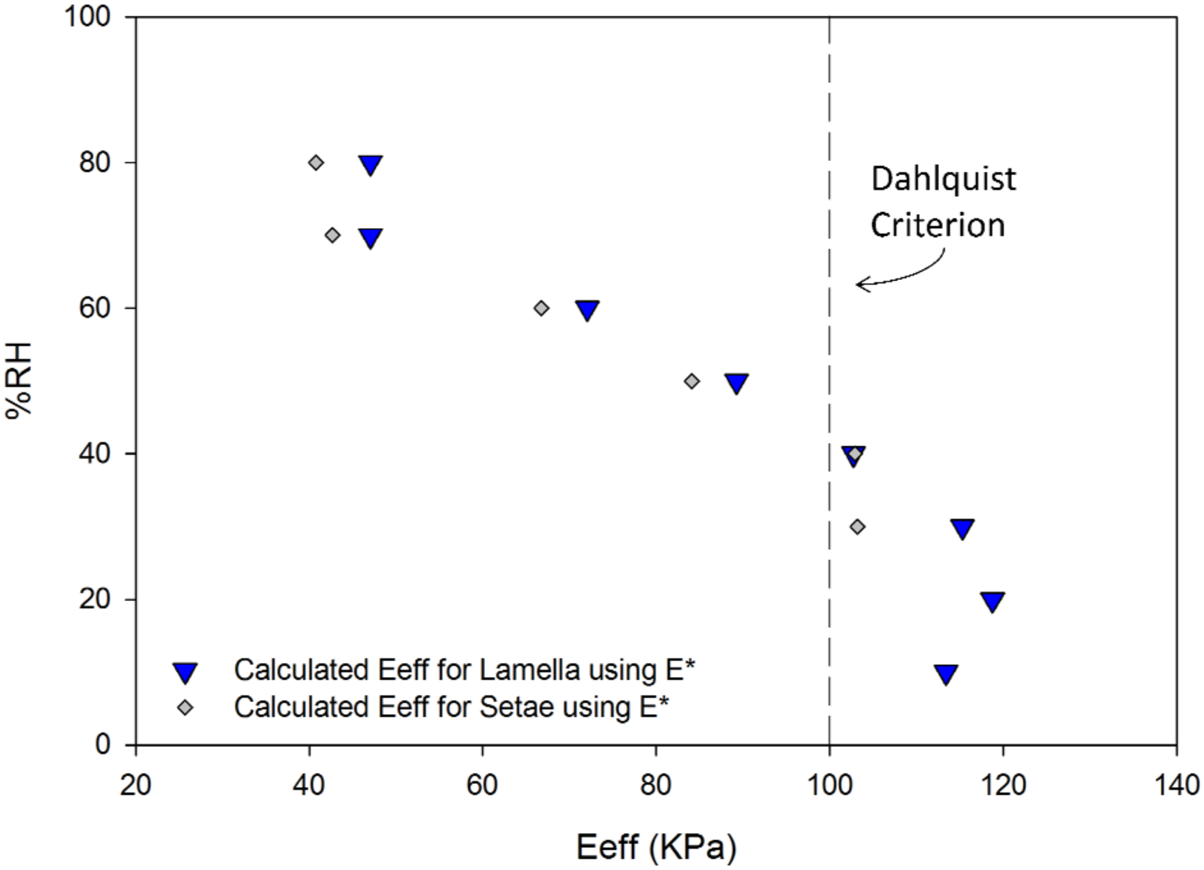

Figure 3.17. Calculated E_{eff} of lamella and setal keratin using E*. Both the setae and lamellae met the Dahlquist criterion for adhesion at approx 40%RH.

There is now plausible explanation that the changes in mechanical properties of the setal keratin are influencing adhesion. That is as the setae become more compliant and softer at higher humidity there is a corresponding increase in adhesion.

3.8 Conclusion

This work has shown a significant influence of RH on the mechanical properties of setal and lamellar keratin, including elasticity, tensile strength, fracture, and dynamic response. The loss tangent increased significantly, by a factor 3x over the humidity range 30 – 80%RH, suggesting that viscoelastic losses increase due to water absorption. In single isolated setae and smooth epidermal layer under dynamic sinusoidal loading, the complex elastic (E^*) modulus at 80%RH is ~1/3 the value at dry conditions. Deformation properties were similar in lamellar samples, with a few exceptions. The changes in mechanical properties of setal keratin were consistent with previously reported studies demonstrating an increase in contact forces, supporting the hypothesis that an increase in RH softens setal keratin and produces a more pronounced viscoelastic response.

Including the geometric effects along with the changes of the elastic modulus, the effective modulus of the setae can be calculated with respect to relative humidity. At modest %RH Dahlquist criteria is met, and correlates well with adhesion data observed in previous studies i.e. more adhesion (tack) at higher humidities.

Structurally the setae are composed of uniaxial bundles within a weak matrix. The lipid based matrix could be remnants of genius or perhaps serve mechanically to increase the compliance of the setae under shear loading. Conceivably, the latter could increase the likelihood of setae attachment to irregular surfaces.

References

Alibardi, L., Edward, D.P., Patil, L., Bouhenni, R., Dhinojwala, A., and Niewiarwski, P.H., Histochemical and ultrastructural analysis of adhesive setae of lizards indicate that they contain lipids in addition to keratins. J. of Morph. 272 (2011) 758-768

Astbury, W. T., and A. Street. X-ray studies of the structure of hair, wool and related fibers. I. General. Trans. Roy. Soc. 230A (1931) 75–101.

Astbury, W. T., and Woods, H. J.. X ray studies of the structure of hair, wool, and related fibers. II. The molecular structure and elastic properties of hair keratin. Phil. Trans. R. Soc. Lond. A. 232 (1933) 333–394

Autumn, K. and Peattie, A., Mechanisms of adhesion in geckos. Int. Comp. Bio. 42 (2002) 1081–1090.

Autumn, K., Majidi, C., Groff, R.E., Dittmore, A., and Fearing, R., Effective elastic modulus of isolated gecko setal arrays. J. Exp. Biol (2006b) 209, 3558-3568

Bendit, E. G. The alpha-beta transformation in keratin. *Nature.* (1957) 179:535

Bendit, E. G. A quantitative x-ray diffraction study of the alpha-beta transformation in wool keratin. Text. Res. J. (1960) 30:547–555.

Bendit, E. G., and M. Feughelman.. Keratin. Encyclopedia of Polymer Science. 8 (1968) 1–44

Bonser, R.H.C., Purslow, **P.P.,** The Young’s Modulus of Feather Keratin, J. Exp. Biol., 198 (1995) 1029-1033.

Bonser, R.H.C., Hydration sensitivity of ostrich claw keratin, J. Mater. Sci. Lett. 21 (2002) 1563-1564.

Cameron, G.T., Wess, T.J. and Bonser, R.H.C., Young's modulus varies with differential orientaion of keratin in feathers. J. Struct. Biol. 2003, 143 (2): pg. 118

Chuong, C.M., Nickoloff, B.J., Elias, P.M., Goldsmith, L.A., Macher, E., Maderson, P.A., Sunberg, J.P., Tagami, H., Pionka, P.M., Thestrup-Pedersen, K., Bernard, B.A., Schoder, J.M., Dotto, P., Chang C.H., Williams, M.L., Feingold, K.R., King, L.E., Kligman, A.M., Rees, J.L., Christophers, E., What is the 'true' function of the skin? Viewpoint 1. Exp. Dermatol. 11 (2002) 159-163

Creton, C., Leibler, L., How does tack depend on contact time and contact pressure? J. Polym. Sci. B. 34 (1996) 545-554.

Dahlquist, C.A., Pressure-sensitive adhesives, in: R. L. Patrick (Eds.), Treatise on Adhesion and Adhesives, Dekker, New York, 1969. pg. 219-260.

Danilatos, G.D., Postle, R., Dynamic Mechanical Properties of Keratin Fibers During Water Adsorption and Desorption. J. of Appl. Poly. Sci. 26 (1981) 193-200

Druhala, M., Feugelman, M., Dynamic Mechanical Loss in Keratin at Low Temperatures. Colloid and Polymer Science. 252 (1974) 381-391

Feughelman, M. The Mechanical Properties of Permanently Set and Cystine Reduced Wool Fibers at Various Relative Humidities and the Structure of Wool. Textile Res. J. 33 (1963) 1013

Feughelman, M., Robinson, M.S., The Tensile Behavior of Wool Fibers in Liquid Nitrogen. J. Text. Res., 37 (1967) 705-706

Feughelman, M. Mechanical Properties and Structure of Alpha-Keratin and Related Fibres; Wool, Human Hair and related Fibres, UNSW Press, USA, 1997.

Fletcher, N.H., The Chemical Physics of Ice. Cambridge University Press, 1970

Fraser, R.D.B., and Macrae, T.P., Hydrogen → Deuterium Exchange Reaction in α-Keratin. J. Chem. Phys. 28 (1958) 1120-1125

Fraser, R.D.B., Macramé, T.P., Rogers, G.E., Keratins; Their Composition, Structure and Biosynthesis. Charles C Thomas Publisher, Springfield, Illinois, 1972.

Fraser, R.D.B., Macrae, T.P., Millward, G.R., Parry, D.A.D., Suzuki, K., and Tulloch, P.A., The Molecular Structure of keratins. J. Applied Poly Symp no.18, 65 1971

Fraser, R.D.B., and Macrae, T.P., Molecular and mechanical structure of keratins, Symp. Soc. Exp. Biol. 34 (1980) 211-246

Fraser, R.D.B., Parry, D.A.D., The Molecular Structure of Reptilian Keratin. International J. of Bio. Macromolecules. 19 (1996) 207-211

Fraser, R.D.B., Parry, D.A.D., Molecular packing in the feather keratin filament. J. Struct. Biol. 162 (2008) 1-13

Fung, Y.C. Biomechanics; Mechanical Properties of Living Tissues. 2nd Ed. Springer-Verlag, New York, New York, 1993. Various chapters

Hansen, W.R., and Autumn, K., Evidence for self-cleaning in gecko setae. Proc. Natl. Acad. Sci. 102 (2005) 385-389

Huber, G., Orso, S., Spolenak, R., Wegst, U.G.K., Enders, S., Gorb, S., Arzt, E., Mechanical Properties of a Single Gecko Seta. Int. J. Mat. Res. 99 (2008) 1113-1118

Hull, D., and Clyne, T.W., An introduction to composite materials. Cambridge University Press. 2nd ed. 1996. Pg. 145

Israelachvili, J., Intermolecular and Surface Forces, Academic Press, New York, 1992.

King, G., Sorption of vapours by keratin and wool, Trans Faraday Soc. 41 (1945) 325-328.

Kinloch, A.J., Adhesion and adhesives: science and technology, Chapman and Hall, New York, NY, 1987

Kitchener, A., Vincent, J.F.V., Composite theory and the effect of water on the stiffness of horn keratin, J. of Mat. Sci. 22 (1987) 1385-1389

Landmann, L., The epidermal permeability barrier. Anat. Embryol 178 (1988) 1-13

Landmann, L., Stolinski, C., Martin, B., The permeability barrier in the epidermis of the Grass snake during the resting stage of the sloughing cycle. Cell Tissue Res. 215 (1981) 369-382.

Lanir, Y., and Fung, Y.C., Two-dimensional mechanical properties of rabbit skin. I. Experimental system. J. Biomech 7(1), 1974, 29-34. II. Experimental results. Ibid., 7 (1974) 171-182

Leeder, J.D., Watt, I.C., The role of Amino Groups in Water Adsorption by Keratin. J. of Phys. Chem. (1965) 3280-3284

Lillywhite, H.B., Water relations of tetrapod integument. J. Exp. Biol. 209 (2006) 202-226.

Lillywhite, H.B., Maderson, P.F.A., The structure and permeability of integument. Am. Zool. 28 (1988) 179-204

Lingham-Soliar, T., Bonser, R.H.C., Wesley-Smith, J., Selective Biodegradation of Keratin Matrix in Feather Rachis Reveals Classic Bioengineering Proc. R. Soc. B. 1980 (2009) 1-8

Maderson, P.F.A., Keratinized epidermal derivatives as an aid to climbing in gekkoid lizards. Nature. 203 (1964) 780-781

Maderson, P.F.A., Drewes, R.C., Baptista, L.F., Price, L.F., Elias, P.M., Ultrastructureal organization of avian stratum corneum lipids as the basis for facultative cutaneous waterproofing. J. Morphol. 227 (1996) 1-13

Maeda, H., Water in Keratin. Biophys J. 56 (1989) 861-868

Marangoni, A., Elasticity of hihg-volume-fraction fractal aggregate networks: A thermodymanic approach. Phys. Rev. B. 62, (2000) 13951-13955

McFarlane, J.S., Tabor, D., Adhesion of solids and the effect of surface films,Proc. R. Soc. Lond. A. 202 (1950) 224-243.

Mitchell, T.W., Feughelman, M., The Torsional Properties of Single Wool Fibers: Part I: Torque-Twist Relationships and Torsional Relaxation in Wet and Dry Fibers. Textile Res. J., 30, (1960) 662-667

Mukherjee, S., Richardson, N., Margosiak, M., Lei, X., Understanding dry skin: a physical basis for the effects of dry environment and surfactant treatment on corneum fracture, Processing of the 5th royal society, unilever Indo-Forum in materials science. Imperial college press, 2000. pg 306-324

Pauling, L., Corey, R.B., Compound Helical Configurations of Polypeptide Chains: Structure of Proteins of the α-Keratin Type. Nature no. 4341, 1953

Peattie, A.M., Majidi, C., Corder, A., Fuller, R.J., Ancestrally High Elastic Modulud of Gecko Setal β-Keratin. J.R. Soc. Interface. 4 (2007) 1071-1076

Peters, L., Woods, H.J., Protein fibers, In The Mechanical Properties of Textile Fibres, R. Meredith, ed. North Holland Publishing Company, Amsterdam, 1955. pg. 151-244

Peterson, J.A., The evolution of the subdigital pad of *Anolis*, 2. Caparisons among the iguanid general related to the anilines and a view from outside the radiation. J. Herpetol 17 (1983) 371-397

Rizzo, N.W., Garner, K.H., Walls, D.J., Keiper-Hrynko, N.M., Ganzke, T.S., Hallahan, D.L., Characterization of the Structure and Composition of Gecko Adhesive Setae. J.R. Soc. Interface, 3 (2005) 441-451

Ruibal, R. and Ernst, V., The structure of the digital setae lizards. J. Morphol. 117 (1965) 271-293

Seki, Y., Schneinder, M.S., Meyers, M.A., Structure and mechanical behavior of a toucan beak, Acta Materialia, 53 (2005) 5281-5296

Setti, M., Fearing, R.S., Synthetic gecko foot-hair mirco/nano-structure as dry adhesives. J. Adhes. Sci. Technol. 17 (2003) 1055-1073.

Speakerman, J.B., The rigidity of wool and its change with adsorption of water vapour, Trans Faraday Soc. 25 (1929) 92.

Stork, N.E., A comparison of the adhesive setae on the feet of lizards and arthropods. J. Nat. Hist. 17 (1983) 829-835

Taylor, A.M., Bonser, R.H.C., Farrent, J.W., The influence of hydration on the tensile and compressive properties of avian keratinous tissue. J. Mater. Sci. 39 (2004) 939-942.

Toni, M., Valle, L.D., Alibardi, L., The epidermis of scales in gecko lizards contains Multiple forms of beta-keratins including basic glicine-proline-serine-rich proteins. J. Proteome Res. 6 (2007) 1792-1805

Vincent, J.F.V., Biomechaincs: Materails: A Practical Approach. Oxford University Press, New York, (1992)

Watchman,J.B., Mechanical Properties of Ceramics, Wiley Interscience, New York, 1996. pg 217

West, G.W., Haley, A.R., Feughelman, M., Physical Properties of Wool Fibers at Various Regains, Tex. Res. J. (1961) 899-904

Whitely, K., Kaplin, I.J., The mesocortex, J. Textile Inst. 68 (1977) 384

Caldwell, J.P., Mastronarde, D.N., Woods, J.L., Bryson, **W.G.,** The three-dimensional arrangement of intermediate filaments in Romney wool cortical cells, J of Struct. Biol. 151 (2005) 298-305

Chapter 4

Adhesion of Geckos

Van der Waals force has been determined to be sufficient to explain adhesion in geckos [Autumn 2002]. However, influence of humidity on the adhesion of geckos has been investigated [Huber 2005, Sun 2005, Niewiaroski 2008, Pesika 2009], multi-scale models by Kim and Bhushan [Kim et. al. 2008], and with multi-physics simulations by Chen [Chen 2010]. These studies have raised questions whether capillary adhesion is an active component to gecko adhesion. With differing supporting evidence none of these studies offers a truly satisfying and compelling argument for capillary adhesion.

4.1 Rate effects and capillary adhesion

Condensing water in thin films has two effects. For wetting liquids in a narrow gap, capillary attraction resulting from the surface tension (γ) of the liquid and the curvature of the meniscus can have substantial adhesion. The second effect of thin film water in surface gaps is viscous resistance. Liquids tend to resist rapid separation, the more rapid the separation rate from a static state, greater the viscous resistance. With larger volumes of water than required for capillary formation, water behaves differently, acting as a lubricant in friction and greatly reducing adhesion.

Condensation of capillaries is a time dependent phenomenon, where nano-scale capillary formation requires ~4.2ms [Szoszkiewicz 2005]. Therefore, sufficiently high shear rates will prevent capillary formation and contributions to adhesion. From equation 1, the drag velocity required to nullify capillary contributions can be determined.

$$\tau = \frac{\lambda}{v} \qquad \text{Eqn. 1}$$

Where τ is contact time, λ is slip length, and υ is velocity. From Gravish et al [Gravish 2010] the setal adhesion follows a 'stick and slip' model with a slip length for the setae of 100nm, setting τ = 4.2ms, the predicted decline in capillary adhesion is at a drag velocity of υ > 23.8μ/s. That is, at sufficiently high drag velocities adhesion will be unaffected by RH, while at drag velocities below the predicted threshold, adhesion will increase with RH.

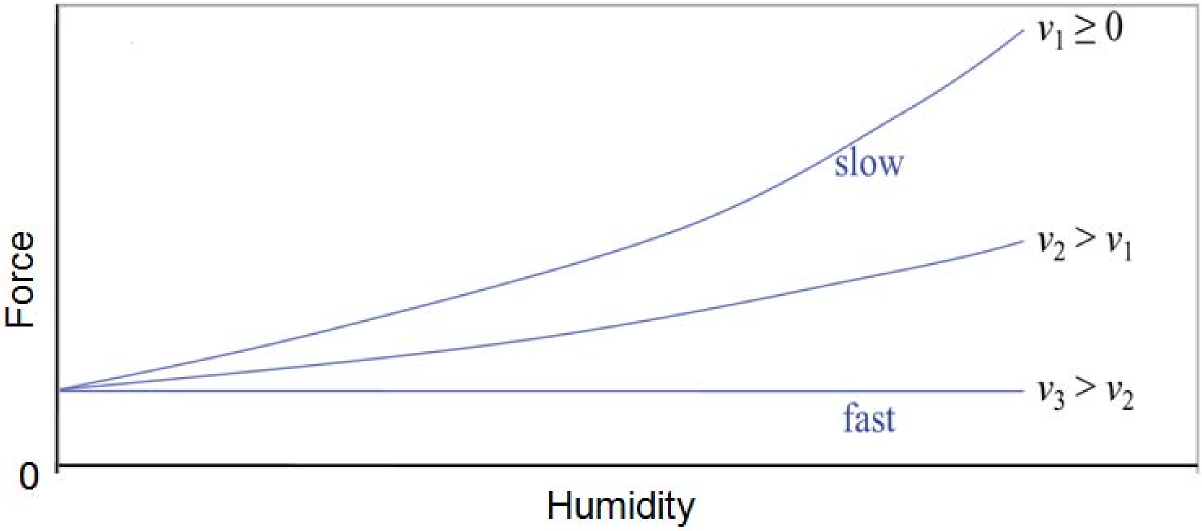

Figure 4.1. The expected velocity effects on capillary adhesion as a function of relative humidity. Where v_1 is lower than the maximum drag velocity for capillary formation and v_3 is above the maximum drag velocity for capillary formation.

The affect of drag velocity on setal adhesion can be broken down into materials properties and capillary adhesion effects forming 4 hypotheses:

Hypothesis 1: adhesion and friction will increase with RH (Humidity effects on contact forces).

Hypothesis 2: RH effects will be greater on hydrophilic substrates and lesser on hydrophobic substrates (Substrate effect on capillary adhesion).

Hypothesis 3: RH effects will be reduced at high rates of shear where capillary bridges have insufficient time to form. (Rate effect on capillary adhesion).

Hypothesis 4: setae will become more compliant and become more tacky at high RH. (Humidity effect on materials properties).

Hypothesis 1-3 are consistent with capillary adhesion mechanism. Hypothesis 4 represents materials property effects on adhesion, an unexplored aspect of biological adhesion.

4.2 Experimental

Setal arrays were collected from live geckos and mounted to a SEM stub using Loctite 4010. Adhesion and friction were conducted using RoboToe on hydrophobic GaAs and hydrophilic glass (SiO_2) substrates at varying humidities from (P/P_s) = 10, 20, 30, 40, 50, 60, 70, and 80% and at five different drag velocities υ = 5, 11, 22, 47, and 100 μm/s. The arrays were allowed to acclimatize for 30 minutes at each humidity set point.

4.3 Results

Adhesion vs. RH (fig 4.2) and friction vs. RH (fig 4.3) obtained from isolated arrays on two different substrates. Figures 4.2 and 4.3, are consistent with hypothesis 1 as both adhesion and friction increase with RH at all velocities. In contradiction with hypothesis 2 (capillary adhesion, substrate effect) the effect of RH did not differ significantly between tests conducted on hydrophobic (GaAs) and hydrophilic (SiO_2) substrates. The data also contradicts hypothesis 3 (capillary adhesion, rate effect). For a slip length of ~100nm [Gravish 2010] a range of velocities of $\upsilon = 5\text{-}100\text{mms}^{-1}$ indicates $\tau = 1\text{-}20\text{ms}$ from eqn. 1. Szoszkiewics and Riedo [Szoszkiewicz 2005] estimated nano-scale capillary formation times from atomic force microscopy measurement to be $\tau_{cap} = 4.2\text{ms}$. Comparing τ_{cap} to the τ range in the experiment we see that the data spans the timescale where we would expect to observe a strong rate effects, exemplified by larger adhesion values at lower test velocities as illustrated in figure 4.1. Data indicates the opposite trend i.e. adhesion is greater at higher drag velocities. At 100µm/s, the velocity is well above the threshold for capillary formation, yet the both adhesion and friction increased with increasing RH with the same trend as the 5µm/s rate. Additionally, the trends hold true using hydrophobic GaAs substrate. This is in contradiction to capillary adhesion theory.

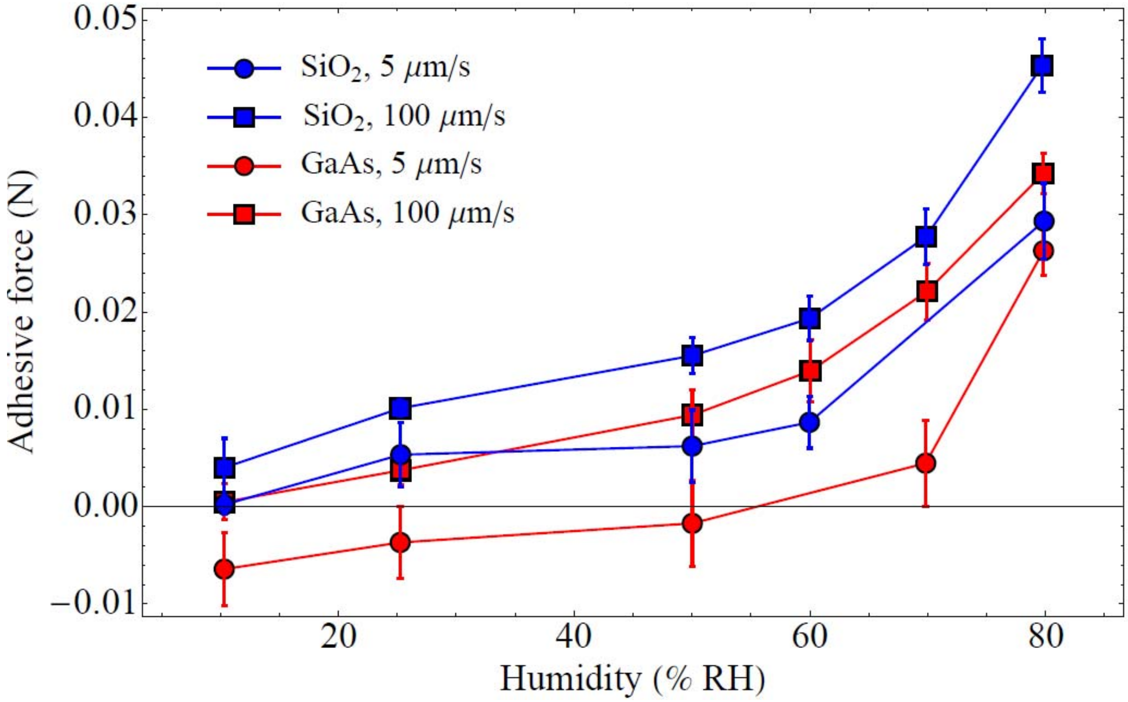

Figure 4.2. Force parallel (adhesion) of a setal array on hydrophilic silica glass (SiO_2- blue)) and hydrophobic GaAs (red), for velocities of 5μm/sec (circle symbols) and 100μm/sec (square symbols).

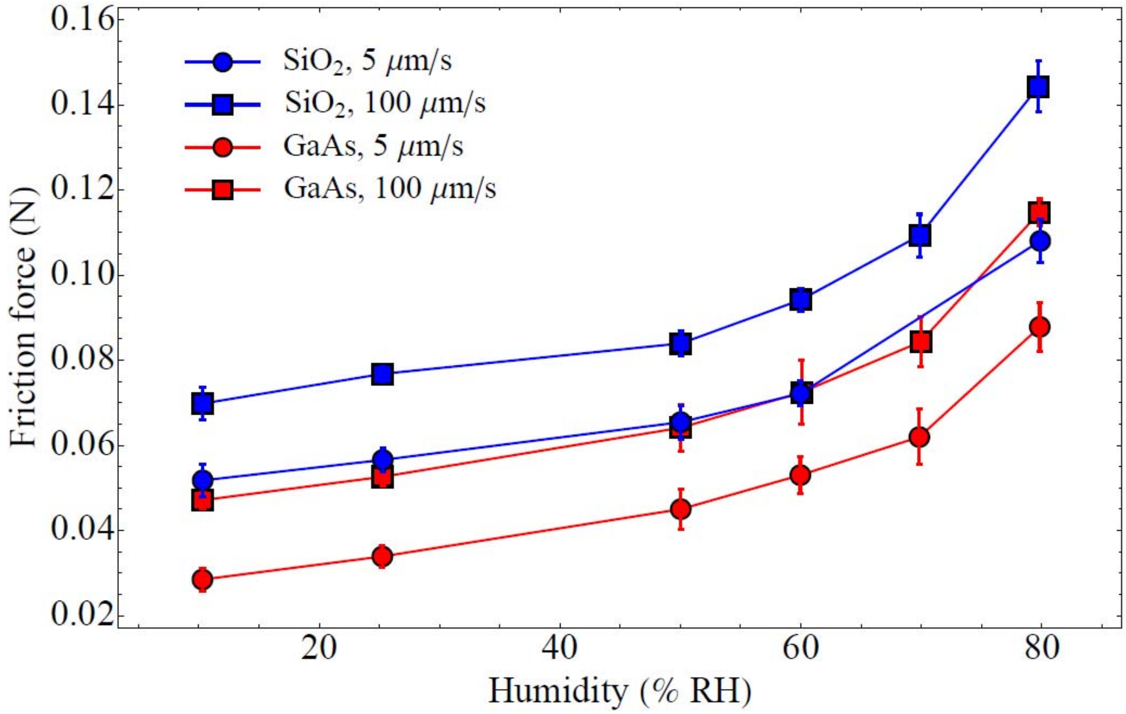

Figure 4.3. Force normal (friction) of a setal array on hydrophilic silica glass (SiO_2- blue) and hydrophobic GaAs (red), for velocities of 5μm/sec (line closest y = 0 line) and 100μm/sec (furthest from y = 0 line).

The results of the DMA experiments on the β-keratin, affect of moisture on the materials properties, typified by the magnitude of the complex modulus $|E^*|$ and the loss tangent. A decrease in the modulus occurred as the humidity increased and the effect was reversed for tanδ, indicating that the storage modulus decreased markedly. This behavior is consistent with a number of previous studies on the deformation of avian keratin [Bonser 2002, Bonser and Purslow 1995, Fraser and MacRae 1980, Taylor 2004] which showed the storage modulus can decrease by as much as 95% at high humidity [Taylor 2004]. A decrease in the storage modulus, E' relative to the loss modulus E" results in a material with a larger time dependent (visco-elastic) component. See figure 4.4. Hence, humidity softened the setal keratin making it more tacky, consistent with hypothesis 4.

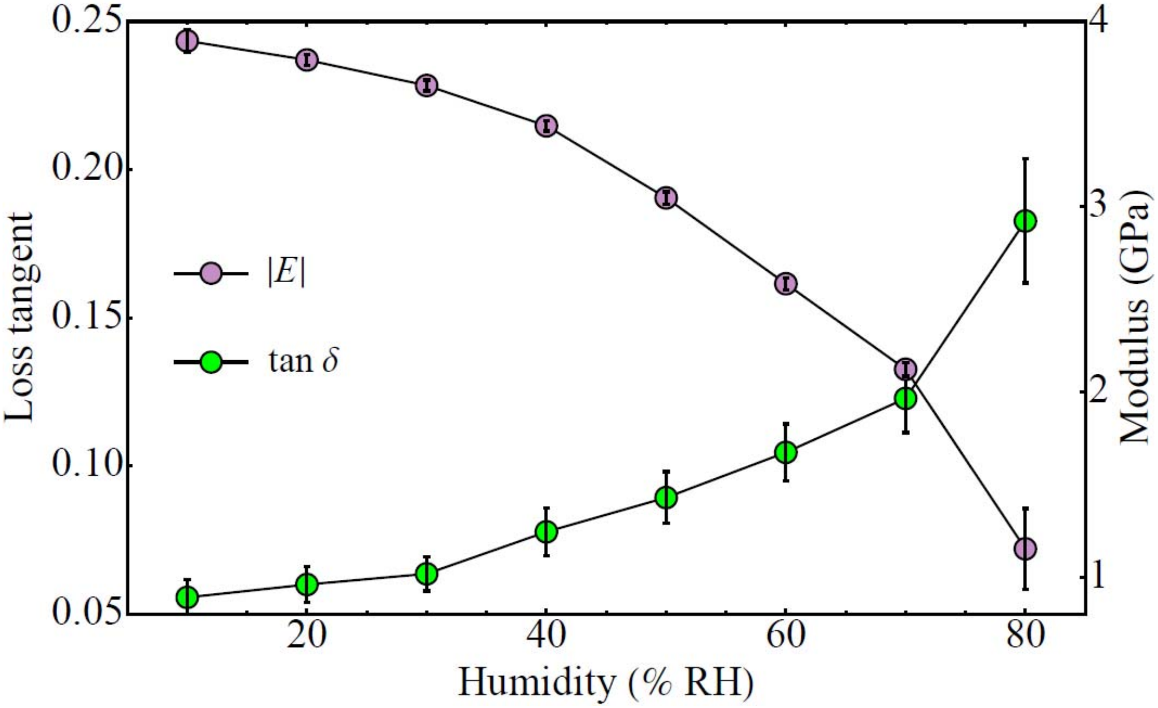

Figure 4.4. The viscoelastic parameters from the DMA experiments (see chapter 3) as measured at different humidities. A drop in the complex modulus, |*E*| concurrent with a rise in tan□ is indicative of a drop in the storage modulus *E*'. The error bars represent the standard error of the mean of each set of trials (n=9).

The result confirm an increase in RH causes an increase in friction and adhesion in an isolated setal array consistent with the results of previous studies [Huber 2005, Sun 2005, Niewiaroski 2008] and hypothesis 1. In contradiction to the capillary adhesion mechanism, the results are similar, as there is an increase of contact forces with humidity on both hydrophobic and hydrophilic surfaces, rejecting hypothesis 2. Enhanced adhesion with increasing RH occurring on hydrophobic surfaces cannot be due to the formation of capillary bridges between the setal array and the substrate. As such capillary formation will reduce adhesion [Israelachvili 1992; pg 331]. Additionally, at shear rates exceeding the maximum shear rate expected to allow capillary formation, a decline in forces at high RH was not observed. Thus, rejecting hypothesis 3. Taken as a whole these results strongly suggest capillary forces do not have a major influence on gecko adhesion and cannot explain the increase of contact forces with increasing RH.

Rejection of hypothesizes 1, 2, and 3, leaves hypothesis 4. Keratin is known as a structural protein, and the stiffness of keratin is strongly affected by humidity [Bonser 2002, Bonser and Purslow 1995, Fraser and MacRae 1980, Taylor 2004] and viscoelastic loss [Danilatos 1981, Mukherjee 2000]. The DMA results (discussed in chapter 3) show that gecko setal keratin is no different in this regard. An increase in RH from 10% to 80% reduced the elastic modulus 75% and increased the loss tangent 4-fold, indicating the keratin becomes softer with an increase in viscoelastic loss. It is known that viscoelastic properties can influence adhesion [Kendall 1979], with high viscoelastic loss corresponding to increase in adhesion. The so called 'chewing gum effect.'

4.4 Fracture of Adhered Surfaces

Modern fracture mechanics is based in the pioneering fracture mechanics work of Inglis [Inglis 1913]. He demonstrated that the stresses near a crack tip (σ) in a material under load can be higher than the stress in the bulk (σ_∞) and derived the following

$$\sigma = \sigma_\infty \left(1 + 2\sqrt{\frac{a}{r}}\right) \qquad \text{Eqn. 2}$$

Where *a* is the crack tip length (or 2a if an internal crack) and *r* is the crack tip radius. However, difficulties arise with this equation as very sharp cracks, where r→0, stress at the crack tip will become exceedingly large. Hence, to the contradiction of observation, very fine surface scratches should result in most structures failing under applied load. This dilemma was solved by Griffith [Griffith 1921], who mathematically described fracture for brittle processes where energy-absorbing processes (plastic deformation) are minimal and the major energy penalty to crack propagation is the formation of new surface area. Griffith working with fracture of glass experimentally validated his energy balance theory

$$d/da[U_p + U_E + WA] = 0 \qquad \text{Eqn. 3}$$

Where contact area A, work of adhesion W, crack length a, elastic energy and applied energy U_E and U_P, respectively. Or in terms of energy U,

$$U = -\frac{\sigma^2 \pi a^2}{E} \qquad \text{Eqn. 4}$$

Where E is the elastic modulus, and σ is stress, only cracks with a critical crack length a_c will spontaneously grow and is written

$$a_c = \frac{2\gamma E}{\sigma^2 \pi} \qquad \text{Eqn. 5}$$

where γ is the surface energy.

However, Griffith equation only accounts for fracture energies in purely brittle material. When plastic deformation is present in fracturing materials, Griffith's surface energies consideration alone fail to provide an adequate solution. Irwin [Irwin 1948] recognized the lack of plastic deformation in Griffith's theory and remedied the deficiency by adding terms to account for plastic deformation at the crack tip and crack tip blunting. Rewriting equation 3 for energy release rate, G,

$$G = \frac{\sigma^2 \pi a}{E} \qquad \text{Eqn. 6}$$

For fracture to occur G must exceed a critical value, G_c, or fracture energy. Rearranging equation 6 and by making certain assumptions $\sigma = E\varepsilon$, and an infinite plane geometry. Once the critical fracture energy is met - fracture is rapid, one can derive

$$\sigma_f = \sqrt{\frac{EGc}{\pi a}} \qquad \text{Eqn. 7}$$

The fracture model of adhesion is based on release of stored elastic energy in the body as it peels for the substrate. In figure 4.5, consider a cylindrical fiber of radius R peeling from a surface. Under an applied stress σ, the adhered bodies will deform storing elastic energy. This stored energy related to the storage modulus (E*) and Poisson's ratio, will be released on separation of the bodies. There is, however, an energy cost of expanding the cracked region dictated by conservation principles. The cost is the work of adhesion γ (units of work/area). The energy of adhesion reflects the energy change in the system of creating the new surface and in the simplest case the energy of the vdW bonds between the adhered bodies. When these two energy contributions are balanced, criteria for detachment can be described [Gao and Yao 2004, Gao et al 2005].

$$\sigma_a = \sqrt{\frac{8E^*\gamma}{\pi R}} \qquad \text{Eqn. 8}$$

Where E^* is the interfacial modulus of the contact, and is given by

$$[(1 - \nu^2) / E' + (1 - \nu_{\text{substrate}}{}^2) / E'_{\text{substrate}}]^{-1} \qquad \text{Eqn. 9}$$

The symbols ν and $\nu_{\text{substrate}}$ are for Poisson's ratio of the bulk keratin and substrate respectively.

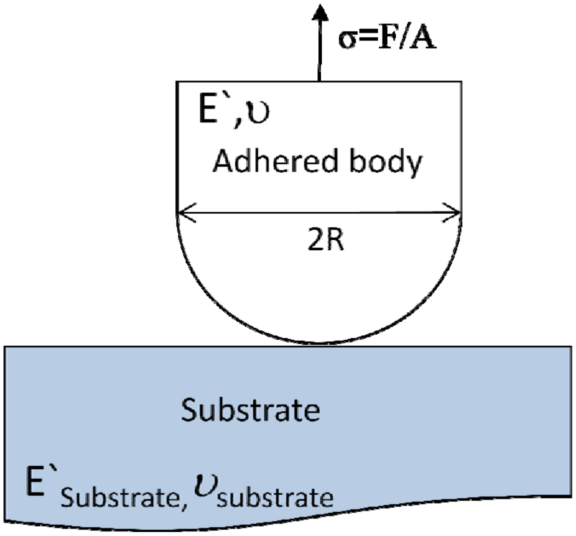

Figure 4.5. A schematic representation of the fibril/substrate interface. The work of adhesion γ, elastic storage modulus *E*' and fiber radius R are expected to be influenced by humidity. A is the cross section area ~2R, F is the applied force, ν is Poisson ratio and σ is the applied stress of the fiber.

For materials with substantial viscous component (inelastic loss) there will be additional energy dissipation far from the crack tip in the bodies themselves. As a result the energy balance of adhesion is modified to accommodate the energy loss. The work of adhesion in this case has two components, intermolecular adhesion γ_0 and viscoelastic loss to the system $\Delta\gamma$, or:

$$\gamma = \gamma_0 + \Delta\gamma(\tan\delta, \upsilon_c) \qquad \text{Eqn. 10}$$

Where $\Delta\gamma$ is explicitly a function of viscoelastic parameter $\tan\delta$ and the propagating crack tip velocity ν_c. Existing theories [Andrews 1985, Hui 1992, Saulnier 2004] treat the effect of viscoelasticity on the work of adhesion as $\Delta\gamma = \gamma_0\Phi(\tan\delta,\upsilon_c)$, that is, the influence of viscoelasticity and rate effects is through a multilicative function Φ, that includes both the rate and viscoelasticity terms. We can now modify eqn. 10, using the relation $F_a = \sigma_a A = \sigma_a \pi R^2$, where A is the cross sectional area and the simplifying assumption that the substrate is very stiff in comparison to the fiber, i.e. $E^* = E'/(1-\upsilon^2)$.

$$F_a = A\sqrt{\frac{8E`(\gamma_0+\Delta\gamma)}{\pi R(1-\upsilon^2)}} = \sqrt{\frac{8\pi R^3 E`\gamma_0(\Phi+1)}{(1-\upsilon^2)}} \qquad \text{Eqn. 11}$$

Some indications of humidity influence on adhesion are given in eqn. 11. There are three factors that are expected to be dependent on humidity: geometry (R) as a result of absorbed water induced swelling; elastic modulus (E'), as a result of softening; and the viscoelastic (tanδ), as a result of enhanced energy dissipation.

Rewriting eqn. 11 using the definition for humidity independent factors

$$F_0 = \sqrt{\frac{8\pi\gamma_0}{1-\upsilon^2}} \qquad \text{Eqn. 12}$$

Gives,

$$F_a = F_0\sqrt{R^3E'[\Phi(tan\delta, \nu_c) + 1]} \qquad \text{Eqn. 13}$$

By reformatting the pull-off force, one can segregate the substrate dependant (F_0) and the substrate independent factors.

We can explain the humidity effects using a simply heuristic argument that is based on scaling behavior of the individual variable in lieu of precise humidity dependence on geometry and visco-elasticity parameters as these are unknown. For example, in figure 4.5, the adhered fiber has a cross sectional area that scales as $A \sim R^2$, because an increase in A produces a corresponding decrease in applied stress σ, the interface between the two surfaces in effectively toughened. Assuming linear swelling with RH gives $R \sim \mathrm{RH}$. Following Saulnier et al. [Saulnier 2004], we take the β-keratin to be a "soft solid" and therefore have multilicative $\Phi \sim v_c \tan^2 \delta$ (cf. $\tan\delta = E''/E'$). From equation 13, pull-off force will overall vary as $(E')^{-1}$. The dependence of E' on humidity can be assumed now as $(E')^{-1} \sim (\mathrm{RH})^m$, where $m > 1$ (cf. Figure 4.5). Finally, since the crack extension velocity ν_c is parallel to the drag velocity υ enforced by our experimental setup, $v_c \sim v$ and we have

$$\sqrt{R^3 E'(\Phi+1)} \propto \sqrt{v}(\mathrm{RH})^{\frac{3+m}{2}} \qquad \text{Eqn. 14}$$

Eqn. 14 is an expression elucidating how the humidity dependant section of eqn. 13 is expected to behave as RH increases.

Letting $\xi = (3m) / 2$, which describes the highest order humidity effect on adhesion and will dominate at high RH, so we can now write a final expression for pull off force:

$$F_a = \alpha F_o \sqrt{\upsilon}(RH)^{\xi} + \varphi(RH, \upsilon) \qquad \text{Eqn. 15}$$

Where σ is the highest order term in (RH, υ) and the φ is composed exclusively of the terms that are asympticaly small. It should be noted that the form of eqn. 15 does not exclude additional, linear increase in vdW dispersion forces with increasing humidity as proposed by

Huber [Huber 2005]. Instead it indicates the contribution of viscoelastic effects will dominate.

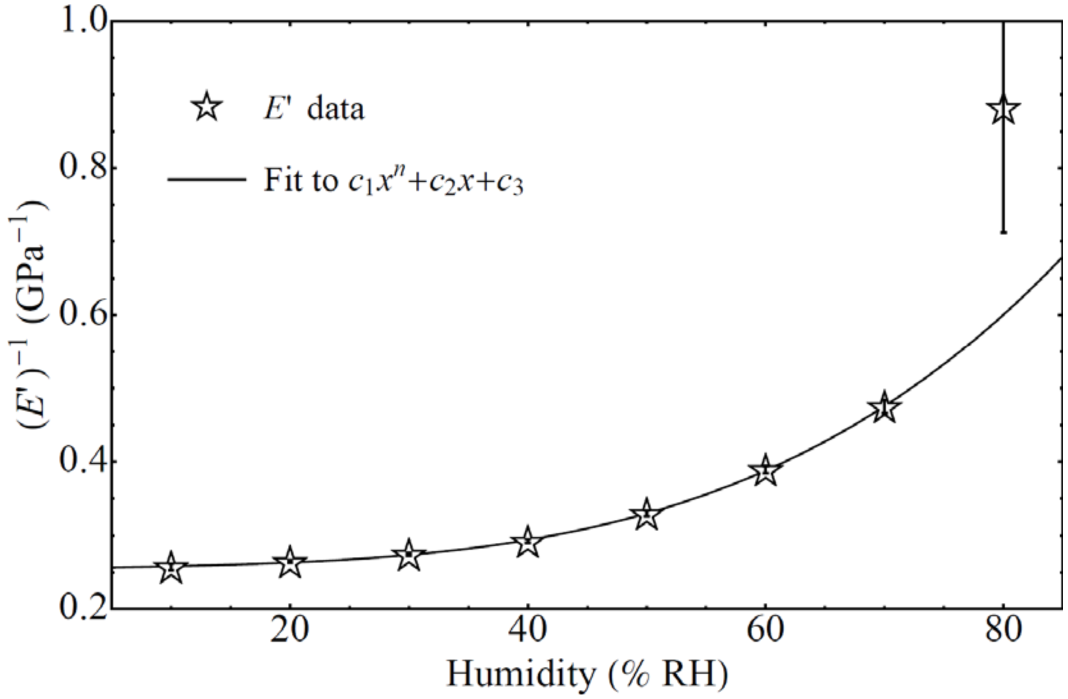

Figure 4.6 The relationship between storage modulus and humidity. The non-linear fit gives a relationship $(E')^{-1} \sim (RH)^{3.6}$. The error bars are the result of error propagation from the data in Fig.4.4.

Applying eqn. 15 to the data, the trends can be adequately described. From figure 4.6 which is derived from figure 4.4 shows a $(E')^{-1}$ dependency. From a linear fit to this series, m is estimated to be 3.6 ± 0.2. For this value of m, $\zeta = 3.3 \pm 0.1$. This exponent is in agreement with the shape of the adhesive force verses humidity curves for all velocities. To demonstrate the correlation, figure 4.7 has all of the adhesion force curves collected on Ga-As substrate on log-log axes. A linear fit to the high humidity (RH ~60%) portions of each of these series allows the determination of the exponent $\zeta_{Ga\text{-}As} = 3.0 \pm 0.2$. A similar analysis for SiO_2 series yields $\zeta_{SiO_2} = 2.8 \pm 0.2$. The values of ζ_{SiO_2} and $\zeta_{Ga\text{-}As}$ are similar as is expected for substrate independent adhesion behavior. From our calculated value of ζ the measured values are smaller. As further confirmation of the validity of eqn. 15 is shown in figure 4.8 which plots (adhesion force)^2 verses test velocity for the data set on Ga-As at varying humidity levels. Despite noise at low humidity, the linear trends indicate that adhesive force $\sim \sqrt{\upsilon}$.

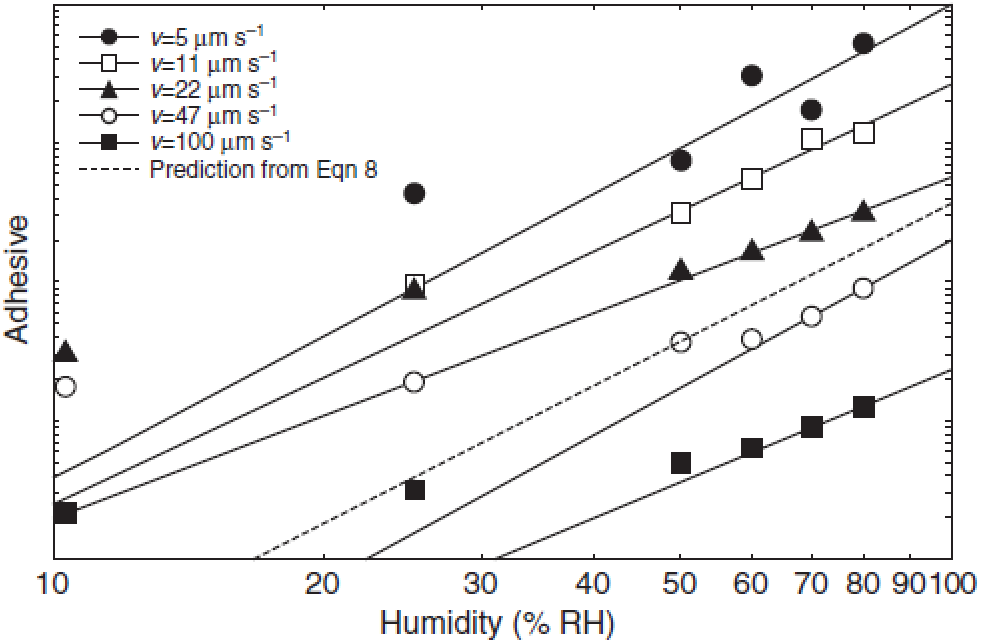

Figure 4.7. Power law fits of adhesion data on GaAs at all velocities. For the sake of clarity the vertical position of each curve has been adjusted. From these fits, the exponent $\zeta_{Ga\text{-}As}$ was determined to be 3.0 ± 0.2. These exponents/slopes are in rough agreement with the expected value, depicted as a line with slope $\zeta = 3.3$. Axes are log-log scale.

Pesika [Pesika 2009] speculated rearrangement of the proteins on the keratin surface and surface properties modifications can alter adhesion; we do not include these effects in eqn. 15. We expect surface modification to influence the short range parameter γ_0. Consequently our estimate of ζ is subject to error. The discrepancies in our measured values could be affected by this surface modification. Still, we know the change in surface energy is quite small over the RH 0-100% [Pesika 2009]. Also there are complicating effects arising from the fibril structure of the arrays which need to be included in the model of gecko adhesion, but our data is quite encouraging with the agreement of asymptotic force in eqn. 15. It is reasonable to assume a simple multiplicative effect for such large number of adhered structures.

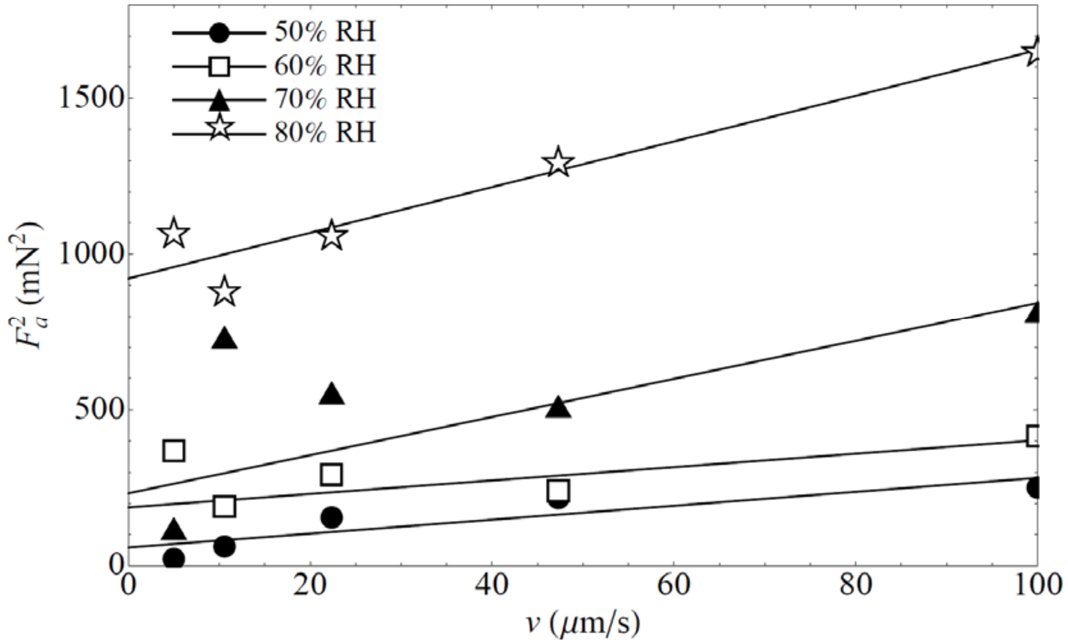

Figure 4.8 Scaling of adhesive forces (F_a) with velocity. When (adhesive force)^2 is plotted against velocity (v), resulting in linear behavior, confirming the correlation $F_a \sim v^{1/2}$.

4.5 The Nature of Friction

Friction is a resistive force that acts to retard the relative motion of two bodies in contact. There are two causes of friction, adhesive and energy dissipation [Goryacheva 1998, page 5]. The first is the work done making and breaking adhesive bonds. It is the force needed to shear the bonds in the contact zone between the bodies and is termed the molecular component of friction. The second friction component is the energy dissipation of deformation of the contact bodies. It is dependent on the mechanical properties of the material, surface geometry, and applied force.

A very simple relationship can be established in accordance to Amontons' laws of friction [Amontons 1699] and later verified and expanded by Coulomb [Coulomb 1799]. First law of friction; friction is proportional to load i.e. $F = \mu\rho$, where ρ is load, μ is the coefficient of friction and F is the force. Therefore,

$$F_f = \mu(F_n + F_a) \qquad \text{Eqn. 16}$$

Where friction force F_f is proportional to the coefficient of friction (macroscopic), multiplied by the sum of applied normal force F_n and adhesive force F_a. To be more accurate in a viscoelastic system F_n will have to take into account dispersive energy loses.

For a single asperity consistent with the spatula dimension, friction;

$$F_{||} = \tau \cdot A \qquad \text{Eqn. 17}$$

where A is the contact area and τ is the shear strength where $\tau \approx G/30$, where G is the shear modulus [Carpick 1999].

$$G = \frac{E}{(1+\upsilon)} \qquad \text{Eqn. 18}$$

The measured elastic modulus decrease of setal keratin is consistent with other keratins [Bonser 2002, Bonser and Purslow 1995, Fraser and MacRae 1980, Taylor 2004, Danilatos 1981] it is reasonable the shear modulus behavior is similar as well. Given the reduction in shear is opposite of $F_{||}$, the increase in contact area must be large for equation 17 to be maintained. It is likely the reduced elastic modulus increases compliance of the setae and the number of setae making contact with the surface. It is possible that the some of the additional contact area is a result of setal/spatula swelling with water absorption. Furthermore, once adhered the to the surface, setae will be require more detachment energy; due to less favorable crack propagation at the interface, and so called 'chewing gum' effect, where peeling energy is dissipated due to visco-elastic loses in the material and it not transmitted to the interface [Kendall 2001 pg. 166].

The elevated observed adhesion and friction at higher shear rates, indicates a shear strengthening effect on the contact has not been investigated. The effect is independent of the substrate and becomes to some extent more pronounced at higher humidity. This could be a manifestation of the reduction of the time dependant visco-elastic component at high shear rates, i.e. the material hardens much like silly putty does at high shear rates. This will result in a stiffening of the interface. Once the setae become detached from the surface they are able to relax.

4.6 Conclusion

Significant changes in viscoelastic response and elastic modulus were measured at varying atmospheric humidities, exemplified by a reduction of the elastic modulus of ~1/3 at 80%RH and an increase of nearly 4-fold in the viscoelastic loss. Enhanced energy dissipation and reduced strength has profound influence on the contact energetic and contact zone peeling. These changes in materials properties can strengthen the interface between the gecko's setae and the adhered surface. The near absence of adhesion below 15% RH, and substantial adhesion in RH ranges expected in the native Tokay habitat, leaves us to consider if atmospheric moisture is required for attachment or if geckos native to dryer climates suffer from impaired adhesion. Not for capillary adhesion mechanism but rather to soften the β-keratin.

Changes in mechanical properties of the setal keratin best explains the increased adhesion at higher humidities as observed in geckos. Capillary forces are not a sufficient factor and do not explain the observed behavior, leaving only van der Waals force the only empirically supported mechanism for gecko adhesion.

References

Amonons, G, De la résistance cause dans les machines, Mémoire de Mathématiques et de Physique de l'Académie Royale, A, 66, 82 (1699) 275-282

Andrews, E.H., The role of viscoelasticity in adhesion. J. Polym. Sci. Pol. Sym. 72 (1985) 295-297

Autumn, K. , Sitti, M., Peattie, A., Hansen, W., Sponberg, S., Liang, Y.A., Kenny, T., Fearing, R., Israelachvili, J., Full, R.J., Evidence for van der Waals adhesion in gecko setae, Proc. Natl. Acad. Sci. 99 (2002) 12252-12256.

Bonser, R.H.C., Purslow, **P.P.,** The Young's Modulus of Feather Keratin, J. Exp. Biol., 198 (1995) 1029-1033.

Bonser, R.H.C., Hydration sensitivity of ostrich claw keratin, J. Mater. Sci. Lett. 21 (2002) 1563-1564

Carpick, R. W., Enachescu, M., Ogletree, D. F. and Salmeron, M. Making, breaking, and sliding of nanometer-scale contacts. Mat. Res. Soc. Symp. Proc. 539, (1999) 93-101.

Chen, B., and H. Gao, An Alternative Explanation Of The Effect Of Humidity In Gecko Adhesion: Stiffness Reduction Enhances Adhesion On A Rough Surface International Journal of Applied Mechanics Vol. 2, No. 1 (2010) 1–9 Imperial College Press

Coulomb, C. A., Théorie des machines simple, Mémoire de Mathématiques et de Physique de l'Académie Royale, 61 (1785) 161-331

Danilatos, G.D., Postle, R., Dynamic Mechanical Properties of Keratin Fibers During Water Adsorption and Desorption. J. of Appl. Poly. Sci. 26 (1981) 193-200

Fraser, R.D.B., and Macrae, T.P., Molecular and mechanical structure of keratins, Symp. Soc. Exp. Biol. 34 (1980) 211-246

Gao, H., Wang, X., Yao, H., Gorb, S., and Arzt, E., Mechanics of hierarchical adhesion structures of geckos. Mech. Mater (2005) 37, 275-285

Goryacheva, I.G., Contact Mechanics in Tribology. Kluwer Academic Publishers. Dordrecht, The Netherlands 1998.

Gravish, N., Wilkinson, M., Sponberg, S., Parness, A., Esparza, N., Soto, D., Yamaguchi, T., Broide, M., Cutkosky, M., Creten C., Rate-dependent frictional adhesion in natural and synthetic gecko setae. J. R. Soc. Interface, **7,** 43 (2010) 259-269.

Griffith, A.A., The phenomena of rupture and flow in solids. Philos Trans R. Soc Lond. A221 (1921) 163-198

Huber, G., Mantz, H., Spolenak, R., Mecke, K., Jacobs, K., Gorb, S., Arzt, E., Evidence for capillarity contributions to gecko adhesion from single spatula nanomechanical measurements. Proc. Nat. Acad. Sci. 102 (2005) 16293-16296.

Hui, C.-Y., Xu, D.-B., and Kramer, E.j., A fracture model for a weak interface in a viscoelastic material (small scale yielding analysis). J. Appl. Phys. 72 (1992) 3294-3304

Inglis, C., Stress in a plate due to the presence of cracks and sharp corners. Trans. Inst. Naval Architects, 55 (1913) 187-96

Irwin, G.R., Fracture dynamics, in Fracture of Metal. ASM. (1948) 152-69

Israelachvili, J., Intermolecular and Surface Forces, Academic Press, New York, 1992.

Kim, T. W. and Bhushan, B. The adhesion model considering capillarity for gecko attachment system. J. R. Soc. Interface 5 (2008) 319-327

Kendall, K., The Connection Between Fracture Energy and the Inelastic Behavior. Acta Metall. 27 (1979) 1065-1073

Kendall, K., Molecular Adhesion and Its Applications. Khuwer Academic Publishers, New York, 2001

Mukherjee, S., Richardson, N., Margosiak, M., Lei, X., Understanding dry skin: a physical basis for the effects of dry environment and surfactant treatment on corneum fracture, Processing of the 5th royal society, unilever Indo-Forum in materials science. Imperial college press, 2000. pg 306-324

Niewiarowski, P. H., Lopez, S., Ge, L., Hagan, E., Dhinojwala, A., Sticky Gecko Feet: The Role of Temperature and Humidity. PLoS ONE 3 (2008) e2192.

Pesika, N.S., Zeng, H., Kristiansen, K., Zhao, B., Tian, Y., Autumn, K.. Isrealachvili, J., Gecko adhesion pad: a smart surface? J. Phys.-Condens. Mat., 2009. 21 (46), 2009, 464132.

Saulnier, F., Ondarcuhu, T., Aradian, A., and Raphael, E., Adhesion between a viscoelastic material and a solid surface. Macromolecules. 37 (2004) 1067-1075

Sun, W., Neuzil, P., Kustandi, T. S., Oh, S. and Samper, V. D The nature Of the gecko lizard adhesive force. Biophys. J. 89 (2005) L14-L17.

Szoszkiewicz, R., Riedo, **E.,** Nucleation Time of Nanoscale Water Bridges. Phys. Rev. Lett. 95 (13) 2005 135502.

Taylor, A.M., Bonser, R.H.C., Farrent, **J.W.,** The influence of hydration on the tensile and compressive properties of avian keratinous tissue. J. Mater. Sci. 39 (2004) 939-942.

Chapter 5 Initial surface chemical analysis of gecko setal arrays and scales

5.1 Chemical analysis of setal keratin

Although bulk chemical analysis of beta-keratin is documented [Fraser 1980 and 1996, Rizzo 2005, Alibardi 2003 and 2011 etc.], surface chemical analysis is in general limited for keratins with some exceptions for wool (alpha-keratin) [Molina 2002 and 2005 etc.] and there are no known publications pertaining to geckos or beta-keratin with the exception of [Hsu 2011]. Using an indirect method of SFG (Sum Frequency Generation) spectroscopy of residue from gecko foot falls on sapphire substrate, reported the presence of phospholipids in the residue.

Surface sensitive technique, XPS (x-ray photoelectron spectroscopy) also referred to as ESCA (electron spectroscopy for chemical analysis) and a related technique Near Edge X-Ray Absorption Fine Structure, NEXAFS, are surface sensitive technique enabling the determination of the chemical composition and local chemical environment of the outer ~100Å of the material, with the exception of H and He. XPS measures the energy of the ejected core photoelectron, whereas NEXAFS measures secondary emission processes from the core-hole annihilation, and consequently yields greater detail of the local chemical bonding environment at the material's surface. While these surface techniques can identify chemical elements and information about the bonding environment with some structural details (organization and orientation) there are limits. Chemical compounds cannot be identified in complex materials such as biological samples, only bonding types and elemental detection limits are on the order of a few atomic percent.

5.2 Background

Proteins are composed of chains of amino acids with a generic formula $H_2NCH\mathbf{R}COOH$ with R being one of 20 side groups. Nitrogen can be used as a proxy for protein concentrations in biological materials, since nitrogen contend is predominantly protein based.

While there are many varieties of carbohydrates, a typical monosaccharide has an aldehyde group and hydroxyls with a generic structure $H\text{-}(CHOH)_x(C{=}O)\text{-}(CHOH)_y\text{-}H$. Lipids have high hydrocarbon content with a head that typically contains C=O and can also contain phosphorous. Similarities in the chemical bonding structures make disseminating lipids and carbohydrates difficult with XPS or NEXAFS particular in complex biological materials. However, ratios of the chemical components can provide insight.

The photoelectric effect was first discovered by Hertz in 1897. After, 70 years, commercial instruments began to appear in 1969 [Briggs 1998 pg. 7]. These machines used either Al Kα x-ray source (1486.6eV) or Mg Kα (1253.6eV). NEXAFS utilizes high intensity and tunable synchrotron radiation [Stohr 1992 pg. 115], began to be utilized in the 1970's to provide greater spectral detail. By the mid 1980s it was realized that NEXAFS could provide great detail of the fine atomic structure below the ionization potential, and can be useful in determining the local chemical bonding environment.

The primary constituent of the excitement process from an incident x-ray of sufficient energy is the generation of photoelectrons. Secondary de-excitation process associated with core hole annihilation are either radiative, fluorescent photons, or non-radiative, Auger electrons. The emission of which can be measured in both energy and quantity. *See figure 6.1.*

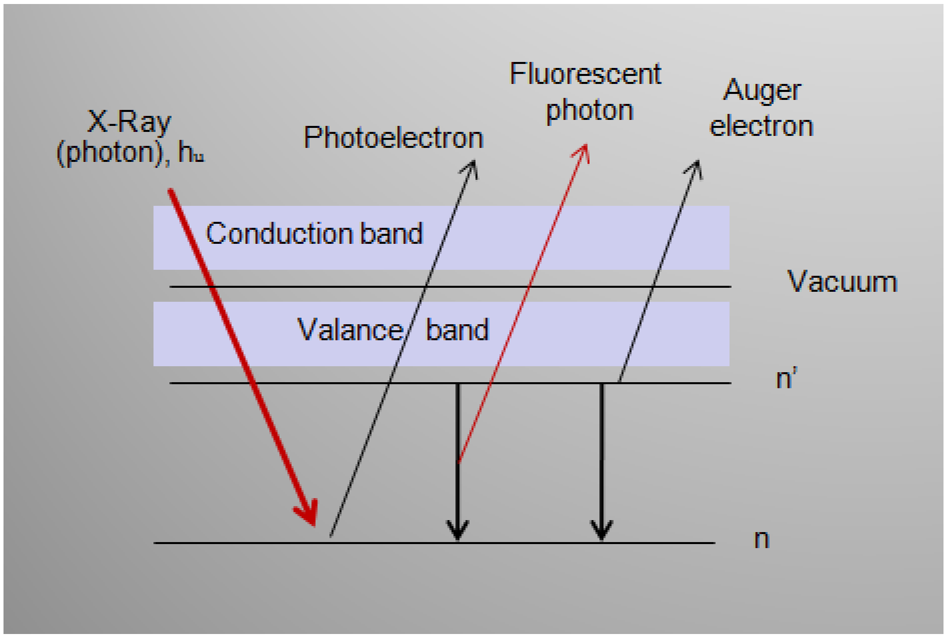

Figure 5.1. Schematic of relevant outcomes of x-ray excitement; photoelectron ejection, Fluorescent photon or Auger electron. For low Z elements, only K shell produces emissions of interest.

Each element has characteristic photoelectron emission energies. Slight differences in the energy and peak shape result from the local chemical bonding environment. The binding energy of a photoelectron, E_b is described

$$E_b=h\nu-E_{kin}-W_f \qquad \text{Eqn. 1}$$

where E_{kin} is the kinetic energy of the photoelectron, $h\nu$ is energy of the incident photon, and W_f is the work function of the sample. For keratins the binding energies for the elements of interest are, C 1S (~285eV), N 1S (~400eV), O 1S (~535eV), S 2P (~164eV), and P 2P (~134eV).

We want to measure the signal proportional to the x-ray absorption cross-section, the number of photons absorbed is

$N_{abs}=I_oA_o(1-e^{-sx(h\upsilon)\rho}) \sim I_oA_o\sigma_x(h\upsilon)\rho$ Eqn. 2

Where I_o is the incident photon flux density [photons/(s cm^2)], A_o [cm^2] is the area exposed to the photon beam, which also is dependent on the incident beam angle, ρ is the atomic density [atoms/cm^2], $\sigma_x(h\nu)$ and is the x-ray absorption cross section. Therefore, the number of absorbed photons is directionally related to the absorption atomic cross section and thusly, the number of holes and photoelectrons created. However, all structures below the ionization potential are lost if only the free photoelectrons are measured. This leads to the measurement of secondary processes of core hole annihilation. Measurements of both primary and secondary processes is the measure of the probability of core hole creation from x-ray absorption.

For secondary de-excitation processes the fraction of fluorescent yield ω_f, and auger yield ω_a satisfies the sum rule, $\omega_f + \omega_a = 1$. For low Z elements the Auger process is faster and dominates the fluorescent emission by ~2 orders of magnitude.

Molecular orbitals can be divided into bonding, non-bonding and anti-bonding (designated with *). Bonding orbitals ascribes a state when the molecule is in a lower relative energy than the free separate atoms. The bonding character is the result of constructive interference between the two atomic orbitals and the electrons in these orbitals have a higher probability to occupy the inter-nuclear region and interact with both nuclei. Molecular bonding only occurs where orbitals overlap. Sigma (σ) bonds are the strongest covalent bonds formed by overlapping orbitals with cylindrical symmetry around the inter-nuclear axis. Pi (π) bonds are weaker than sigma bonds and consist of spin pairing of two p orbitals that approach side by side. Anti-bonding orbitals, if occupied, the energy of the molecule is higher than for two separate atoms. The greater energy arises from destructive interference between the two atomic orbitals and electrons in this orbital are largely excluded from the inter-nuclear region being forced to occupy less energetically favorable locations. Consequently, energy of the ejected photoelectron, fluorescent photon or Auger electron is altered by the local bonding environment.

5.3 Experimental

Near Edge X-Ray Absorption Fine Structure, NEXAFS, performed at the National Synchrotron Light Source (NSLS) in Brookhaven National Laboratory, New York. The beam line uses elliptically polarized beam (~85%) through a monochromator and 600L/mm grating that provides a full-width-half-maximum resolution of ~0.15 eV at the carbon K-edge (285 eV). The monochromator energy was calibrated with the C 1S π* transition (285.35eV) on a graphite grid. Samples were mounted such as to allow the altering of the incident beam angle relative to the sample surface. For further details [Weidner 2010]. NEXAFS spectra were collected on the optically clear eye spectacle, scale, setal array and lamella. The eye spectacle and scale were collected from a freshly molted Tokay gecko and the setal array with lamella was collected from a live female Tokay gecko.

XPS spectra of the setal array was collected on a Kratos AXIS Ultra DLD instrument (Kratos, Manchester England), using 0° take off angle, and monochromatic Al $K_{\alpha1,2}$ x-ray source ($h\nu$=1446.6eV). The instrument was calibrated using Au_{4f} peak. *See appendix A for data*.

5.4 Results and discussion

Carbon K-edge is fairly well studied for amino acids [Zubavichus 2005, Zhang 2009, Graf 2009, Kaznacheyev 2002, Carravetta 1998, Gordon 2003]. Figure 5.2 shows the spectra for the C K-edge (1s), the spectrums are dominated by the C 1s (C=O) $\pi^*_{C=O}$ amide at 288.4eV proceeded by the π* aliphatic peak at 287.7eV and thiol σ* peak at 287.3eV. The small peak at 285eV is associated with pi bonding of aromatic carbon. There is a broad σ* C-C/C-N peak at ~292.7eV. Nearer ~302eV is $\sigma^*_{C=C}$ and $\sigma^*_{C=N}$. The intensity ratio of the aliphatic vs. N-C=O amides suggests the setal arrays have less protein in relation to another constituent. Also indicative of the eye spectacle contains little aromatic carbons. The spectacle has a more distinct peak at 292.7eV and absence of the feature at ~285eV. The profiles of the setae and lamella are similar with less distinct features compared to the scale and spectacle.

The aromatic carbon peak at 285eV is present in amino acids, phenylalanine, tryptophan, and tyrosine. Both phenylalanine and tyrosine are known from bulk chemical analysis to be present in lizard claw [Fraser 1972]. The peak is present for all samples with the exception of the eye spectacle. The setae prominent peak, ~288eV has a substantial constitute on the leading edge, either from σ^*_{C-H} or possibly contribution from σ^*_{C-S}. Sulfur is present in the setae as indicated by XPS (appendix A), but the concentration was low. It could be due to higher C-H constituency in the setae, a possible indication of lipids. Additionally the $\pi^*_{C=O}$ peak is weaker in the setae sample; this also lends some support to lipid presence. The broad peak near 292-295eV on the setae is biased towards the lower energy; some indication of C-C/C-O ratio is lower for the setae sample.

Table 5.1. Spectral features for carbon K-edge as observed from NEXAFS.

Component	Transition	Energy
aromatic	$\pi^*_{C=C}$	285eV (*a*)
aliphatic	σ^*_{C-H}	287.7-288.5eV (*a,d*) 291eV(*b*)
Thiol	σ^*_{C-S}	287.3eV (*c*)
Amide/ketone/carboxyl	$\pi^*_{C=O}$	288.2-288.7eV (*a,b,c*)
	σ^*_{C-OH}	289.6-290.6eV(*c*)
Amine	σ^*_{C-N}	290.3-291eV (*c*), 292.0-.9eV (*a*)
Alkyl	σ^*_{C-C}	293.0-297eV (*c*), 292.0-.9eV (*a*)
Alkene	$\sigma^*_{C=C}$	301.5-302.5eV(*a*)
	$\sigma^*_{C=N}$	301.5-302.5eV(*a*)
	σ^*_{C-O}	302eV(*b*)

(a) [Graf 2009] (b) [Gordon 2003] (c) [Zubavichus 2005] (d) [Kaznacheyev 2002]

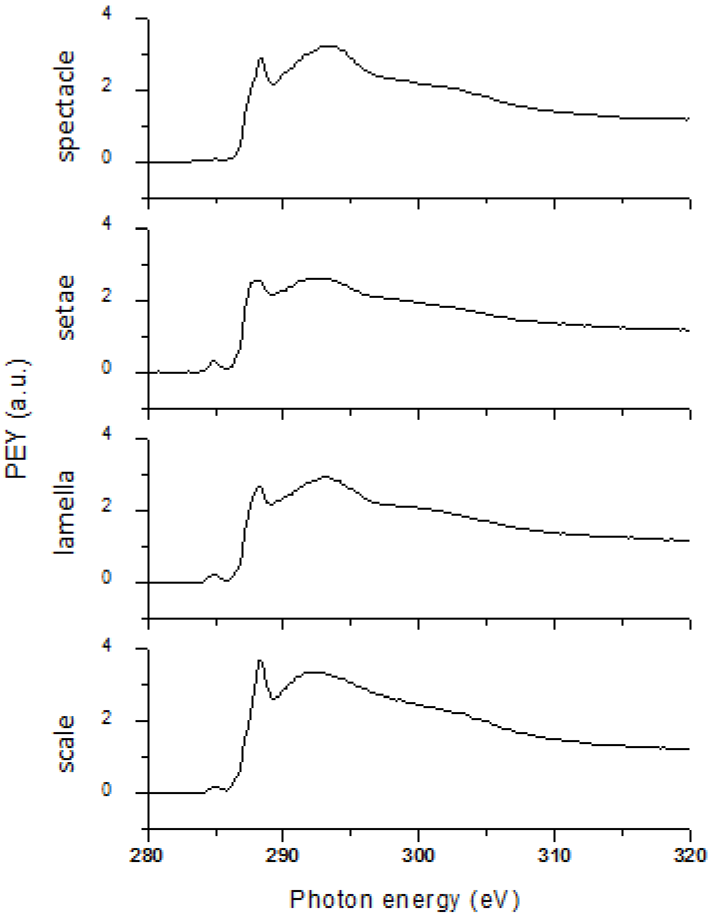

Figure 5.2. Pre-/post-edge normalized Carbon K-edge spectra for Tokay eye spectacle, lamella, setae, and scale from near the eye.

Taking advantage of the polarized synchrotron radiation and the dependence of the resonance intensities on the electric field vector ***E*** relative to the molecular axis (***E*** field parallel to the orbital axis creates a strong resonance), surface organization can be determined. Difference spectra (incident beam angle 80°-30°) shown in figure 5.3 are indicative of ordering. The strong difference in the eye spectacle difference spectra indicates a more ordered β-keratin structure, with the least structure in the setal array. The strong σ* peak at 80° with much weaker σ* at 30° is indicative of the σ* orbitals are parallel to the surface. Additionally, the π* peak is larger at 30° which also supports that the π* orbitals at the surface are preferentially oriented perpendicular to the surface. Although there is some surface roughness influence, with both the setal array and lamella being rough on the micron scale and the eye spectacle being smooth for optical proposes. The absence of a stronger difference spectra on the lamella and setae is likely due to surface roughness, since it is known that keratins have roughly 1/3 cystallinity by volume [Fraser 1972].

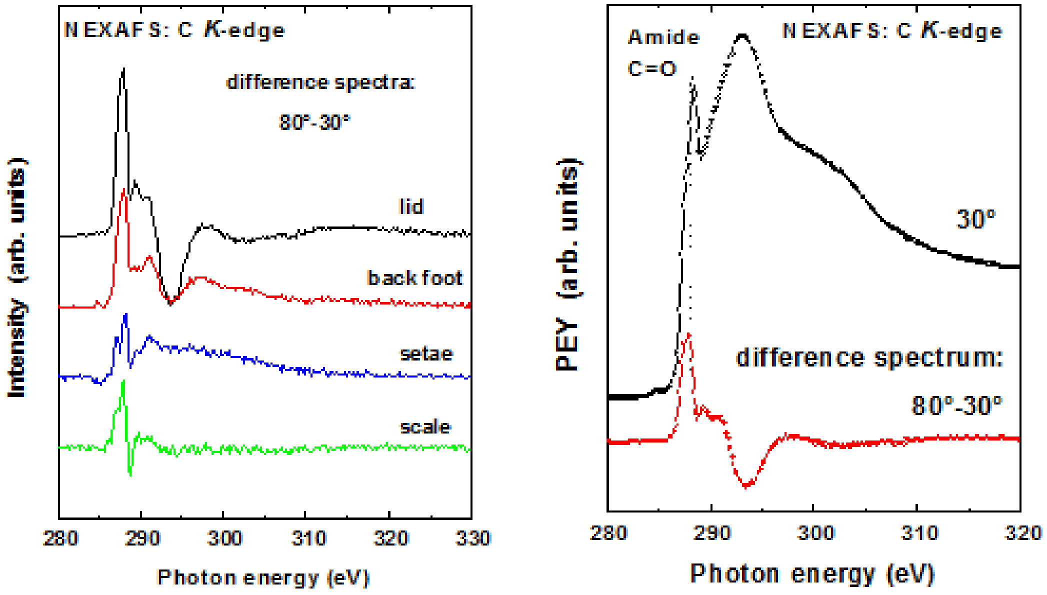

Figure 5.3. Carbon K-edge 80°-30° delta spectrums. Left: carbon K-edge spectrum for eye spectacle (black), Lamella (red), setae (blue), scale from near the eye (green). Right carbon K-edge spectra for the eye spectacle at 30 degrees (black) and the spectrum delta from 80°-30° (red). The strong difference in the eye spectacle spectrum indicates an ordered structure.

Figure 5.4 shows the oxygen K-edge spectra with the characteristic π* and σ* resonance. A sharp feature at 530eV relates to the transition of the $\pi^*_{C=O}$ orbital, at 532.3eV is the π^*_{COOH} which shows a small shoulder on the setae and lamella profiles, this shoulder in not visible on the scale or spectacle due to the much stronger $\sigma^*_{O\text{-}H}$ peak at 539.2eV. At higher energy lies the $\sigma^*_{C\text{-}O}$ peak at ~ 545eV. The peak ratios are varied across the four samples. However, the peak ratios are quite similar between the lamella and setae, the peak ratios are also similar between the eye spectacle and scale. The $\sigma^*_{O\text{-}H}$ peak at 539.2eV and ~545eV $\sigma^*_{C\text{-}O}$ peak for the spectacle/scale is more intense than in the setae/lamella.

Table 5.2. Spectral features for oxygen K-edge as observed from NEXAFS.

Component	Transition	Energy
COO/CONH	$\pi^*_{C=O}$	530eV
COOH	$\pi^*_{C\text{-}OH}$	532.3eV
C-H	$\sigma^*_{O\text{-}H}$	539.2eV
COO/CONH	$\sigma^*_{C\text{-}O}$	545eV

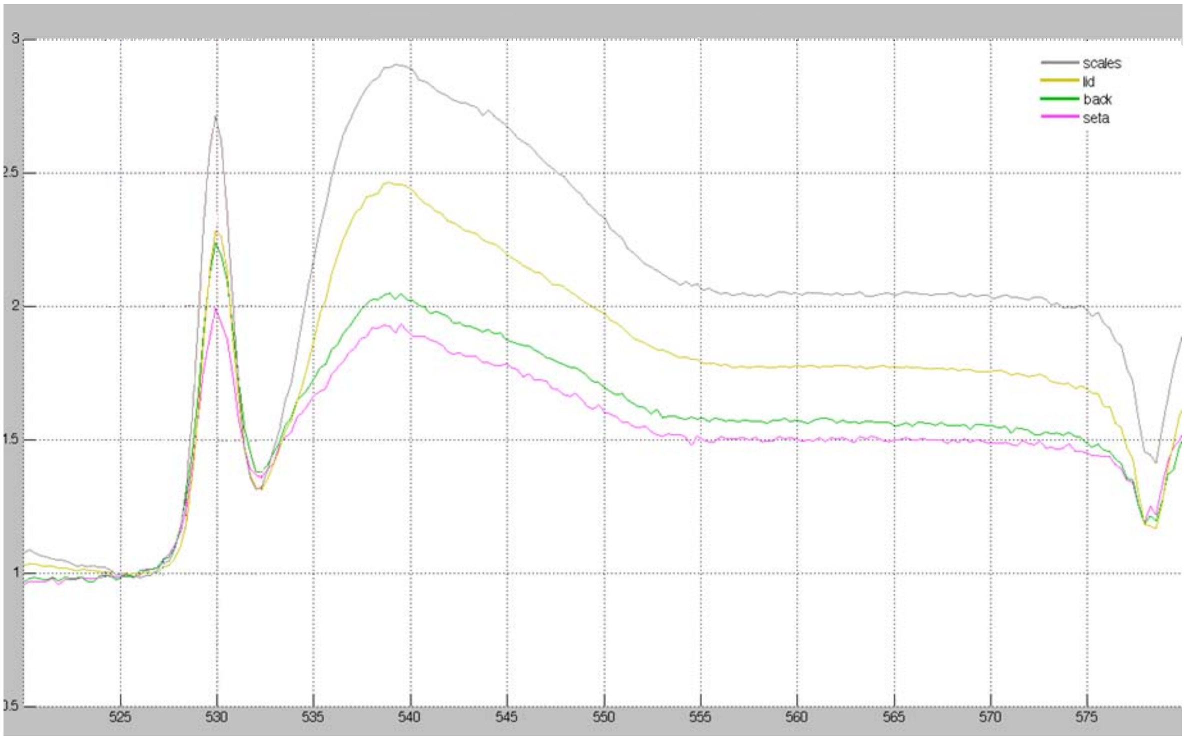

Figure 5.4. Pre-edge normalized oxygen K-edge spectra, C-O π* at ~530eV and C-O σ* at ~539eV. Scale (grey), eye spectacle (yellow), lamella (green) and setae (magenta). The post edge is not normalized; the height of the flat portion on the post edge is relative to the oxygen in the sample.

Nitrogen is only found in proteins and is indicative of the presence and concentration on protein. Figure 5.5 shows the nitrogen K-edge spectra of the gecko samples, the spectra are dominated by a broad σ* resonance peak in the vicinity of 406.5eV attributed to the C-H bonds and an intense peak near 402 eV of the N 1s→$\pi^*_{C=O}$(C=ONH) transition. Near 412eV is the σ^*_{C-N} peak. Peak ratios 406.5eV and 412eV are fairly consistent across the sample with the exception of the scale which shows a greater disparity between the intensities of the two peaks with the emphases on the 406.5eV peak. Setae specimen has the lowest nitrogen content and amide π* intensities relative to the nitrogen post edge, suggesting the setae have the least amount of protein of the four samples measured. Figure 5.6 shows the amide π* intensity. The scale has the most nitrogen present and likely the most protein content with the eye spectacle and lamella protein content in between that of the setae and scale.

Table 5.3. Spectral features for nitrogen K-edge as observed from NEXAFS.

Component	Transition	Energy
CONH	$\pi^*_{C=O}$	402 eV
C-H	σ^*_{C-H}	406.5eV
C-N	σ^*_{C-N}	412eV

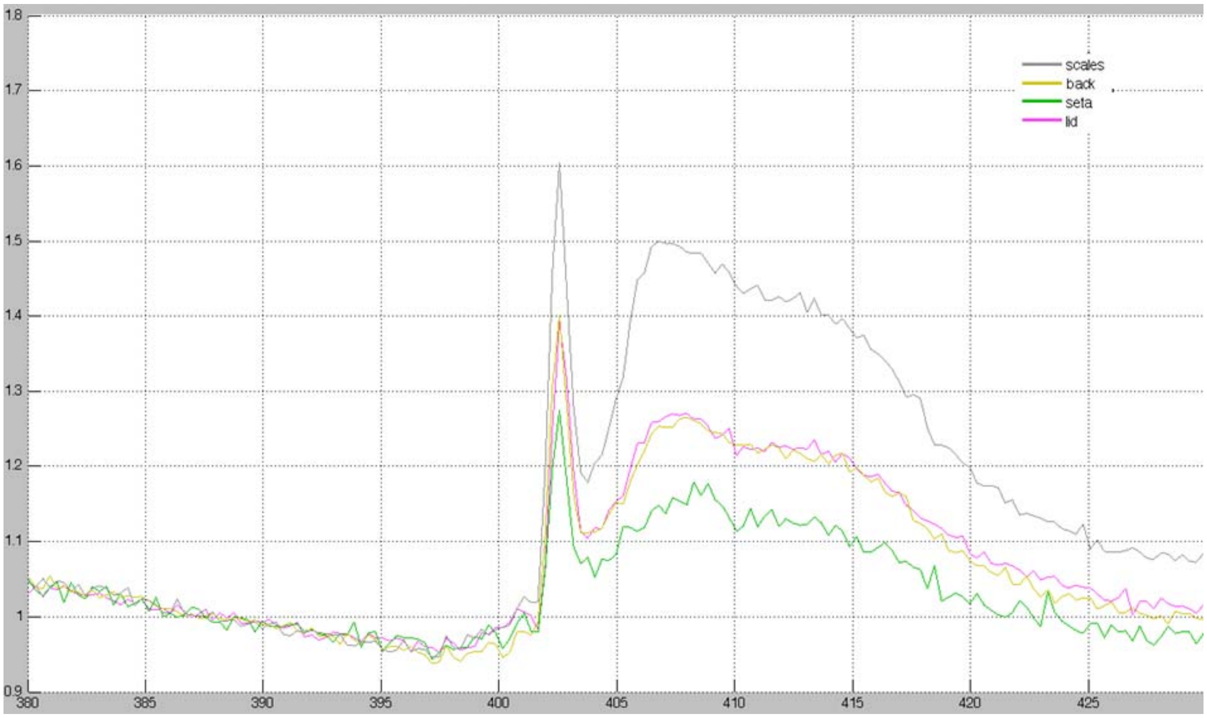

Figure 5.5. Pre-edge normalized nitrogen K-edge spectra, amide π* analysis is sensitive to the amount of protein. Scale (grey), eye spectacle (yellow), lamella (green) and setae (magenta). The post edge is not normalized; the height of the flat portion on the post edge is relative to the nitrogen in the sample. The least amount of nitrogen and probably protein was detected in the seta arrays with the highest amount detected in the scales.

The complexity of the chemical signature convolutes signals from individual amino acid groups but some correlations can be extrapolated. Isolated amino acid NEXAFS signatures are available in the literature [Zubavichus 2005, Graf 2009, Gordon 2003, Zubavichus 2005, Kaznacheyev 2002]. The strong peak at ~402 eV assigned to CONH group can also be assigned to indol (aromatic heterocyclic of six-carbon benzene ring fused with five-carbon nitrogen contain ring) and guanidine $[N_3H_5]^+$ groups found in tryptophan and arginine, respectively. Histidine with an imidazole (aromatic heterocyclic) group also has a peak near 402eV, however it also has a preceding peak at 399.8eV [Zubavichus 2005] that is not present. Additionally, the π^*_{CONH2} peak at 400.7eV appears not to present or lost in the noise of the measurement. At higher energies the $\sigma^*_{C\text{-}N}$ peak from nitrogen hetrocycle (~410eV) is only present in hydroxyproline, proline, glutamine, and histidine [Zubavichus 2005].

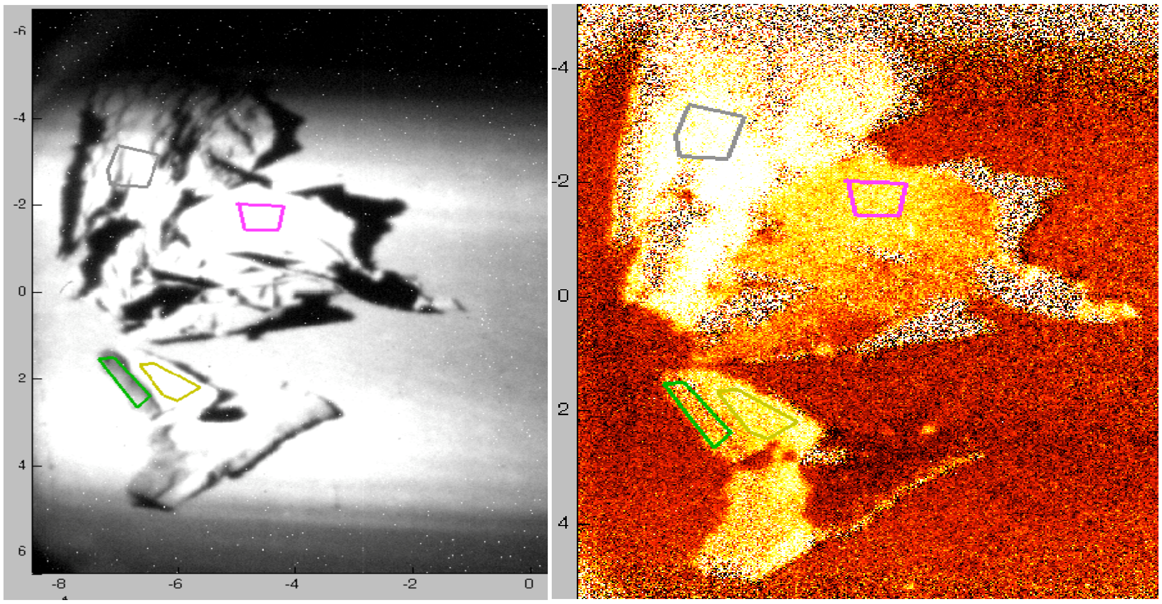

Figure 5.6. Image left: Optical image of the samples mounted for NEXAFS, Image right: Image based on amide π*. Setae (green), Lamella (yellow), eye spectacle (pink), scale (blue). Lighter color indicates a larger portion of amide π* bonds, i.e. protein.

From the spectral data, the setae have the least amount of protein, from the observed nitrogen K-edge and aliphatic/amide carbon K-edge ratio. The setae also have the least amount of oxygen, a fairly large component of carbohydrates, and a larger aliphatic carbon K-edge peak, aliphatic which are abundant in lipids. The setal shafts are encased in a membrane [Alibardi 2001, Rizo 2005] and lipids have been detected in the setae [Alibardi 2011] and the epidermis of gecko [Alibardi 2001] as well as in reptiles scales [Tu 2002, Alibardi 2003] and the spectral data seems to support the presence of lipids. The scales have the most protein content, from the observed nitrogen K-edge and aliphatic/amide carbon K-edge ratio, the lamella and eye spectacle intermediate nitrogen content.

While phospholipids were detected by Hsu [Hsu 2011] using SFG, phosphorous was not detected using XPS. It is likely the concentration of phosphorous was too low for detection. Hsu also raised the prospect of fluid like adhesion mechanism resulting from the observed lipid based residue. This is highly speculative and unsubstantiated given the ample evidence to the contrary [Autumn 2002a and 2002b, Prowse 2011, Putoff 2010]. In ants with fluid based adhesion mechanism the remaining residue is approximately 2μm in height at the contact location and spreads approximately the size of contact area [Federle 2002]. If we use Federle's ant model the equivalent fluid volume consumed for a gecko would greatly exceed that of the gecko by orders of magnitude, using 30,000 10μm drag cycle (total drag distance was 300m) data from Gravish [Gravish 2010]. Clearly at the conclusion of 30,000 cycles the setae and adhesion were still present. Even for very thin films of fluid remaining after each foot strike represented a substantial volume, exceeding the mass of the animal.

Table 5.4. Fluid consumption for 300m distance per gecko using a capillary model, assumes 400g gecko - surface residual fluid is proportional to contact area and thickness as listed.

contact thickness (fluid)	Fluid consumed per gecko (cc)	% body weight
1 nm	6	12%
10 nm	60	120%
100 nm	600	1200%
1 μm	6000	12000%
2 μm	12000	24000%

It is interesting to note that NEXAFS indicates the eye spectacle is more structured compared to the other samples tested; this is likely a result of the smoothness necessary for eye optics. The other samples have substantial surface roughness particularly the lamella and setae compared to the eye spectacle. This surface roughness will create larger scattering angle and decrease the angular sensitivity.

5.6 Conclusion

Initial surface chemical analysis indicates the eye spectacle is the most ordered structure, most likely a result of surface roughness. The setae showed the lowest presence of protein of the samples tested (scale, eye spectacle, lamella, and setae). Whether this result is from the presence of a thin membrane covering the setae or a manifestation of a structural difference is unknown at this time and requires further study. But initial indications seem to confirm a presence of lipids on the setae surface. The scale and eye spectacle have the highest levels of nitrogen amide intensity and ratio of the aliphatic/amides suggest higher amount of protein is present. Further surface chemistry study is needed to resolve the exact nature of the setal surface and the effect it has on adhesion and contact properties. Ideally additional surface studies will include samples in hydrated and dehydrated states.

References

Alibardi, L., Ultrastructural autoradiographic and immunocytochemical analysis of setae formation and keratinization in the digital pads of the gecko Hemidactylus turcicus (Gekkonidae, Reptilia). Tissue & Cell. 35 (2003) 288-296.

Alibardi, L., Edward, D.P., Patil, L., Bouhenni, R., Dhinojwala, A., and Niewiarwski, P.H., Histochemical and ultrastructural analysis of adhesive setae of lizards indicate that they contain lipids in addition to keratins. J. of Morph. 272 (2011) 758-768

Autumn, K. , Sitti, M., Peattie, A., Hansen, W., Sponberg, S., Liang, Y.A., Kenny, T., Fearing, R., Israelachvili, J., Full, R.J., Evidence for van der Waals adhesion in gecko setae, Proc. Natl. Acad. Sci. 99 (2002a) 12252-12256.

Autumn, K. and Peattie, A., Mechanisms of adhesion in geckos. Int. Comp. Bio. 42 (2002b) 1081–1090.

Brigg, D., Surface analysis of polymers by XPS and static SIMS. Cambridge University Press, 1998

Carravetta, C., Plashkevych, O., Agren, H., A theoretical study of the near-edge x-ray absorption spectra of some larger amino acids. J. of Chem. Phys. 109 (1998) 1456-1464

Federle, W., Riehle, M., Curtis, A.S.G., Full, R.J., An Integrative Study of Insect Adhesion: Mechanics and Wet Adhesion of Pretarsal Pads in Ants. Int. Comp. Biol. 42 (2002) 1100- 1106

Fraser, R.D.B., and MaCrae, T.P., Molecular and mechanical structure of keratins, Symp. Soc. Exp. Biol. (1980) 34, 211-246

Fraser, R.D.B., Parry, D.A.D., The Molecular Structure of Reptilian Keratin. International J. of Bio. Macromolecules. 19 (1996) 207-211

Gordon, M.L., Cooper, G., Morin, C., Araki, T., Turci, C.C., Kaznatcheev, K., Hitchman, A.P., Inner-Shell Excitation Spectroscopy of the Peptide Bond: Comparison of the C 1s, N 1s, and O 1s Spectra of Glycine, Glycyl-Glycine and Glycyl-Glycyl-Glycine. J. Phys. Chem. A 107 (2003) 6144-6159

Graf, N., Yegan, E., Gross, T., Lippitz, A., Weigel, W., Krakert, S., Terfort, A., Unger, W.E.S., XPS and NEXAFS studies of aliphatic and aromatic amine species on functionalized surfaces. Sur. Sci., 603 (2009) 2849-2860

Hsu, P.Y., Ge, L., Li, X., Stark, A.Y., Wesdemiotis, C., Niewiarowski, P.H., and Dhinojwala, A., Direct evidence of phospholipids in gecko footprints and spatula-substrate contact interface detected using surface-sensitive spectroscopy. J.R. Soc. Interface (2011)

Kaznacheeyev, K., Osanna. A., Jacabsen, C., Plashkevych, O., Vahtras, O., Agren, H., Hitchcock, A.P., Innershell Absorption Spectroscopy of Amino Acids. J. Phys. Chem. A, 106 (2002) 3153-3168

Molina, R.,Espinos J.P., Yubero, F., Erra, P., Gonzalez-Elipe, A.R., XPS analysis of downstream treated wool: Influence of the nature of the gas on the surface modification of wool, Applied Surface Science 252, (2005) 1417-1429

Molina, R., Jovancic, P., Comelles, F., Bertran, E., Erra, P., Shrink-resistance and wetting properties of keratin fibres treated by glow discharge, J. Adhesion Sci Technol. Vol. 16 No. 11, (2002) 1469-1485

Prowse, M.S., Puthoff, J.B., Wilkinson, M., Autumn, K., Effects of Humidity on the Mechanical Properties of Gecko Setae. Acta Biomaterialia 7 (2011) 733-738

Puthoff, J.B., Prowse, M.S., Wilkinson, M., Autumn, K., Changes in Materials Properties Explain the Effects of Humidity on Gecko Adhesion, J. Exp. Biol. 213 (2010). 3699-3704

Rizzo, N.W., Garner, K.H., Walls, D.J., Keiper-Hrynko, N.M., Ganzke, T.S., Hallahan, D.L., Characterization of the Structure and Composition of Gecko Adhesive Setae. J.R. Soc. Interface. 3 (2005) 441-451

Stohr, J., NEXAFS Spectroscopy. Srpinger-Verlag. New York 1996

Tu, M.C., Lillywhite, H.B., Menon, J.G., Menon, G.K., Postnatal ecdysis establishes the permeability barrier in snake skin: new insights into barrier lipid structures. JEB. 205 (2002) 3019-3030

Weidner, T., Sammuel, T., McCrea, K., Gamble, L.J., Stayton, P.S., Castner, D.G., Assembly and structure of a-helical peptide films on hydrophobic fluorocarbon surfaces. Biointerphases. 5 (2010) 9

Zhang, W., Carravette, V., Piekan, O., Feyer, V., Richter, R., Coreno, M., Prince, K.C., Electronic structure of aromatic amino acids studied by soft x-ray spectroscopy. J. of Chem. Phys. 131 (2009) 035103-1-11

Zubavichus, Y., Shaporenko, A., Grunze, M., Zharnikov, M., Innershell Absorption Spectroscopy of Amino Acids at All Relevant Absorption Edges. Phys. Chem. A letters, 109 (2005) 6998-7000

Chapter 6 Conclusions

6.1 Conclusion

Geckos have remarkable climbing ability due to their hierarchical toe structure. This climbing ability can be enhanced or decreased by mechanical properties modification of the setae. In the presences of water the β-keratin softens decreasing the elastic modulus in tandem with an increase in non-elastic loss. The effect of which enhances the tackiness of the setal arrays. This work has shown a significant influence of relative humidity on the mechanical properties of setal and lamellar keratin, including elasticity, tensile strength, fracture, and dynamic response. The loss tangent increased significantly, by a factor 3x over the humidity range 30 – 80% RH, suggesting that viscoelastic losses increase due to water absorption. In single isolated setae and smooth epidermal layer under dynamic sinusoidal loading, the complex elastic modulus at 80%RH is ~1/3 the value at dry conditions with similar results on elastic modulus from linear loading. Deformation properties were similar in lamellar samples, with a few exceptions. The changes in mechanical properties of setal keratin were consistent with previously reported studies of the mechanical properties of β-keratin.

Furthermore, we have shown that adhesion in Tokay geckos are not enhanced by capillary formation, but fits well with the van der Waals adhesion model over a range of drag velocities, substrates and relative humidity levels. The data was not consistent with a capillary model of adhesion. Rather, the data indicated softening of the setae and increase in viscoelastic loss enhanced adhesion at elevated humidity. Physically the increase in adhesion is a result of more compliant setae adhering to the surface in larger numbers and being less apt to detach due to visco-elastic loses internal the setae.

Initial surface chemical analysis indicates the eye spectacle is the most ordered structure. However, this is likely a result of surface roughness influence rather than a dramatic difference in structure. The setae showed the lowest presence of protein of the samples tested (scale, eye spectacle, lamella, and setae). Whether this result is from the presence of a thin membrane covering the setae shaft or a manifestation of a structural difference in the spatula is unknown at this time and requires further study. The other constituent of the setae is also unknown. Initial data suggests the possibility of lipids but carbohydrates is feasible and not ruled out by the data. There are also clear differences in the surface chemistry of the scale, eye spectacle, lamella and setae.

6.2 Future Work

There is a wide variety of toe structures found in geckos - these structures have not been investigated and could be intriguing to study. Consequently, there remain many unanswered questions of the nature of gecko adhesion in species other than Tokay, such as, is adhesion with respect to relative humidity species dependant? If humidity dependence on adhesion varies with species, are these differences materials related or could they be explained by some other means such as setal geometry consideration.

The geometry of the setae stalks with the relatively soft lipid matrix between the stronger keratin fibril is important to understand the implications of the structure; potentially the structure could offer better contact compliance of the spatulas to the surface. But analysis of the structure is needed. While it is speculated, the number of spatula contacts increases at higher RH, confirmation either through modeling or direct observation is desirable.

It will be interesting to determine more detailed chemical nature of the setal surface. While initial NEXAFS and XPS was conducted for this thesis and prior work with water contact angle, TEM, and SFG - there are many more questions to be answered in future studies regarding the surface chemistry. Further surface chemistry study is needed to resolve the exact nature of the setal surface and the effect it has on adhesion and contact properties. Ideally additional surface studies will include samples in hydrated and dehydrated states.

Appendix A.1 - XPS survey scan of the setal array

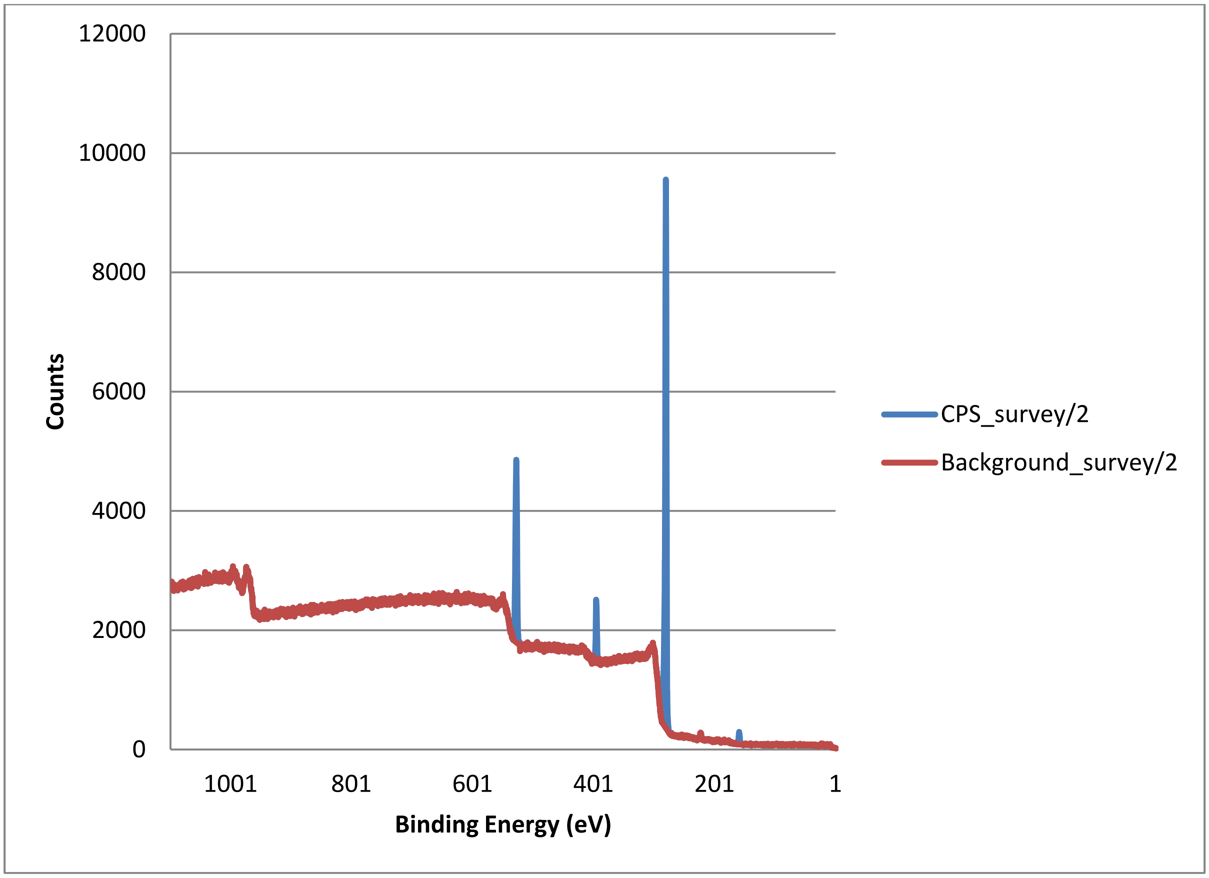

Appendix A.2 - XPS Sulfur 2p scan of the setal array

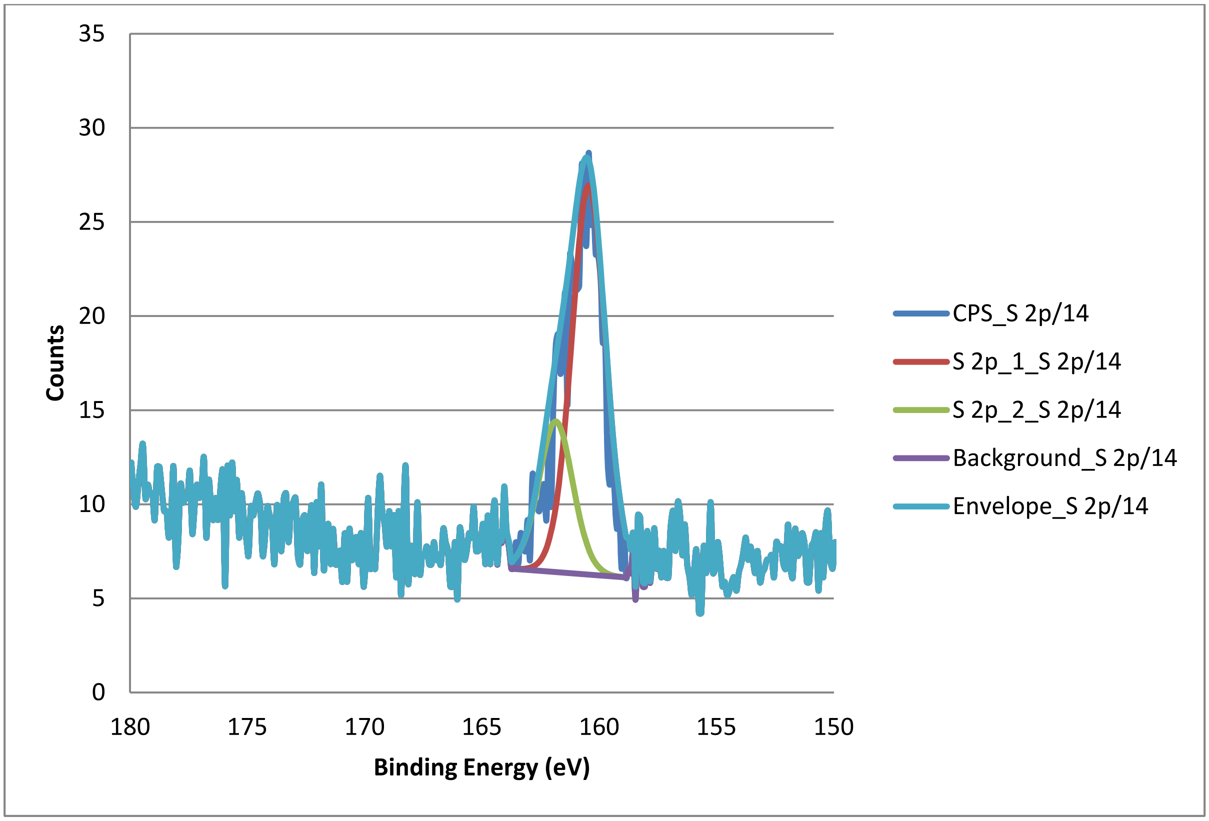

Appendix A.3 - XPS Carbon 1s scan of the setal array

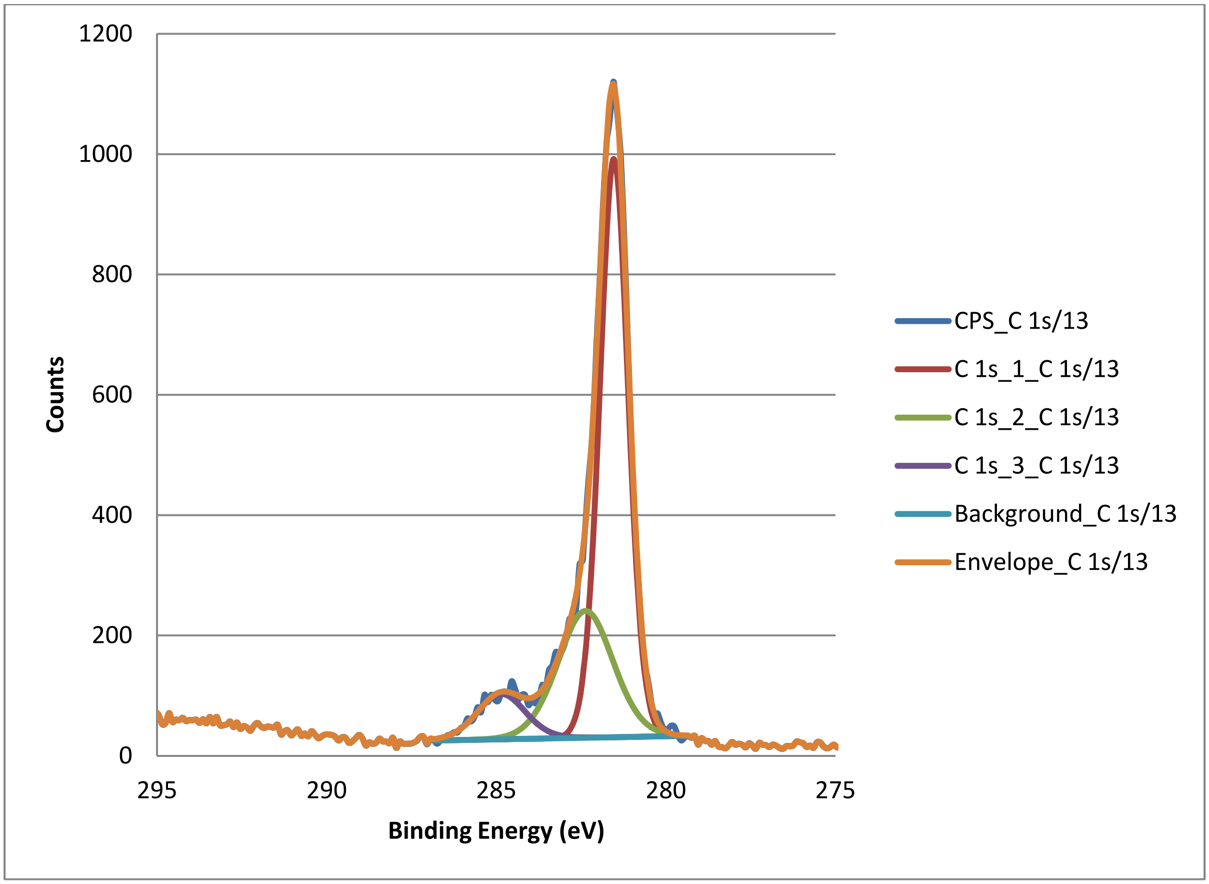

Appendix A.4 - XPS Nitrogen 1s scan of the setal array

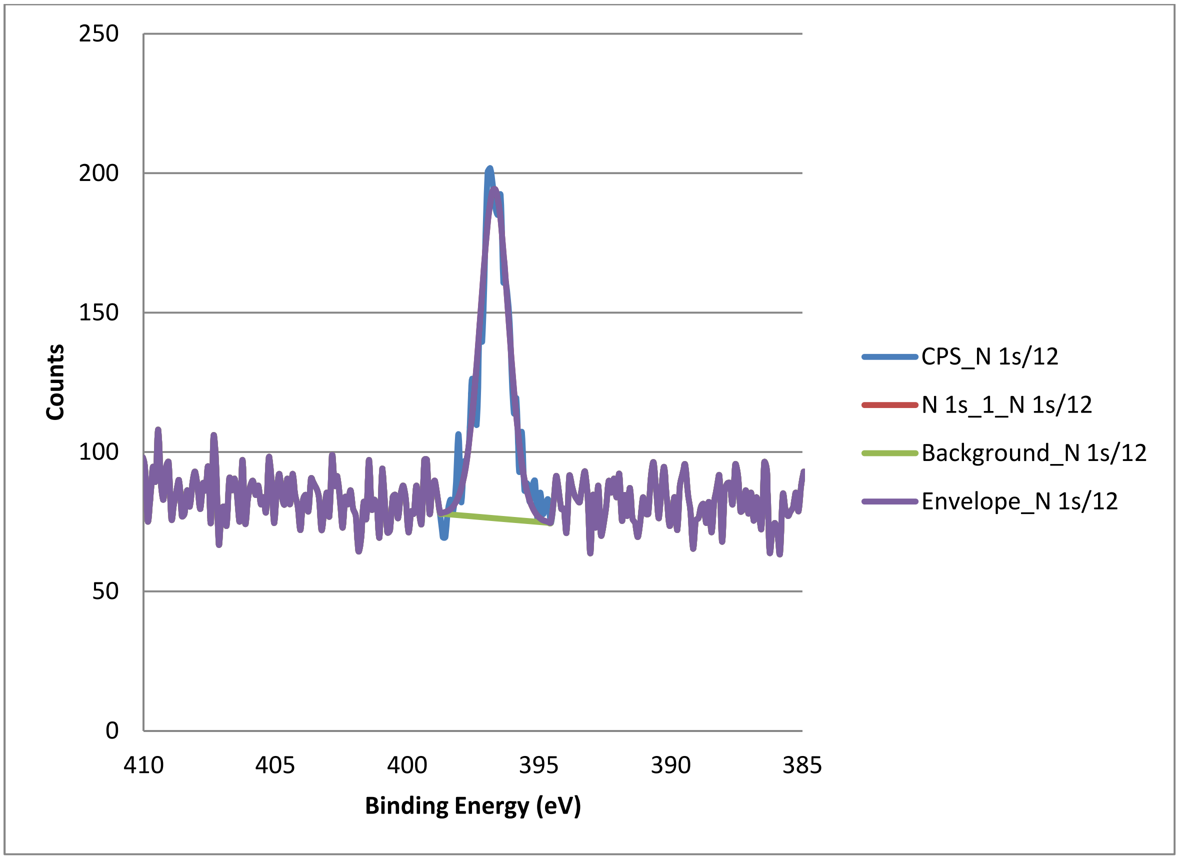

Appendix A.5 - XPS Oxygen 1s scan of the setal array

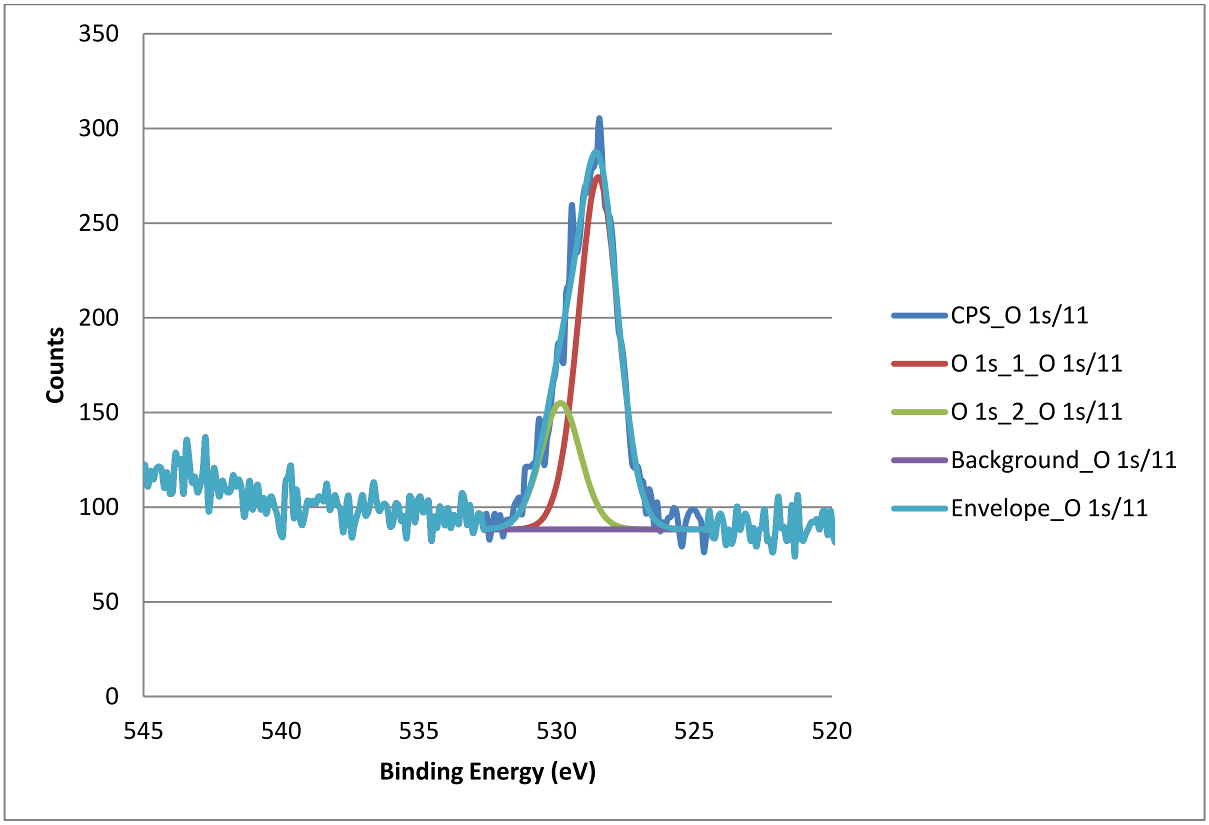

VITA

Michael Prowse was born in Tacoma Washington. At the University of Washington he earned a Bachelor of Science degree in Ceramic Engineering and a Master of Science in Materials Science and Engineering. In 2012 he earned a Doctor of Philosophy at the University of Washington in Materials Science and Engineering. He currently resides outside of Portland Oregon.